optica

Volume 1 • Issue 2 • August 2014

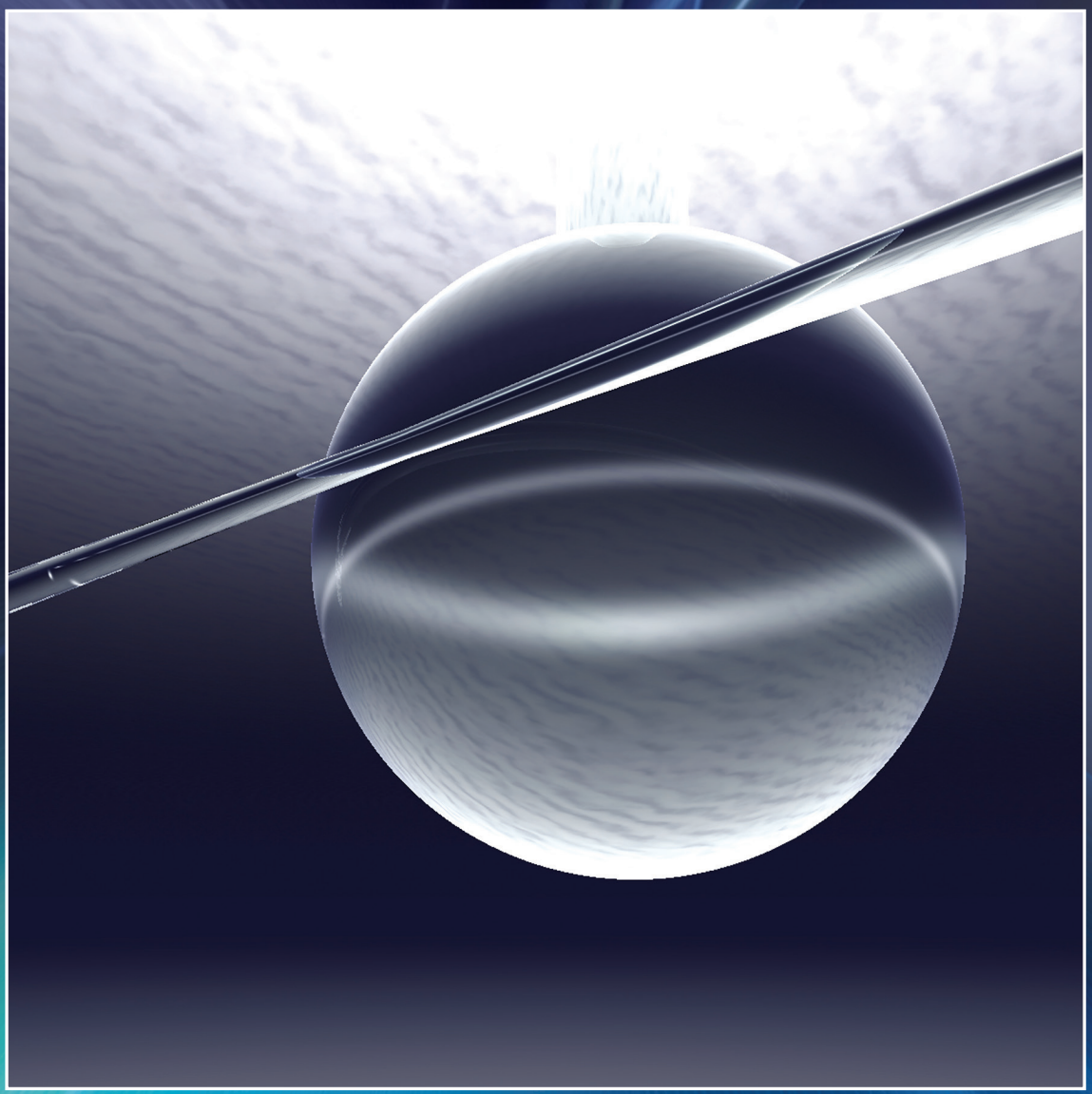

OSA®
The Optical Society

ISSN: 2334-2536

optica.osa.org

Research Article Vol. 1, No. 2 / August 2014 / Optica 64

Time-stretched sampling of a fast microwave waveform based on the repetitive use of a linearly chirped fiber Bragg grating in a dispersive loop

JIEJUN ZHANG AND JIANPING YAO*

Microwave Photonics Research Laboratory, School of Electrical Engineering and Computer Science, University of Ottawa, Ontario K1N 6N5, Canada

**Corresponding author: jpyao@eecs.uottawa.ca*

Received 21 March 2014; revised 28 May 2014; accepted 29 May 2014 (Doc. ID 208550); published 1 August 2014

Conventional sampling techniques may not be able to meet the ever-increasing demand for increased bandwidth from modern communications and radar signals. Optical time-stretched sampling has been considered an effective solution for wideband microwave signal processing. Here, we demonstrate a significantly increased stretching factor in the photonic time-stretched sampling of a fast microwave waveform. The microwave waveform to be sampled is intensity modulated on a chirped optical pulse generated jointly by a mode-locked laser and a length of dispersion compensating fiber. The pulse is then injected into an optical dispersive loop that includes an erbium-doped fiber amplifier and is stretched by a linearly chirped fiber Bragg grating multiple times in the loop. A record stretching factor of 36 is achieved based on an equivalent group delay dispersion coefficient of 12,000 ps/nm. This result could help address the new challenges imposed on signal processors to operate at a very high sampling rate.

OCIS codes: (060.7140) Ultrafast processes in fibers; (070.1170) Analog optical signal processing; (060.5625) Radio frequency photonics; (130.2035) Dispersion compensation devices.

http://dx.doi.org/10.1364/OPTICA.1.000064

1. INTRODUCTION

The ever-increasing bandwidth of modern communications and radar signals has imposed new challenges on signal processors to operate at a very high sampling rate. The use of the conventional sampling techniques may not be able to meet the demand. To realize broadband sampling, a solution is to use photonic-assisted sub-Nyquist sampling. Numerous approaches have been proposed, such as optical downsampling [1,2], optical undersampling [3], optical pseudorandom sampling [4], compressive sampling [5], and optical time-stretched sampling [6–14]. Among these techniques, optical time-stretched sampling has been considered an effective solution for wideband microwave signal processing.

In an optical time-stretched sampling system, a microwave waveform is modulated on a predispersed optical pulse, which, after the modulation, travels through another dispersive element for time stretching. The second dispersive element should have a much greater group delay dispersion (GDD) coefficient than the first element. A time-stretched microwave waveform will be generated when the pulse is sent to a photodetector (PD) and a slow version of the original waveform is obtained [15]. This technique was first proposed by Coppinger *et al.* in [7], demonstrating a sampling rate that is 1/3.25 of the Nyquist frequency. Since then, new efforts have been dedicated to further reducing the sampling rate by increasing the stretching factor. In [8], dispersion-based time-stretched sampling with a stretching factor of 5 combined with compressive sensing was demonstrated to achieve a sampling rate as low as only 1/40 of the Nyquist frequency. The sampling rate is then further reduced to 1/80 of the Nyquist frequency by

using a time-stretched sampling module with a time stretching factor of 20 [9]. In [10], time-stretched sampling using a coherent receiver to improve the detection sensitivity by cancelling the dispersion-induced impairments and optical nonlinearity was demonstrated. A stretching factor of 24 was achieved by using two dispersive elements with two GDD coefficients of 45 and 1045 ps/nm for predispersion and time stretching, respectively. In [11], time-stretched sampling of a continuous-time signal was demonstrated based on virtual time gating, where a stretching factor of 1.5 was achieved. To overcome the "big data" problem associated with time-stretched sampling, Asghari and Jalali demonstrated a sampling solution based on nonlinear time stretching [12]. An equivalent stretching factor of 200 was achieved. The system has been further enhanced to achieve a real-time bandwidth suppression factor of 500 [13]. In the system, a programmable optical filter was used to modulate the microwave waveform to the optical pulse, which may make the system complicated and costly. In [14], an unprecedented time-stretching factor of 250 was realized by using a predispersion element with a GDD coefficient of 41 ps/nm and a double-pass dispersive element with a GDD coefficient of −10, 246 ps/nm. To achieve such a large dispersion, an extremely long dispersion compensating fiber (DCF) is used. To compensate for the loss in the long DCF, four stimulated Raman amplifiers pumped by four high-power laser diodes were employed. Although the system could realize an effective sampling rate of 10 T samples/s, the use of a long DCF and multiple Raman amplifiers makes the system rather bulky and complicated. For a time-stretching element with a fixed GDD coefficient, to achieve a large stretching factor, the predispersion element could be selected to have a relatively small GDD coefficient. The consequence of using a predispersion element with small dispersion is that the input optical pulse cannot be sufficiently prestretched to have a large time duration, to allow a microwave waveform with a long duration to be modulated on the prestretched input pulse. Therefore, the fundamental solution for having a large stretching factor for a long-duration microwave waveform is to use a time-stretching element with a large GDD coefficient.

In fiber optics, a dispersive element can be a single-mode fiber (SMF), a DCF, or a linearly chirped fiber Bragg grating (LCFBG). Since an SMF has a relatively small dispersion coefficient, it is rarely used in a time-stretched sampling system, especially as the time-stretching dispersive element. A DCF, on the other hand, can have a dispersion coefficient that is several times greater than that of an SMF. However, to achieve large time stretching, a DCF with a length of several tens [10] or even hundreds [14] of kilometers is required. Thus, the system is still bulky and lossy. An LCFBG has been proved to be a highly effective dispersive element with low insertion loss and small nonlinear effects [16,17]. The GDD of an LCFBG is proportional to its grating length and inversely proportional to its bandwidth. For time-stretching applications, the bandwidth of an LCFBG is usually controlled to be equal to the bandwidth of the optical pulse. Hence, to have a large GDD coefficient, an LCFBG with a long length is needed. For example, a 10 cm long LCFBG with 1 nm bandwidth has a GDD coefficient of 1000 ps/nm. To further increase the GDD coefficient, the length of the LCFBG should be further increased. Although an LCFBG with a length greater than 1 m is commercially available, the size is large and the fabrication is complicated and costly.

The use of a microwave waveguide with a large GDD coefficient has been explored in the past few years for spectrum analysis [18,19]. Recently, it was demonstrated [20] that by forming a dispersive loop that incorporates a microwave dispersive element and a microwave amplifier, an equivalent microwave dispersive element with a GDD coefficient that is several times greater than that of the original dispersive element can be achieved by recirculating the microwave waveform in the loop. Compared with a simple cascade of multiple dispersive elements for achieving an equivalent dispersive element with a large GDD coefficient, the recirculating dispersive loop has advantages such as a smaller device footprint, lower insertion loss, and a better signal-to-noise ratio (SNR) [20]. The major limitations of an electrical dispersive loop are the small bandwidth, usually below 1 GHz, and high loss. In addition, the maximum time delay is limited, although the constant time delay provided by a coaxial cable is already much larger compared to that of a waveguide. To implement a dispersive loop with a large GDD coefficient over a large bandwidth, a solution is to use photonic components. In addition to a broad bandwidth, an optical dispersive loop can generate a much longer time delay, since a long loop is possible due to the extremely low loss of an optical fiber. A time-stretched sampling system using an optical dispersive loop can significantly increase the stretching factor over a broad bandwidth.

In this paper, we propose a novel technique for achieving time-stretched microwave sampling with a significantly increased stretching factor. In the proposed system, a microwave waveform is modulated on a predispersed optical pulse, which is sent to a recirculating dispersive loop consisting of an LCFBG and an erbium-doped fiber amplifier (EDFA). The LCFBG is used to achieve repetitive pulse stretching, and the EDFA is used to compensate for the loss in the loop. By controlling the gain of the EDFA to compensate for the loop loss, the optical waveform can recirculate in the loop, and repetitive use of the LCFBG for accumulated pulse stretching is realized. The proposed technique is experimentally demonstrated. An LCFBG with a GDD coefficient of 1500 ps/nm is fabricated and incorporated in the recirculating dispersive loop. An equivalent GDD coefficient of 12, 000 ps/nm is achieved, which, to the best of our knowledge, is the largest dispersion ever reported for time-stretched sampling. The corresponding stretching factor is 36. The use of the system to sample a microwave waveform is demonstrated. For a sampling system with a bandwidth of 32 GHz, the use of the proposed recirculating dispersive loop can extend the bandwidth by 36 times, or 1.15 THz (or a time resolution of 347 fs), with a frequency resolution of 4.93 GHz.

2. PRINCIPLE

The schematic of the proposed time-stretched sampling system is shown in Fig. 1. An optical pulse from a mode-locked laser (MLL) is sent to a DCF serving as a predispersion element.

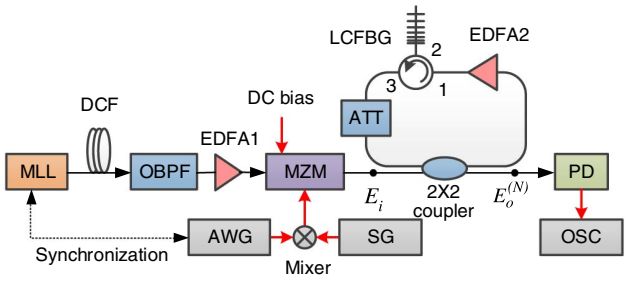

Fig. 1. Schematic of the time-stretched sampling system. MLL, mode-locked laser; OBPF, optical bandpass filter; DCF, dispersion compensating fiber; EDFA, erbium-doped fiber amplifier; MZM, Mach–Zehnder modulator; ATT, attenuator; LCFBG, linearly chirped fiber Bragg grating; PD, photodetector; AWG, arbitrary waveform generator; SG, signal generator; OSC, oscilloscope.

The predispersed optical pulse is then sent to a Mach–Zehnder modulator (MZM) through an optical bandpass filter (OBPF) and an EDFA (EDFA1). A microwave waveform is modulated on the predispersed optical pulse at the MZM. The modulated signal is then sent to the recirculating dispersion loop, in which an LCFBG and a second EDFA (EDFA2) are incorporated. Note that the bandwidth of the OBPF is identical to the bandwidth of the LCFBG, so the predispersed optical pulse at the output of the OBPF has a spectral width that is identical to that of the LCFBG. The microwave waveform to the MZM is generated by mixing an electrical gate signal from an arbitrary waveform generator (AWG) with a sinusoidal microwave signal from a microwave generator (SG). The modulated waveform is launched into the recirculating dispersive loop through a 2 × 2 3 dB coupler. In the loop, the LCFBG is used as a dispersive element and EDFA2 is used to compensate for the round-trip loss. An attenuator (ATT) is also included in the loop to provide fine control of the loop gain in order to maintain full compensation of the loss while avoiding optical lasing in the loop. The optical pulse is recirculating in the dispersive loop. The time-stretched optical pulse at the output of the loop is sent to a PD. The stretched microwave waveform is sampled by a real-time oscilloscope.

It is known that an LCFBG has a quadratic phase response within its passband. Its transfer function can be written as [21]

$$H_{\mathrm{LCFBG}}(\omega) = \exp\left(-j\frac{\beta_C}{2}\omega^2\right), \tag{1}$$

where ω is the optical angular frequency and β_C is the GDD coefficient of the LCFBG (in ps^2). Assuming that the optical spectrum at the input of the dispersive loop is $E_i(\omega)$, the output spectrum after recirculating for N round trips in the loop can be written as

$$E_o^{(N)} = \left(\frac{\sqrt{2}}{2}\right)^{N+1} g^N E_i(\omega) H^N(\omega), \tag{2}$$

where g is the net gain of the loop, which can be changed by tuning the gain of EDFA2 or the loss of the attenuator. If we make g close to but slightly less than $\sqrt{2}$, we then have $(\sqrt{2}g/2)^N \approx 1$. The transfer function of the loop can be expressed as

$$H_{\mathrm{loop}}(\omega) = \frac{E_o^{(N)}}{E_i} = \frac{\sqrt{2}}{2}\exp\left(-j\frac{N\beta_C}{2}\omega^2\right). \tag{3}$$

By comparing Eqs. (1) and (3), we can see that the recirculating dispersive loop acts as a dispersive element that has an equivalent GDD coefficient of $N\beta_C$. It should be noted that in practice, $\sqrt{2}g/2$ should always be smaller than unity to prevent the loop from lasing. As a result, the amplitude of $H_{\mathrm{loop}}(\omega)$ should decay with the increase of N. The maximum number of N is determined by the minimum SNR required to detect the time-stretched signal. If the 2 × 2 coupler is replaced by an optical switch, then the number of recirculations can be controlled by the optical switch. In this case, the equivalent GDD coefficient of the recirculating dispersive loop can be tunable by letting the waveform recirculate in the loop for a certain number of round trips.

The stretching factor of the time-stretched sampling system is given by

$$M = 1 + N\beta_C/\beta_D, \tag{4}$$

where β_D is the GDD coefficient of the predispersion element. Since the second term in Eq. (4) is much greater than 1, it can be seen that the stretching factor increases proportionally to the number of the round trips N. Again, if an optical switch is employed in the system, the stretching factor can then be adjusted to improve the performance of the sampling system according to the frequency band of the input waveform. For example, N should be large for a fast microwave waveform so that all the details of the microwave waveform can be revealed, while for a relatively slow microwave waveform, N should be small to avoid oversampling and data redundancy [12,13].

3. EXPERIMENT

An experiment based on the setup shown in Fig. 1 is performed. In the experiment, an MLL (IMRA femtolite 780) with a repetition rate of 48 MHz and a central wavelength of 1558 nm is employed to produce an optical pulse train. An individual pulse in the pulse train is nearly transform limited with a 3 dB spectral bandwidth of 8 nm. The predispersion element is a DCF with a dispersion coefficient of $\beta_C = 432$ ps^2 (or −339 ps/nm). The LCFBG used in the dispersive loop has a dispersion coefficient of $\beta_C = 1912$ ps^2 (or −1500 ps/nm) within a reflection passband of 0.6 nm centered at 1558 nm. The OBPF (Finisar WaveShaper 4000S) is configured to have a near-rectangular passband with a bandwidth identical to that of the LCFBG. It can be calculated that after the predispersion by the DCF and the filtering by the OBPF, the MLL pulse is stretched to have a time duration of $\Delta\tau = 203$ ps. The optical pulse train at the output of the OBPF is amplified by EDFA1 and sent to the MZM. The MZM has a bandwidth of 20 GHz and is biased at its minimum transmission point. A microwave waveform generated by mixing an 18 GHz microwave signal from the

SG with a rectangular pulse train with a repetition rate of 286 kHz serving as a gate signal from the AWG is applied to the MZM. The repetition rate of the rectangular pulse train is smaller than that of the MLL (48 MHz) to reduce the duty cycle of the modulated optical pulse train, thus allowing pulse stretching with a large stretching factor without creating overlap between adjacent pulses. Note that in the experiment, the AWG and the MLL are synchronized. The modulated optical waveform at the output of the MZM is sent to the recirculating dispersive loop via the 2 × 2 coupler. The length of the recirculating dispersive loop is estimated to be 61 m (corresponding to a time delay of 305 ns). The time-stretched optical pulse from the recirculating dispersive loop is sent to the PD (25 GHz, New Focus). The electrical waveform at the output of the PD is sampled by a real-time oscilloscope (Agilent DSO-X 93204A).

The modulation process is depicted in Fig. 2. As can be seen from Fig. 2(a), the gate signal with a repetition rate of 286 kHz and a gate duration of 20.8 ns is mixed with the 18 GHz microwave generated by the SG and sent to the MZM. Since the MZM is biased at its minimum transmission point, the predispersed pulse train corresponding to the low voltage level of the modulation waveform will not be able to pass through the MZM, and the pre-dispersed pulse train corresponding to the high voltage level of the modulation waveform is modulated by a microwave waveform with twice the frequency of the microwave signal generated by the SG (i.e., 36 GHz), as shown in Fig. 2(b). Therefore, the number of microwave cycles in each MLL pulse is 7. In addition, there will be only one MLL pulse that is modulated by the microwave waveform in every period of the gate. The resulting pulse train with a reduced repetition rate is illustrated in Fig. 2(c). It should be noted that for practical applications one can use an MLL with a lower repetition rate so that the gate signal is not needed. Then the MZM can be biased at the quadratic point and the waveform carried by the MLL pulse will be the same as the modulation signal.

The modulated pulses are then injected into the recirculating dispersive loop. In every round trip, part of the optical

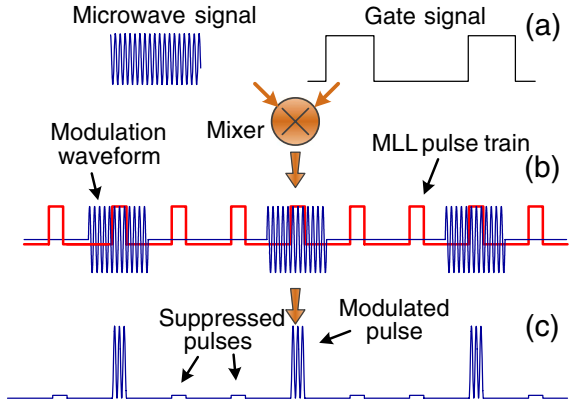

Fig. 2. Modulation process. (a) An 18 GHz microwave signal generated by the SG (solid blue line) and a gate signal generated by the AWG (black), (b) the waveform applied to the MZM (blue) and the MLL pulse train after predispersion and filtering (red), (c) the resulting optical pulse train carrying the microwave waveform with a reduced repetition rate.

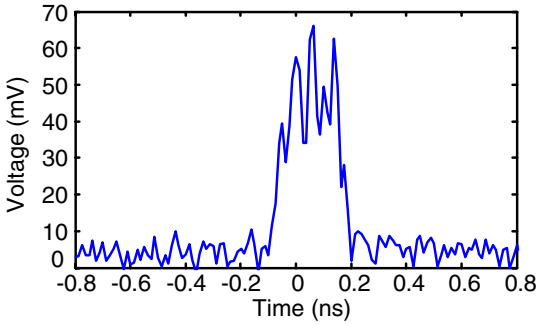

Fig. 3. Waveform of the modulated MLL pulse measured at the output of the MZM.

pulse is coupled out of the loop by the 2 × 2 coupler and detected by the PD.

Figure 3 shows the measured MLL pulse at the output of the MZM. The FWHM of the pulse is measured to be around 230 ps. Compared to the theoretical pulse width of $\Delta\tau = 203$ ps, the 27 ps difference could be caused by the relatively large sampling interval of 12.5 ps of the oscilloscope. The microwave waveform modulated on the predispersed pulse cannot be correctly sampled, since the doubled microwave frequency of 36 GHz exceeds the highest frequency of the oscilloscope.

The waveform at the output of the dispersive loop is then measured by the real-time oscilloscope, as shown in Fig. 4. As can be seen when a modulated optical waveform is launched into the recirculating dispersive loop, a pulse burst with a decaying amplitude is generated. The quick decay in amplitude is due to the loss in the loop. To avoid lasing in the loop, the gain of EDFA2 is controlled to be smaller than the loss. The time duration between two adjacent pulses is 308 ns, which corresponds to the time delay of the recirculating dispersive loop. The time duration between two large pulses is 3.5 μs, corresponding to the repetition time of the optical pulse train at the output of the MZM.

Theoretically, the decaying can be reduced by increasing the loop gain. However, due to the uneven magnitude response of the LCFBG and the uneven gain spectrum of EDFA2, the recirculating dispersive loop may start lasing at a certain wavelength when the loop gain is increased, while at the other wavelengths, the loop gain is still smaller than 1. The relatively high noise floor is mainly caused by the amplified spontaneous

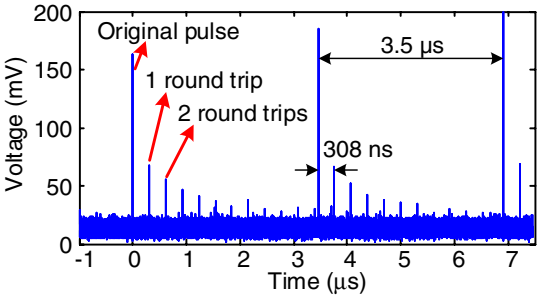

Fig. 4. Measured optical waveform at the output of the recirculating dispersive loop.

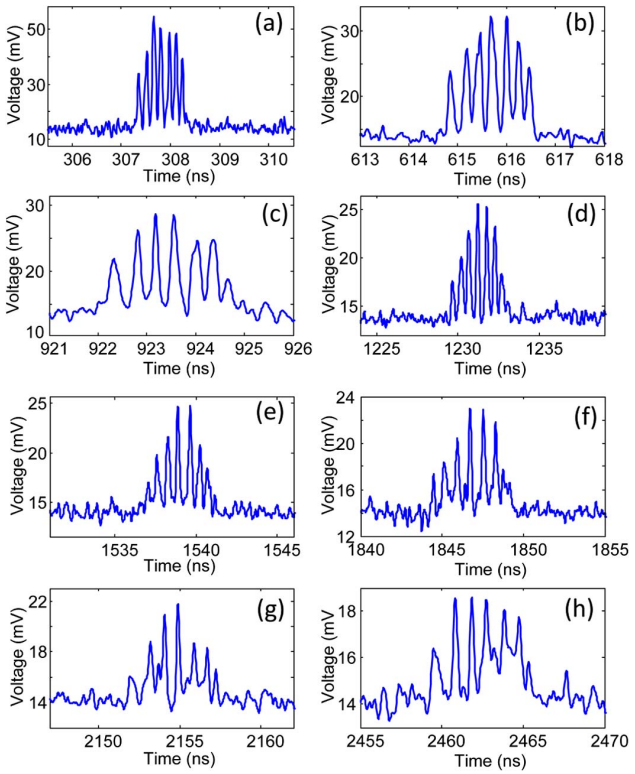

Fig. 5. Output waveforms after different numbers of round trips. (a) One round trip, (b) two round trips, (c) three round trips, (d) four round trips, (e) five round trips, (f) six round trips, (g) seven round trips, and (h) eight round trips. Note that the time scale is 1 ns/division in (a)–(c) and 5 ns/division in (d)–(h).

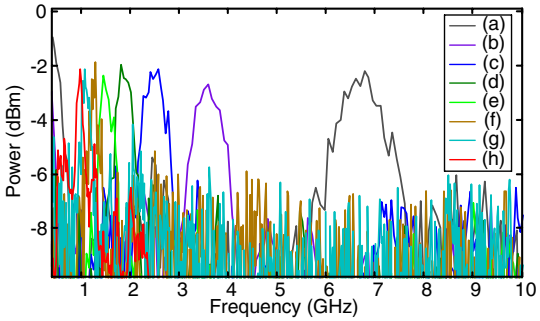

Fig. 6. Electrical spectra of the measured time-stretched waveforms for different numbers of round trips. (a)–(h) correspond to the waveforms given in Figs. 5(a)–5(h).

emission of EDFA2 and the occasional lasing of the loop, as the loop gain is very close to 1 at some wavelengths. To increase the SNR of the system, an LCFBG with a specially designed amplitude response or an EDFA gain-flattening filter should be included in the loop to avoid lasing. One may also use an optical switch to replace the optical coupler so that the loop loss can be reduced, and a lower gain for EDFA2 is required.

The detailed waveforms after the pulse is stretched in the recirculating dispersive loop for one to eight round trips are shown in Figs. 5(a)–5(h). After one round trip, the pulse duration is stretched to around 1 ns and all seven microwave cycles with a temporal separation between two adjacent cycles of around 140 ps can be identified, as shown in Fig. 5(a). The optical pulse is stretched with a stretching factor of around 5.

Then, the optical pulse keeps on recirculating in the loop, with the stretched pulses shown in Figs. 5(b)–5(h). Since the round-trip loss cannot be completely compensated by the gain of EDFA2, and the amplified spontaneous emission of EDFA2 introduces a significant amount of noise, the SNR drops after each round trip. By fine control of the loop gain using the tunable attenuator, we are able to make the pulse circulate for eight round trips before it is fully imbedded in the noise. For the pulse after the eighth round trip, the equivalent GDD is 8×1500 ps/nm $= 12,000$ ps/nm. The measured waveform after the eighth round trip shows that the pulse duration is around 7 ns and the average temporal separation between each microwave cycle is 1 ns. This indicates that a stretching factor of 36 is obtained, which is close to the theoretically calculated stretching factor of 36.4 based on Eq. (4). Assuming that the bandwidth of the system is limited by the oscilloscope used in our experiment, which is 32 GHz, the bandwidth of the sampling system can be as large as $36 \times 32 = 1.15$ THz, corresponding to a time resolution of 347 fs. The frequency resolution, on the other hand, is limited by the time duration of the optical pulse used to carry the microwave waveform, which is $(203 \text{ ps})^{-1} = 4.93$ GHz.

Figure 6 shows the electrical spectra of the measured waveforms for different numbers of round trips given in Fig. 5. The spectra show that the SNR decreases as the number of round trips increases, which agrees with our discussion. It can also be seen that for a single frequency input, there is only one output frequency component, which means that the signal distortion effect usually encountered by a time-stretched system has a weaker effect compared to the SNR deterioration and is negligible.

4. DISCUSSION AND CONCLUSION

A novel time-stretched sampling system with a large stretching factor has been demonstrated by the repetitive use of an LCFBG in a recirculating dispersive loop. An equivalent GDD as large as 12, 000 ps/nm with a large stretching factor of 36 was achieved. This is the second largest dispersion-based stretching factor for a time-stretched sampling system ever reported. Although the stretching factor of 250 reported in [14] is much greater than the stretching factor of 36 in this work, we have demonstrated a dispersive element with a greater dispersion than that in [13]. If we used a predispersion element that has a similar dispersion coefficient as the one in [14], we would be able to achieve a much greater stretching factor than 250. Note that for pulse stretching with a very large stretching factor, the input pulse applied to the MZM should be very short; thus the system can only sample a microwave waveform with a narrow width.

It should also be noted that the stretching factor can be further increased by using a low-noise optical amplifier. In addition, by flattening the magnitude response of the LCFBG and the gain of EDFA2, the net gain in the loop can be controlled to be very close to 1, but with no lasing; thus an input

pulse can recirculate in the loop more times, which would lead to a much greater stretching factor. In [22], a microwave photonic filter with an ultra-even magnitude response was used to achieve pulse recirculation in an active cavity for 270 round trips. If this can be realized for a wideband LCFBG, the equivalent GDD can be as large as 4.05×10^5 ps/nm, which corresponds to a stretching factor of 1195.

FUNDING INFORMATION

China Scholarship Council (201206160086); Natural Sciences and Engineering Research Council of Canada (NSERC).

REFERENCES

1. P. W. Juodawlkis, J. J. Hargreaves, R. D. Younger, G. W. Titi, and J. C. Twichell, "Optical down-sampling of wide-band microwave signals," J. Lightwave Technol. **21**, 3116–3124 (2003).
2. B. C. Pile and G. W. Taylor, "Performance of subsampled analog optical links," J. Lightwave Technol. **30**, 1299–1305 (2012).
3. A. Feldster, Y. P. Shapira, M. Horowitz, A. Rosenthal, S. Zach, and L. Singer, "Optical under-sampling and reconstruction of several bandwidth-limited signals," J. Lightwave Technol. **27**, 1027–1033 (2009).
4. M. B. Airola, S. R. O'Connor, M. L. Dennis, and T. R. Clark, "Experimental demonstration of a photonic analog-to-digital converter architecture with pseudorandom sampling," IEEE Photon. Technol. Lett. **20**, 2171–2173 (2008).
5. G. C. Valley, G. A. Sefler, and T. J. Shaw, "Compressive sensing of sparse radio frequency signals using optical mixing," Opt. Lett. **37**, 4675–4677 (2012).
6. F. Coppinger, A. Bhushan, and B. Jalali, "Photonic time stretch and its application to analog-to-digital conversion," IEEE Trans. Microwave Theory Tech. **47**, 1309–1314 (1999).
7. F. Coppinger, A. Bhushan, and B. Jalali, "Time magnification of electrical signals using chirped optical pulses," Electron. Lett. **34**, 399–400 (1998).
8. H. Chi, Y. Chen, Y. Mei, X. Jin, S. Zheng, and X. Zhang, "Microwave spectrum sensing based on photonic time stretch and compressive sampling," Opt. Lett. **38**, 136–138 (2013).
9. Y. Chen, H. Chi, T. Jin, S. Zheng, X. Jin, and X. Zhang, "Sub-Nyquist sampled analog-to-digital conversion based on photonic time stretch and compressive sensing with optical random mixing," J. Lightwave Technol. **31**, 3395–3401 (2013).
10. B. W. Buckley, A. M. Madni, and B. Jalali, "Coherent time-stretch transformation for real-time capture of wideband signals," Opt. Express **21**, 21618–21627 (2013).
11. Y. Han and B. Jalali, "Continuous-time time-stretched analog-to-digital converter array implemented using virtual time gating," IEEE Trans. Circuits Syst. I, Reg. Papers **52**, 1502–1507 (2005).
12. M. H. Asghari and B. Jalali, "Anamorphic transformation and its application to time–bandwidth compression," Appl. Opt. **52**, 6735–6743 (2013).
13. M. H. Asghari and B. Jalali, "Experimental demonstration of optical real-time data compression," Appl. Phys. Lett. **104**, 111101 (2014).
14. J. Chou, O. Boyraz, D. Solli, and B. Jalali, "Femtosecond real-time single-shot digitizer," Appl. Phys. Lett. **91**, 161105 (2007).
15. J. Yao, "Photonic generation of microwave arbitrary waveforms," Opt. Commun. **284**, 3723–3736 (2011).
16. X. Dong, P. Shum, N. Ngo, C. Chan, J. Ng, and C. Zhao, "A largely tunable CFBG-based dispersion compensator with fixed center wavelength," Opt. Express **11**, 2970–2974 (2003).
17. T. Erdogan, "Fiber grating spectra," J. Lightwave Technol. **15**, 1277–1294 (1997).
18. J. D. Schwartz, J. Azaña, and D. V. Plant, "Experimental demonstration of real-time spectrum analysis using dispersive microstrip," IEEE Microwave Wireless Compon. Lett. **16**, 215–217 (2006).
19. M. A. Laso, T. Lopetegi, M. J. Erro, D. Benito, M. J. Garde, M. A. Muriel, M. Sorolla, and M. Guglielmi, "Real-time spectrum analysis in microstrip technology," IEEE Trans. Microwave Theory Tech. **51**, 705–717 (2003).
20. B. Nikfal, S. Gupta, and C. Caloz, "Increased group-delay slope loop system for enhanced-resolution analog signal processing," IEEE Trans. Microwave Theory Tech. **59**, 1622–1628 (2011).
21. G. P. Agrawal, *Nonlinear Fiber Optics*, 3rd ed. (Academic, 2001).
22. D. B. Hunter and R. A. Minasian, "Photonic signal processing of microwave signals using an active-fiber Bragg-grating-pair structure," IEEE Trans. Microwave Theory Tech. **45**, 1463–1466 (1997).

optica

Optical sectioning using a digital Fresnel incoherent-holography-based confocal imaging system

ROY KELNER,* BARAK KATZ, AND JOSEPH ROSEN

Department of Electrical and Computer Engineering, Ben-Gurion University of the Negev, P.O. Box 653, Beer-Sheva 8410501, Israel
**Corresponding author: kelnerr@post.bgu.ac.il*

Received 26 March 2014; revised 20 May 2014; accepted 27 May 2014 (Doc. ID 208919); published 1 August 2014

We propose a new type of confocal microscope using Fresnel incoherent correlation holography (FINCH). Presented here is a confocal configuration of FINCH using a phase pinhole and point illumination that is able to suppress out-of-focus information from the recorded hologram and hence combine the super-resolution capabilities of FINCH with the sectioning capabilities of confocal microscopy.

OCIS codes: (090.0090) Holography; (090.1995) Digital holography; (110.6880) Three-dimensional image acquisition; (180.1790) Confocal microscopy; (180.6900) Three-dimensional microscopy; (070.6120) Spatial light modulators.

http://dx.doi.org/10.1364/OPTICA.1.000070

Confocal imaging is commonly used for microscopy due to its ability to provide optical sectioning, improved contrast, and high-image resolution [1]. The concept of confocal microscopy was developed by Minsky in 1955 but found widespread use in biology only a few decades later. The reason for this delay is probably due to technological limitations at that time, as confocal imaging requires scanning over the entire imaged target [2,3]. Though confocal holographic systems that do not require scanning had been developed [4,5], they are unfortunately not suitable for fluorescence imaging [5], which is commonly practiced in microscopy for biological applications. In this Letter, we present, for the first time to our knowledge, a confocal configuration of Fresnel incoherent correlation holography (FINCH) [6]. FINCH is readily suitable for fluorescence microscopy and offers resolutions beyond the Rayleigh limit [7] but lacks the optical sectioning capabilities that are most important whenever thick objects are being imaged. These highly sought-after capabilities exist in the hereby proposed system and are achieved with the added cost of target scanning. These costs, however, can be mitigated to a large degree if a proper scanning methodology is used [1,8].

Before discussing the proposed confocal FINCH system, the working concept of FINCH is first briefly presented. A schematic configuration of a dual-lens FINCH system [9,10] is shown in Fig. 1(a). It is assumed that the object is spatially incoherent; thus light beams that are emitted or scattered from two different object points cannot interfere with each other, and the system is analyzed by considering a single point source object. In Fig. 1(a), a spherical light beam is emitted from the source point a_o, located at the front focal plane of the objective lens L_o, and propagates into the FINCH system. An input polarizer $P1$ is set at a 45° angle to the active axis of a spatial light modulator (SLM), $SLM1$, which allows the formation of two in-parallel imaging systems in a common-path single-channel configuration. The SLM modulates the phase of only the polarization components of the beam that are in parallel to its active axis. Polarization components of the input beam that are perpendicular to its active axis are not modulated; for them, the SLM is a transparent element. The system can thus be considered as two imaging systems, each acting with one of two orthogonal polarization components of light. In these systems, the input beam of light is collected by the objective lens L_o and then further concentrated by the lens L_c. In one of the two systems the SLM does not influence the beam, and an image is formed at the image point a_2; in the other, a converging diffractive lens is displayed on $SLM1$ and the beam is concentrated into the image point a_1.

To record a hologram of the maximum achievable resolution [7,9], a charge-coupled device (CCD) is positioned between the two image points, a_1 and a_2, so that a perfect overlap is achieved between the beam diverging from the image point a_1 and the beam converging toward the image point a_2. Note that interference can occur between these two beams, since they originate from the same point source, a_o, granted that the maximal optical path difference between the two is shorter than the coherence distance of the light source [9]. Further, note that the output polarizer $P2$ is essential and is used

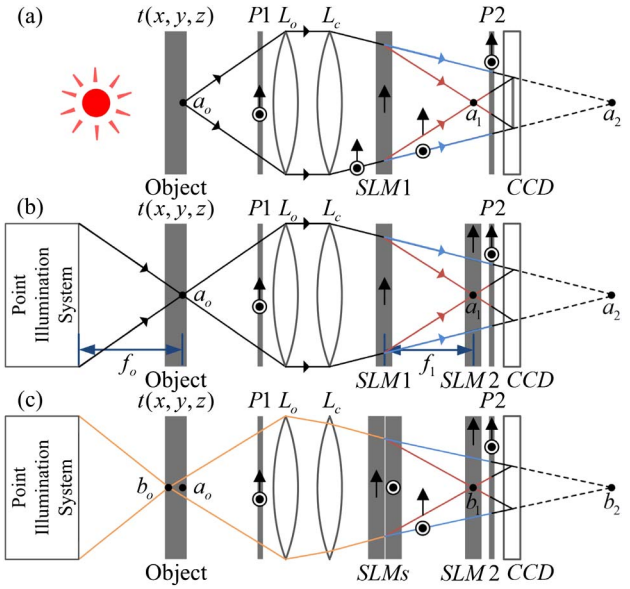

Fig. 1. Schematics of FINCH recorders: (a) a dual-lens FINCH system; (b), (c) the proposed confocal FINCH systems. $P1$ and $P2$, polarizers; L_o, objective lens; L_c, converging lens; $SLM1$ and $SLM2$, spatial light modulators; CCD, charge-coupled device.

to project the polarization components of the two beams into a common orientation. Usually, $P2$ is also set at a 45° angle to the active axis of $SLM1$, but other angles can be used to control the relative intensity of the two beams [11]. The intensity of the two-beam interference pattern is recorded by the CCD, giving rise to a 0th order term and two other terms attributed to the holographic image of a_o and its twin. A phase-shifting procedure [6,7,9–11], utilizing $SLM1$, requires at least three exposures and is performed so that only the holographic image term remains. The spatial incoherence of the object ensures that the final recorded FINCH hologram is a summation over the intensities of all point source interference patterns. The recorded object can then be reconstructed from the hologram through a digital Fresnel propagation to a specific reconstruction distance, z_r [9]. An additional feature of FINCH is that out-of-focus points are also recorded in the hologram. This, on one hand, can be advantageous when refocusing to planes of different depths is required, but on the other hand, it can impose noise and artifacts over the observed in-focus image. Next, we present a FINCH-based method that can section any desired plane out of the three-dimensional (3D) object distribution.

In a confocal FINCH system [Fig. 1(b)], a second SLM, $SLM2$, is positioned in the x y plane in which the image point a_1 is formed. A diffractive optical element, hereby referred to as a "phase pinhole," is displayed on $SLM2$. This phase pinhole is considered as one of the main innovations of the presented work. The phase pinhole at the scanning point (m, n) is described by the following equation:

$$G(\vec{r};\vec{r}_l) = \begin{cases} \exp(i\varphi_k) & |\vec{r}-\vec{r}_l-\vec{r}_s| \le r_1 \\ \exp(i\alpha|\vec{r}-\vec{r}_l-\vec{r}_s|)P(\vec{r}/R_2) & \text{Otherwise} \end{cases}, \quad (1)$$

with $\vec{r} = (x, y)$, $\vec{r}_l = (am, bn)$, and $\vec{r}_s = (x_s, y_s)$, and is composed of the actual pinhole part, $\exp(i\varphi_k)$, which is a circular area of radius r_1 set to a uniform phase modulation, surrounded by a mask of an axicon, $\exp(i\alpha r)$, where α is a parameter proportional to the axicon angle, $P(\vec{r}/R_2)$ denotes the circular aperture of $SLM2$, with a clear disk of radius R_2, a and b are scanning intervals in the x and y axes, respectively, and $\vec{r}_s$ is the starting point of the scanning. In the confocal FINCH system, for every scanning point (m, n), the uniform phase modulation at the pinhole region is set to three different φ_k values, usually 0°, 120°, and 240°, and $SLM1$ is no longer used for the phase-shifting procedure. Since the phase is changed only within the phase pinhole, any information carried by a wave that passes through $SLM2$ outside the phase pinhole and does not eventually interfere with the wave modulated by the phase pinhole is lost after the phase-shifting procedure. Overall, the proposed phase pinhole can be considered as a regular pinhole for the polarization components parallel to the active axis of $SLM2$ and as a clear aperture (of $SLM2$ dimensions) for the orthogonal polarization components. Accordingly, the proposed phase pinhole can perform properly even without displaying an axicon. Yet, by incorporating the axicon, light outside of the circular pinhole is actually deflected outside the sensor area. This, in turn, diminishes the amount of light that would otherwise reach the CCD and is only later removed digitally via phase shifting. Thus, the dynamic range of the CCD can be better exploited when the axicon is present. Eventually, we are left mostly with the information of the interference between light that passes through the phase pinhole of $SLM2$, with its orthogonal counterparts that are imaged at the point a_2.

The above described phase pinhole can efficiently achieve optical sectioning, as will be demonstrated promptly. However, better results can be achieved by incorporating a point illumination system, forming a complete confocal FINCH system. In a confocal FINCH system [Fig. 1(b)], the object points outside the scanning spot are eliminated from the recorded hologram. First, due to the point illumination, any of the object points that are not lit (i.e., are not within the cone of light) will not be recorded. Second, all points that are focused onto the region of $SLM2$ but fall outside of the phase pinhole are also rejected from the hologram. Points that fall partly within the phase pinhole will be attenuated in the recorded hologram, as their recorded fringe patterns will have a very limited aperture, rejecting most of their intensity. Most importantly, points whose images are out of focus on $SLM2$ are either completely eliminated from the recorded hologram (if their light does not propagate through the phase pinhole) or their intensity is greatly diminished, first due to the out-of-focus illumination and then due to an additional rejection of most of the information, since only a small part of their cone of light can propagate through the phase pinhole. This mechanism allows optical sectioning, with a tradeoff; unlike a regular FINCH system [Fig. 1(a)], which records holograms that contain the complete 3D information of the wide-field illuminated scene, here only a single point in space is properly imaged in a single

recorded hologram, and thus a scanning mechanism is required over the entire object.

Scanning of the entire object can be performed either mechanically, by translating the object in the x, y, and z axes, or electronically, without any mechanical intervention. In order to electronically control the position of the point illumination, one can introduce into the illumination system an additional SLM, for example, or other beam steerers (acousto-optical or electro-optical). As the object is scanned over the x y plane, the imaged point over $SLM2$ is formed at different positions, and so the phase pinhole mask is electronically centered to that point. For each scanning position (m, n), a single hologram is recorded (extracted from three exposures by a complete phase-shifting procedure). From each hologram a single point is reconstructed using the Fresnel diffraction integral formula for a single output point (a complete convolution is unnecessary), and all points from all of the recorded holograms can then be combined into a single image. Alternatively, as performed in the reported experiments, from each hologram a reconstruction of the entire input plane can be calculated; then, for each single pixel of the hologram, the maximum intensity value from all reconstructions is chosen, and a complete reconstruction of a specific x y plane is formed. In practice, just like in conventional confocal microscopy [1,8], many points can be imaged in parallel. This can be achieved, for example, by point illuminating multiple points on the same x y plane simultaneously, while a phase pinhole mask of multiple pinholes is displayed over $SLM2$. Of course, the distance between the illuminated points must be chosen so that proper optical sectioning can be achieved.

It is also possible to electronically scan at different depths (z positions) by controlling the focal length of the converging lens displayed on $SLM1$, but this will not allow a perfect overlap of the interfering beams on the CCD plane, and thus a resolution reduction is expected. A mechanical movement of the object at the z axis may then be preferred. This is a bearable cost, since this movement is only necessary once an x y plane scan is completed. Note that alternative FINCH configurations can be used to achieve perfect overlap at different z distances without a mechanical movement. This can be achieved by incorporating another SLM, placed with its active axis perpendicular to the active axis of $SLM1$ [see Fig. 1(c), in which two SLMs are stacked together and a perfect overlap can be achieved for any desired point source object]. This SLM can even replace the lens L_c if needed.

In Fig. 1(b), the point a_o is located on the optical axis and on the back and front focal planes of the point illumination system and the objective lens, respectively. Consider an arbitrary point located on the optical axis at a distance z_o from a_o. According to McCutchen's theorem, the complex amplitude at that point, $(0, 0, z_o)$, is given by $h_{\text{ill}}(z_o) = \mathcal{F}\{H_{\text{ill}}(2\lambda f_o^2 \rho)\}$, where the right-hand-side term is attributed to a one-dimensional Fourier transform of the radial aperture distribution H_{ill}, of the illumination system, f_o is its focal distance, λ is the central wavelength, and ρ is the variable of H_{ill} equal to r^2 [12]. The point $(0, 0, z_o)$ is imaged into two image points, $(0, 0, z_1 = z_o m_{a,1})$ and $(0, 0, z_2 = z_o m_{a,2})$, with complex amplitudes of $b_1 h_{\text{ill}}(z_o)$ and $b_2 h_{\text{ill}}(z_o)$, respectively, where b_1 and b_2 are constants, $m_{a,1}$ and $m_{a,2}$ represent the axial magnifications of the corresponding imaging systems, and the planes of $z_{1,2} = 0$ are at the imaged points a_1 and a_2, respectively. The waves associated with these two points interfere on the CCD plane, forming a fringe pattern from which the point $(0, 0, z_o)$ can be reconstructed. The interference pattern can be described as

$$I = \left| c_1 e^{i\varphi_k} Q\left(\frac{1}{l_1}\right) h_{\text{ill}}(z_o) h_{\text{det}}(m_{a,1} z_o) + c_2 Q\left(\frac{1}{-l_2}\right) h_{\text{ill}}(z_o) \right|^2, \tag{2}$$

where $Q(1/l_k) = \exp[i\pi l_k^{-1} \lambda^{-1} (x^2 + y^2)]$ is a quadratic phase function. The left-hand-side term in Eq. (2) is attributed to the wave associated with the image point $(0, 0, z_1 = z_o m_{a,1})$, a distance l_1 from the CCD, following its multiplication by the phase mask of the form of Eq. (1), which effectively multiplies the wave by a complex amplitude proportional to $h_{\text{det}}(z_1) = \mathcal{F}\{H_{\text{det}}(2\lambda f_1^2 \rho)\}$, with H_{det} affiliated with the imaging system forming that point and f_1 as its focal distance. Note that in the case of clear circular apertures, H_{ill} and H_{det} are Rect functions, so h_{ill} and h_{det} are Sinc functions. The right-hand-side term in Eq. (2) is attributed to the wave associated with the image point $(0, 0, z_2)$, a distance l_2 from the CCD.

Following a phase-shifting procedure, only one of the cross terms in Eq. (2) is left:

$$H(x, y) = c_o Q\left(\frac{1}{z_r}\right) h_{\text{ill}}(z_o) h_{\text{ill}}^*(z_o) h_{\text{det}}(m_{a,1} z_o) P(\vec{r}/R_H), \tag{3}$$

where $\vec{r} = (x, y)$, $z_r = l_1 l_2/(l_1 + l_2)$ is the reconstruction distance and $P(\vec{r}/R_H)$ denotes the circular aperture of the hologram, with a clear disk of radius R_H. This radius is determined by the overlap area of the two interfering waves. The recorded point can then be reconstructed from the hologram through a digital Fresnel propagation to the reconstruction distance z_r [9]:

$$\begin{aligned} h(u, v; z_o) &= H(x, y) * Q\left(\frac{1}{z_r}\right) \propto \\ & h_{\text{ill}}(z_o) h_{\text{ill}}^*(z_o) h_{\text{det}}(m_{a,1} z_o) \mathcal{F}\{P(\lambda z_r \vec{r}/R_H)\} \propto \\ & |h_{\text{ill}}(z_o)|^2 h_{\text{det}}(m_{a,1} z_o) \mathcal{J}\text{inc}\left(\frac{2\pi R_H}{\lambda z_r} \sqrt{u^2 + v^2}\right), \end{aligned} \tag{4}$$

where $*Q(1/z_r)$ denotes a Fresnel propagation (here, $*$ denotes a two-dimensional convolution) and $\mathcal{J}\text{inc}(r) \triangleq J_1(r)/r$ is the Bessel function of the first kind and of order one. Comparing Eq. (4) above with Eq. (5) of Ref. [9], we conclude that the transverse resolution of the proposed system, attributed to the $\mathcal{J}$inc term, is similar to a regular FINCH system; however, the longitudinal separation is much better in the proposed system and is comparable to that of a conventional confocal microscope, due to the z_o-dependent terms $|h_{\text{ill}}(z_o)|^2 h_{\text{det}}(m_{a,1} z_o)$.

In order to demonstrate the optical sectioning capabilities of the proposed system, the experimental setup described in Fig. 2

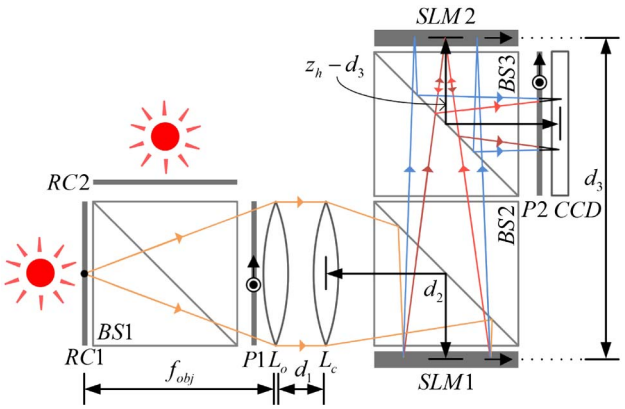

Fig. 2. Experimental setup: *RC*1 and *RC*2, resolution charts; *BS*1, *BS*2, and *BS*3, beam splitters; *P*1 and *P*2, polarizers; L_o, objective lens; L_c, converging lens; *SLM*1 and *SLM*2, spatial light modulators; *CCD*, charge-coupled device.

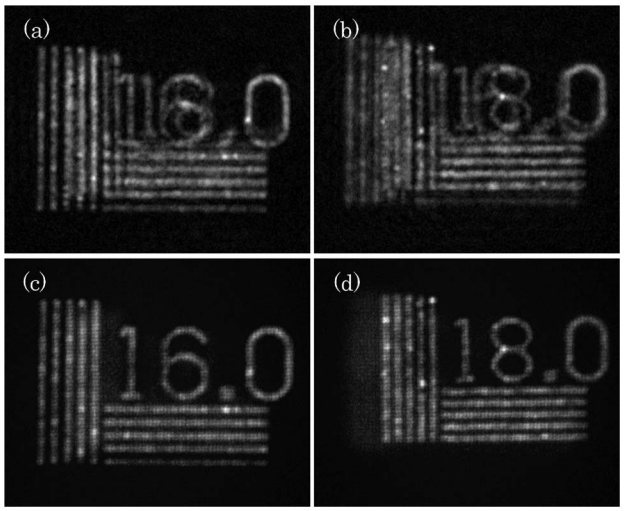

Fig. 3. Experimental results: (a) FINCH reconstruction of a 16.0 cycles/mm resolution chart located 30 cm away from the objective lens, with the 18.0 cycles/mm resolution chart at 31 cm; (b) FINCH reconstruction of a 18.0 cycles/mm resolution chart located 30 cm away from the objective lens, with the 16.0 cycles/mm resolution chart at 29 cm; (c), (d) the optical sectioning FINCH equivalents of (a) and (b), respectively.

was used. A beam splitter, *BS*1, was used as a beam combiner, with two resolutions charts (negative National Bureau of Standards 1963A), *RC*1 and *RC*2, positioned at a distance of 30 and 31 cm (for the x y plane scan of *RC*1) or 29 and 30 cm (for the scan of *RC*2) away from the objective lens, respectively. Together, the two charts can be considered as a 1 cm thick object. The resolution charts were back-illuminated using two LEDs (Thorlabs LED635L, 170 mW, $\lambda = 632.8$ nm, $\Delta\lambda = 15$ nm). Diffuser sheets were attached to the charts in order to imitate a scattering/illuminating object. The focal lengths of the objective lens L_o and the lens L_c were chosen as $f_{\text{obj}} = 30$ cm and $f_c = 150$ cm, respectively. For simplicity, we have replaced these two lenses with an equivalent lens with a focal length of $f_e = 25$ cm, implying that $d_1 = 0$ cm (Fig. 2). Other parameters in the system were: $d_2 = 10$ cm, $d_3 = 66.3$ cm, and $z_h = 90$ cm (which is the distance from *SLM*1 to the CCD and is the parameter that determines the transverse magnification of FINCH as $M_T = z_h/f_{\text{obj}}$). The two SLMs (Holoeye PLUTO, 1920 × 1080 pixels, 8 μm pixel pitch, phase-only modulation) were positioned at similar orientations, with their active axes in parallel, while the two polarizers, *P*1 and *P*2, were set at a 45° angle to these axes, and in parallel to each other. Since the two SLMs are reflective, two beam splitters, *BS*2 and *BS*3, were incorporated into the system so that the two SLMs were positioned orthogonally to the optical axis. This causes a loss of a large amount of light, which can be avoided by either by positioning the SLMs at a small angle, eliminating the beam splitters but requiring a careful compensation in the SLM displayed masks, or by using transmissive components (e.g., *SLM*1 can be replaced with a liquid crystal gradient index lens [13]).

In the experiments, we compared the results of a regular FINCH system (setting the phase mask of *SLM*2 to a constant zero modulation) and an optical sectioning FINCH system (with a phase pinhole displayed on *SLM*2). The phase pinhole radius was $r_1 = 44$ μm, surrounded by an axicon of parameter $\alpha = 2\pi \cdot 13 \cdot 10^{-3}/\lambda$, and the scanning over a grid of size 81 × 61 points on each plane was performed with pinhole displacements in the x and y axes of 40 μm. The exposure time was set to 1.25 s, implying a scanning time of roughly 5 h per plane. Note that in the reported experiments we do not use the proposed point illumination, and the entire object is illuminated at all times. This is to emphasize the contribution of the phase pinhole, which can be considered the most genuine part and newest contribution of this work, whereas scanning illumination systems are widely used in confocal microscopy [8]. It should be noted that such systems, in which the sectioning is performed solely by the phase pinhole, can be useful for imaging situations in which the observed scene cannot be illuminated as required.

The experimental results are presented in Fig. 3. Reconstruction results from regular FINCH holograms are presented in Figs. 3(a) and 3(b), for the resolution targets closest to the objective (*RC*1) and farthest from it (*RC*2), respectively. Here, the out-of-focus targets greatly diminish the quality of the reconstruction. The equivalents of the reconstructions of Figs. 3(a) and 3(b), resulting from the phase-pinhole-incorporated FINCH, are presented in Figs. 3(c) and 3(d), respectively. Unlike regular FINCH holography, the out-of-focus targets are highly attenuated, and so the in-focus targets appear with much detail, high contrast, and weak background artifacts. Hence, the optical sectioning capability of the proposed system is clearly demonstrated. It should be noted that once a single point illumination is incorporated into the system, the sectioning capabilities are expected to be further enhanced. Here, the out-of-focus target is illuminated with similar intensity to the in-focus target, unlike the case of point illumination, where object points will exhibit an illumination of less intensity that declines farther away from the location of the illuminated point.

To conclude, a new confocal FINCH configuration capable of optical sectioning has been proposed in this Letter, and a

simpler configuration of FINCH capable of sectioning has been demonstrated and compared with regular FINCH. The proposed system combines the super-resolution capabilities of FINCH with the sectioning capabilities of confocal microscopy. Together with the notable capabilities of FINCH for fluorescent microscopy, parallel illumination arrangements, and nonmechanical scanning schemes [8], we expect the proposed system to have an important role in microscopy in general and biological microscopy in particular. Other potential applications for the proposed system might include high lateral resolution tomography that is also capable of simultaneous imaging of passive reflecting surfaces and fluorescent objects.

FUNDING INFORMATION

National Institutes of Health (NIH) (U54GM105814); The Israel Ministry of Science and Technology (MOST); The Israel Science Foundation (ISF) (439/12).

REFERENCES

1. R. H. Webb, Rep. Prog. Phys. **59**, 427 (1996).
2. M. Minsky, Scanning **10**, 128 (1988).
3. W. B. Amos and J. G. White, Biol. Cell **95**, 335 (2003).
4. P.-C. Sun and E. N. Leith, Appl. Opt. **33**, 597 (1994).
5. R. Chmelík and Z. Harna, Opt. Eng. **38**, 1635 (1999).
6. J. Rosen and G. Brooker, Opt. Lett. **32**, 912 (2007).
7. J. Rosen, N. Siegel, and G. Brooker, Opt. Express **19**, 26249 (2011).
8. P. J. Verveer, Q. S. Hanley, P. W. Verbeek, L. J. Van Vliet, and T. M. Jovin, J. Microsc. **189**, 192 (1998).
9. B. Katz, J. Rosen, R. Kelner, and G. Brooker, Opt. Express **20**, 9109 (2012).
10. R. Kelner, J. Rosen, and G. Brooker, Opt. Express **21**, 20131 (2013).
11. G. Brooker, N. Siegel, V. Wang, and J. Rosen, Opt. Express **19**, 5047 (2011).
12. C. W. McCutchen, J. Opt. Soc. Am. **54**, 240 (1964).
13. G. Brooker, N. Siegel, J. Rosen, N. Hashimoto, M. Kurihara, and A. Tanabe, Opt. Lett. **38**, 5264 (2013).

Research Article Vol. 1, No. 2 / August 2014 / Optica 75

Absolute absorption cross-section measurement of a submonolayer film on a silica microresonator

JACK A. BARNES,[1] GIANLUCA GAGLIARDI,[2] AND HANS-PETER LOOCK[1,*]

[1]Department of Chemistry, Queen's University, Kingston, Ontario K7L 3N6, Canada

[2]Consiglio Nazionale delle Ricerche-Istituto Nazionale di Ottica (INO), Comprensorio "A. Olivetti," Via Campi Flegrei 34, 80078 Pozzuoli (Naples), Italy

*Corresponding author: hploock@chem.queensu.ca

Received 2 April 2014; revised 13 June 2014; accepted 17 June 2014 (Doc. ID 208781); published 6 August 2014

Conventional absorption spectroscopy is not nearly sensitive enough for quantitative overtone measurements on submonolayer coatings. While cavity-enhanced absorption detection methods using microresonators have the potential to provide quantitative absorption cross sections of even weakly absorbing submonolayer films, this potential has not yet been fully realized. To determine the absorption cross section of a submonolayer film of ethylene diamine (EDA) on a silica microsphere resonator, we use phase-shift cavity ringdown spectroscopy simultaneously on near-IR radiation that is Rayleigh backscattered from the microsphere and transmitted through the coupling fiber taper. We then independently determine both the coupling coefficient and the optical loss within the resonator. Together with a coincident measurement of the wavelength frequency shift, an absolute overtone absorption cross section of adsorbed EDA, at submonolayer coverage, was obtained and was compared to the bulk value. The smallest quantifiable absorption cross section is $\sigma_{\min} = 2.7 \times 10^{-12}$ cm^2. This absorption cross section is comparable to the extinction coefficients of, e.g., single gold nanoparticles or aerosol particles. We therefore propose that the present method is also a viable route to absolute extinction measurements of single particles.

OCIS codes: (230.3990) Micro-optical devices; (230.5750) Resonators.

http://dx.doi.org/10.1364/OPTICA.1.000075

1. INTRODUCTION

Single-molecule detection and single-atom detection rely largely on the measurement of excited-state fluorescence [1,2]. While single-particle absorption measurements, especially in the IR fingerprint region [3], are generally applicable and provide more chemical specificity, conventional absorption spectroscopy is not nearly sensitive enough for single-molecule measurements. In most commercial spectrometers absorption spectroscopy requires the measurement of a small intensity change on a large intensity background. While direct single-particle absorption detection therefore appears impossible with this approach, Celebrano *et al.* succeeded in detecting the shadow of a strongly absorbing molecule by focusing the light to a diffraction-limited spot [4]. Of course, surface-enhanced Raman scattering [5,6], surface-plasmon-resonance-enhanced detection [7], and near-field scanning optical microscopy also have approached and occasionally reached single-molecule or single-particle detection limits.

Optical microresonators of differing geometries have also been used previously as label-free and ultrasensitive chemical sensors reaching single-particle or single-molecule detection limits [8–18]. The resonance frequencies of the "whispering gallery" cavity modes (WGMs) are sensitive to the surface coverage and the refractive index of the adsorbed chemical species [11,19], while the optical absorption of the surface layer leads to a decrease of the quality (Q) factor [20] and can be retrieved

either from the reduction of power that is transferred to the resonator mode [21], from the decrease of the cavity ringdown time, or from the broadening of the resonance line. These cavity-enhanced absorption detection methods have, therefore, the potential to provide quantitative absorption cross sections of single particles. For microresonators this potential has, to the best of our knowledge, not yet been realized, although Pipino *et al.* measured absolute overtone absorption cross sections using a large monolithic folded optical cavity [22]. In most previous studies the presence of a particle placed in the mode field of a microresonator was inferred from, e.g., stepwise resonance frequency shifts [19] or incremental transfer of thermal energy into the resonator [8,9] and could not be readily quantified. In addition, a measurement of the total optical loss in the microresonator obtained from resonance lifetime or linewidth measurements does not permit us to distinguish losses due to molecular absorption from changes in the cavity coupling coefficient.

As we show in the present paper, the signal enhancement, which is provided here by an optical microcavity, is indeed quantifiable and provides a route to absolute absorption cross sections of either single particles or—here—of weak transitions at submonolayer coverages. We combined "conventional" phase-shift cavity ringdown measurements of Rayleigh backscattered light with phase-shift measurements of light bypassing the cavity and thereby obtain absolute values for the coupling coefficient and the cavity loss. The optical loss measurement can then be related to the surface coverage, which is obtained from the frequency shift of the WGM. With the assumptions made about the molecular dimensions, it is possible to calculate the absorption cross section.

Time-domain measurements have routinely been used to measure optical lifetimes in a variety of resonator configurations [23] including monolithic silica resonator cavities [22,24] and microresonators [25,26]. For such cavity ringdown time measurements the time-dependent intensity decay of a short optical pulse injected into the resonator is monitored. We apply an alternative approach that, instead, uses intensity-modulated light from a cw source and then measure the phase shift of light exiting the resonator. This approach is referred to as phase-shift cavity ringdown (PS-CRD) spectroscopy and has been used for mirror cavities [27,28], fiber-optic loops [29], and, more recently, silica microsphere resonators [30,31]. To demonstrate the sensitivity of the method we use the PS-CRD technique to measure the optical absorption of near-IR light through a weak overtone transition of ethylene diamine (EDA), $H_2N-CH_2-CH_2-NH_2$, that is adsorbed on the surface of a high-Q silica microsphere with a coverage of less than four monolayers. The compound was selected because its absorption spectrum and refractive index at 1.5 μm are well known. Also, the adsorption kinetics of EDA on silica have previously been characterized [32], and its vapor pressure is comparably high, allowing for a controlled dosing experiment.

2. EXPERIMENTAL SETUP

The silica microsphere (diameter of 273 μm, measured using the microscope built into the fusion splicer) was formed by melting the end of a single-mode optical fiber (Corning SMF-28E) in the electric arc of a fusion splicer. Another strand of single-mode optical fiber was tapered to a waist diameter of about 3 μm and used to couple light into the evanescent field of the microsphere's WGMs. A detailed description of the experimental setup regarding the microsphere and tapered waveguide may be found elsewhere [30].

The amplitude- and frequency-modulated light is coupled into either TE or TM WGMs of the microsphere. Rayleigh backscattering, from imperfections in the silica microsphere, equilibrates degenerate counterpropagating WGMs. Rayleigh backscattered light is coupled into the fiber taper and detected using a photodetector (Fig. 1) [33,34]. In addition, WGM resonances are observed by monitoring the light transmitted through the tapered waveguide using a second photodetector. A spectrum of a typical WGM resonance, viewed simultaneously in backscatter and transmission modes, is shown in references [35,36]. Frequency locking of the diode laser was achieved using the Pound–Drever–Hall (PDH) technique [37], as described previously [38]. The control signal was continuously acquired and is readily converted into the WGM frequency shift.

A distributed feedback (DFB) laser (Avanex 1905 LMI, linewidth: 2 MHz), amplified to a power of 9 mW using an erbium-doped fiber amplifier (Keopsys OI-BT-C-18-Sd-B-GP-FA), was employed to interrogate the microsphere. An ILX Lightwave ultra-low-noise current source (LDX-3620) was used with the DFB laser. At a fixed temperature, this laser

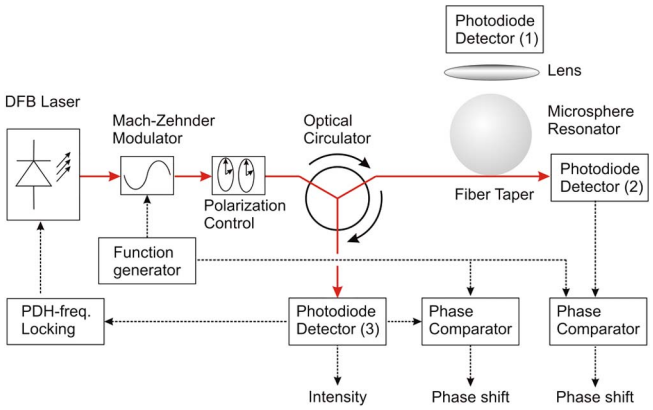

Fig. 1. Schematic representation of the experimental setup. The output of a distributed feedback (DFB) laser at 1549 nm is directed through an optical isolator and an erbium-doped fiber amplifier to a Mach–Zehnder modulator. The polarization of the amplitude-modulated beam is then polarization controlled before being coupled into a silica microsphere resonator. The Rayleigh backscattered light is directed though a circulator to a photodetector (PD) (3). The intensity and phase of the signal from the PD is measured using a lock-in amplifier. Photodiode (2) and another lock-in amplifier are used to measure the intensity and phase of light that is transmitted through the fiber taper. The backscattered light is also used to lock the center frequency of the laser to the cavity resonance with the Pound–Drever–Hall (PDH) method. The coverage is obtained from the frequency shift of the WGM as described below. The FM and AM frequencies are kept sufficiently different to allow the lock-in amplifiers to accurately extract intensity and, simultaneously, phase angle values without cross talk. Typically the Rayleigh-backscattered signal is used to lock the laser to the WGM resonance.

can be continuously current tuned over a wavelength range of 0.15 nm. The laser output was sinusoidally intensity modulated using a Mach–Zehnder modulator (JDS Uniphase) to a maximum frequency of 20 MHz. A polarization controller positioned after the modulator allowed the TE or TM resonator mode to be selectively excited. The mode polarization was determined by placing an InGaAs detector [Detector (1): Thorlabs DET10C] above the microsphere and recording the scattered radiation through an IR polarizer.

WGM resonances were detected through the Rayleigh backscattering of light coupled into the delivery waveguide. It is well known that Rayleigh backscattering from imperfections in the silica microsphere quickly equilibrates degenerate counterpropagating cavity modes [34]. A fiber-optic circulator directed the backscattered light to a fiber-coupled 150 MHz bandwidth InGaAs detector [Detector (2): Thorlabs PDA10CF]. Light transmitted though the delivery fiber was monitored using another InGaAs detector [Detector (3): Thorlabs DET10C]. RF lock-in amplifiers (Stanford Research Systems Model SR844) processed the detector outputs, providing intensity and phase angle measurements that were referenced to the laser intensity modulation.

A quartz crystal microbalance (QCM) was placed under the microsphere and taper. The fiber taper, microsphere, and microbalance sensor element were located under a 5 cm^3 glass dosing chamber into which EDA vapor was introduced. A low flow of nitrogen was passed over neat EDA (vapor pressure of 11.3 Torr at room temperature), carrying the vapor through a Teflon valve into the dosing chamber. This entire apparatus was contained within a Plexiglas enclosure and purged with dry nitrogen, which served to reduce contamination and the adsorption of water vapor onto the microsphere.

3. POUND–DREVER–HALL FREQUENCY LOCKING

To lock the laser to a WGM, we use the PDH method [37] as described earlier [38,39]. Briefly, the DFB laser is current modulated, resulting in a frequency modulation (FM) of 10–50 MHz in addition to the 1–20 MHz amplitude modulation (AM) described above. When the resulting detector signal, which contains the beat notes at the FM frequency, is mixed with the FM oscillator and low-pass filtered, a dispersive-like error signal is obtained that is returned to the laser driver and used to lock the laser center frequency.

We select the FM frequency such that the error signal remains proportional to the derivative of the WGM line shape, i.e., we work in a regime in which the modulation frequency is small compared to the WGM linewidth. The polarity of the error signal indicates the relative tuning of the laser with respect to the resonance center frequency. This signal is applied to a servo circuit, where it is amplified, integrated, and fed back to the current driver as a correction signal. As a consequence, the laser frequency locks tightly to the WGM resonance with an electrical bandwidth of 35 kHz. If the WGM shifts in frequency due to, for example, adsorption of molecules on the microsphere surface, the magnitude of the correction signal applied to the laser changes accordingly. Knowledge of the transfer function of the laser driver (mA/mV), as supplied by the manufacturer (ILX Lightwave), together with the measured tuning characteristics of the DFB laser (pm/mA), allows us to calculate the frequency shift from the control voltage change.

4. REAL-TIME MEASUREMENT OF THE SURFACE COVERAGE

The surface coverage of the silica sphere with EDA was measured simultaneously using both the frequency shift of the WGM and a QCM. The QCM was positioned directly below the fiber taper and microsphere. The surface of the quartz crystal supports a gold electrode, which occupies about 25% of the surface area. While the gold electrode of the QCM presents a different surface compared to the silica microsphere, both are expected to adsorb EDA and coverages may be compared. Surface coverages of the QCM were calculated from the quartz crystal resonance shifts using the Sauerbrey equation [40]. An analog-to-digital converter was used to simultaneously measure the servo-control voltage, the QCM frequency, the backscattered signal intensity, and the phase angles from the lock-in amplifiers, while the laser was locked to the WGM. These values were displayed, and simultaneously recorded, on a computer through a LabView program (Fig. 2).

We note that with a number of assumptions it is also possible to independently determine the coverage from the wavelength shift of the WGM. Teraoka and co-workers have derived an expression describing the wavelength shift of a WGM due to molecules adsorbed on a microsphere surface [10,19,41]. Their calculation is based on the polarization induced in an adsorbed molecule by the evanescent tail of the WGM. Using a perturbation approach for calculating the wavelength shift induced by a change, $\delta\varepsilon_r$, in the dielectric

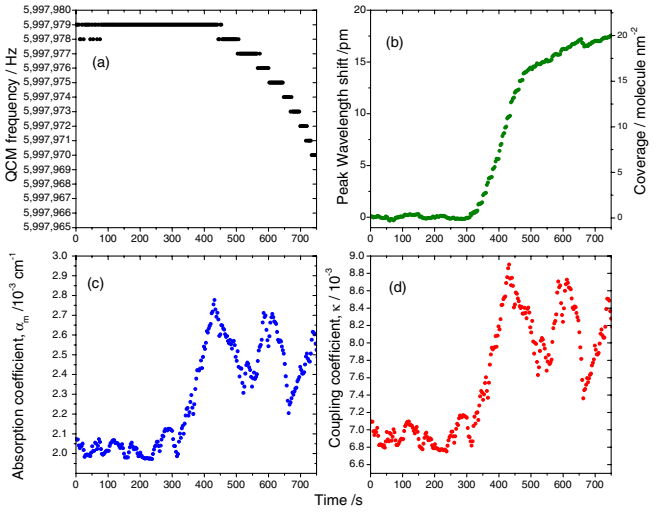

Fig. 2. Response of WGM to dosing of EDA onto the silica microsphere surface. Very low concentrations of EDA have been mixed into a stream of dry nitrogen starting at $t = 300$ s. (a) Frequency response of the QCM. The readout is digitized with 1 Hz resolution. (b) Wavelength shift, $\delta\lambda$, of the WGM resonance as measured by the correction voltage supplied to the PDH-locked DFB laser, (c) absorption coefficient, α_m, and (d) coupling coefficient, κ, calculated from the observed phase shifts and Eqs. (3)–(5).

medium external to the microsphere with radius R, they derived the expression for the fractional change in the TE-mode wave vector (see also Appendix A):

$$\left(\frac{\delta k}{k_0}\right)_{\mathrm{TE}} = -\frac{\alpha_t \theta}{\varepsilon_0 R}\frac{1}{(n_1^2 - n_2^2)}. \quad (1)$$

For the first-order TM mode one requires a correction term,

$$\left(\frac{\delta k}{k_0}\right)_{\mathrm{TM}} \cong \left(\frac{\delta k}{k_0}\right)_{\mathrm{TE}}\left[2 - \left(\frac{n_2}{n_1}\right)^2\right], \quad (2)$$

and would have to use both the tangential and the radial component to the polarizability instead of α_t as is appropriate for a TE mode. This expression holds for a surface layer that is much thinner than the wavelength of the light—as is the case in the present experiments. Here, $n_1 = 1.444$ is the microsphere refractive index, and $n_2 = 1.0$ is that of the surroundings. If the refractive index of the adsorbed material is assumed constant, Eq. (1) can be used to relate the wavelength shift $\delta\lambda/\lambda_0 = -\delta k/k_0$, to the surface coverage, θ. The transverse component of the polarizability of the adsorbed molecule, α_t, and the radial component of the polarizability, α_r, depend on the components of the polarizability tensor and on the orientation of the adsorbed molecule on the surface [42]. Using calculated values for the diagonal tensor components for gas phase EDA, it can be shown that α_t varies by, at most, 6% from the isotropic polarizability value of EDA ($\alpha_{\mathrm{iso}} = 6.7 \times 10^{-24}$ cm^3) [43]. Hence, orientation effects can be ignored in this case. Also, given the low concentration of EDA, the thermal conductivity of the vapor surrounding the microsphere differs insignificantly from that of pure nitrogen present before the dosing. Therefore, frequency shifts due to a change in thermal conductivity are expected to be negligible.

5. RESULTS AND ANALYSIS

Figures 2(a) and 2(b) give the surface coverage values obtained from the QCM and those calculated from the WGM resonance wavelength shift using Eq. (1). The maximum dosage level indicated by the QCM is a factor of 4 greater than that based on the WGM wavelength shift. This difference is not surprising, since the microsphere surface is atomically smooth silica, whereas the sensitive region of the QCM is principally a comparably rough evaporated gold surface.

It has been shown that gold reversibly adsorbs amines [44] in a manner highly dependent on surface roughness. We therefore use the more reliable coverages obtained from Eq. (1) instead of the values given by the QCM. It is also known that EDA adsorbs strongly to silica through interaction with surface silanol groups [32]. Given the response from the QCM [Fig. 2(a)], we can assume that in our case the observed perturbations of the WGM cavity resonance are due to adsorbed EDA, rather than vapor. In addition, we have to consider that water adsorbs to silica and the silica surface may originally be covered with a few monolayers of water that are partially displaced by EDA.

As can be seen in Fig. 2(a), the QCM response is discretized due to its 1 Hz frequency resolution, whereas the microsphere frequency shift is continuous. Figure 2(b) also shows that upon exposing the sphere to EDA, the WGM resonance frequency shifts to longer wavelengths as expected.

EDA adsorbs onto silica through interactions with surface silanol groups, which are the major surface species, even in the presence of water vapor [32]. The average surface density of silanol groups on silica is estimated at 4.9 nm^{-2} [45], which suggests that, based on the resonance shift data, about four monolayers of EDA are deposited on the microsphere over the course of this experiment. By comparison, the "footprint" of an EDA molecule in the bulk liquid phase can be estimated from the density (0.9 g/mL) and the molar mass (60.1 g/mol) as 0.23 nm^2/molecule, which is somewhat larger than expected from the *ab initio* "diameter" of the isolated molecule (~0.13 nm^2/molecule). The density of the bulk EDA layers (4–7 molecules/nm^2) is therefore comparable to the surface density of the silanol groups (about 4.9 nm^{-2}).

Figure 2(b) shows a pronounced change in deposition rate after about two monolayers were deposited. We speculate that the fast formation of the first two monolayers is driven by the strong hydrogen bonds between the silanol groups and the amine moiety of the EDA, whereas the slower formation of the next two monolayers is governed by weaker EDA/EDA interactions. It has been shown that EDA strongly binds through chemisorption on silica via a proton transfer reaction with the surface silanol groups [32]. Additional physisorbed layers will bond through amine hydrogen bonding interactions, which have a lower energy on the order of 13 kJ/mole [46]. The oscillations in Figs. 2(c) and 2(d) were found to occur in almost all dosing experiments and are not yet understood. While we expect that the frequency shift (coverage), as well as absorption and coupling coefficients, will approach an asymptotic value given by the vapor pressure of the gas, the free energy of adsorption, and the temperature of the gas and the substrate, it is not required that this limit is reached monotonously. The oscillations may then be a reflection of reorientation and spatial redistribution processes.

In our experiment, optical absorption of EDA through its N–H stretch overtone band at 1549 nm is measured with the PS-CRD technique. In a previous application of the phase-shift technique to microspheres, the ring-cavity model of Rezac [47] was used to calculate the phase shift observed in the light transmitted through the delivery fiber [30]. This transmitted light represents the superposition of a portion of the incident field and the forward scattered field of the microsphere. The phase shift observed in the transmitted light is given by [30]

$$\Delta\Phi_{\mathrm{trans}} = 2\tan^{-1}\left[\frac{\Omega n_{\mathrm{eff}} L}{2c}\frac{2\ln\Gamma}{(\ln\Gamma)^2 - (\alpha_m L/2)^2}\right], \quad (3)$$

where Ω is the angular laser intensity modulation frequency, n_{eff} is the effective refractive index of the WGM, L is the circumference of the microsphere, $\kappa = \sqrt{1-\Gamma^2}$ is the coupling constant between the taper and microsphere, and α_m is the attenuation coefficient.

In addition, we also recorded the phase shift of the backscattered field. It has been shown recently that the phase shift for the backscattered light is [35,36]

$$\Delta\Phi_{bs} = 2\tan^{-1}\left[\frac{2\Omega/\tau}{\Omega^2 - \left(1/\tau^2 + 1/\gamma^2\right)}\right], \quad (4)$$

where τ is the ringdown time of the microsphere, given as

$$\tau = \frac{Ln_{eff}}{c_0(\alpha_m L - 2\ln\Gamma)}, \quad (5)$$

and γ is the coupling constant between near-degenerate clockwise and counterclockwise WGMs [35,36].

The coupling constant, γ, was assumed to remain unchanged throughout the adsorption process. This was verified experimentally by measuring the frequency-dependent phase shift of a microsphere WGM with first a clean surface and then a surface covered by approximately two monolayers of EDA. It was found that the ringdown time decreased with dosing, as expected, while the coupling constant, γ, remained unchanged (Fig. 3). It appears that the clockwise/counterclockwise modal coupling is dominated by intrinsic scattering centers within the microsphere and not by adsorbed species on the microsphere surface.

From Eq. (4) one expects that the phase shift of the intensity-modulated backscattered light varies approximately linearly with the AM frequency for low modulation frequencies, Ω. For high modulation frequencies deviations from linearity are expected, as described in Ref. [35]. A fit of the phase-shift values obtained at different AM frequencies to Eq. (4) yields the ringdown time τ and the coupling constant

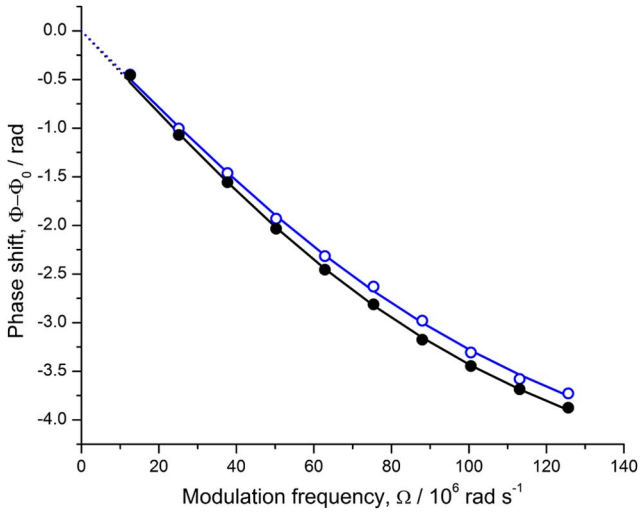

Fig. 3. Observed phase delay of the amplitude-modulated light of a WGM of a clean microresonator (solid black circles) and after dosing (open blue circles). From a fit to Eq. (4) (lines), ringdown times of $\tau = 12.3 \pm 0.2$ and 11.4 ± 0.2 ns were obtained, respectively. At a vacuum wavelength of 1.549 μm ($\nu = 1.93 \times 10^{14}$ Hz), this corresponds to a Q-factor of about 1.5×10^7. The coupling constants of $\gamma = 31 \pm 3$ and 30 ± 4 ns were unchanged.

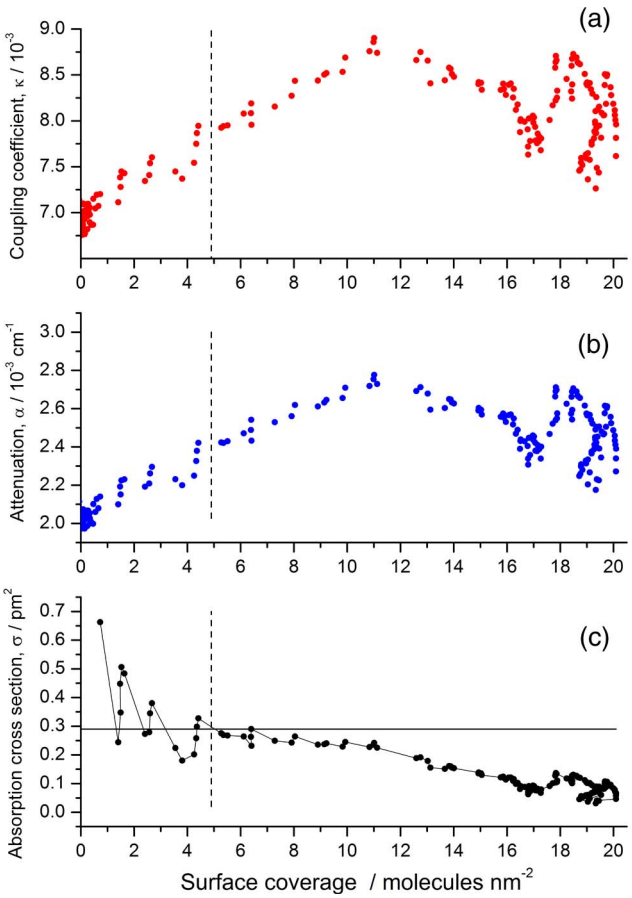

Fig. 4. Data shown in Fig. 2 were processed using Eqs. (3)–(5) to obtain (a) the coupling coefficient, κ, (b) the attenuation coefficient, α_m, and (c) the molecular absorption cross section, σ, as a function of the surface coverage, which was calculated from the frequency shift of the WGM [Fig. 2(b)] and Eq. (4). The vertical dashed line indicates the approximate coverage corresponding to one monolayer, and the horizontal line in (c) indicates the absorption cross section of bulk liquid EDA, σ_{bulk}.

γ. The quality factor is given by $Q = 2\pi\nu\tau$ (Fig. 3), where ν is the optical frequency of the light.

Based on the ringdown time at zero coverage, the Q-factor is $\sim 1.5 \times 10^7$ for the particular TE mode used. Calculating Q-factors based on ringdown time eliminates complications due to thermal effects, which are known to influence Q-factor determinations based on linewidth measurements [48].

By recording the phase shift in transmission mode, $\Delta\Phi_{trans}$, and backscatter mode, $\Delta\Phi_{bs}$, simultaneously at a fixed Ω, one can use Eqs. (3)–(5) to calculate the ringdown time (τ), the absorption coefficient (α_m), and the coupling coefficient (κ) throughout the dosing process [Figs. 2(c) and 2(d)]. These measurements can then be correlated to the coverage of the microsphere with EDA, which is obtained from the frequency shift [Fig. 2(b)] to obtain Fig. 4.

6. PHOTOTHERMAL EFFECTS

Photothermal effects, such as desorption of EDA upon heating of the sphere on resonance, have to be considered. When the

laser is locked on a WGM resonance, imperfections in the microsphere absorb part of the circulating light, leading to heating of the microsphere. We found that with increasing input power, the resonance shifts to longer wavelengths, and attribute that shift to an increase in the microsphere's temperature [49]. Using published values for the thermo-optic coefficient and linear expansion coefficient of silica [50], it is estimated that the temperature of the microsphere is ~10 K higher than the QCM when the laser is locked to the WGM resonance. Given the relatively high binding energies involved, the 10 K temperature increase of the microsphere is expected to have a negligible effect on the degree of adsorption of the first two monolayers but may affect the physisorbed EDA layers at higher coverage.

7. DISCUSSION

In Fig. 4(a) the coupling coefficient, κ, governing the interaction between the taper and the microsphere resonator is seen to increase linearly until a coverage of about 10 molecules/nm^2, i.e., roughly two monolayers, is reached. This may appear surprising, since, to the best of our knowledge, in all previous studies the coupling parameter is assumed to be independent of the surface coverage. It appears that this premise is not necessarily true. The change of κ with the surface coverage may be explained by the adsorbed layer of EDA on the sphere and fiber that will, especially in the narrow fiber taper, influence the index of the propagated mode and thereby the phase-matching condition.

As expected, the overtone absorption, α_m, increases approximately linearly but is then found to decrease gradually as more than about one or two monolayers are deposited [Fig. 4(b)]. Oscillations of the absorption were observed beyond about two monolayers of coverage and presently lack a definitive explanation. These oscillations may be due to restructuring and reorientation of the adsorbate layers as a function of surface coverage. Oscillations were observed in all experiments but were sometimes found at lower coverages.

The overtone absorption cross section of one monolayer is estimated from

$$\sigma = \frac{(\alpha_m - \alpha_0) l_{\mathrm{EDA}}}{f_{\mathrm{thin}} \theta}, \tag{6}$$

where $\alpha_0 = 0.0020$ cm^{-1} is the optical loss of the WGM before dosing, $l_{\mathrm{EDA}} = 360$ pm is the estimated length of an EDA molecule and our estimate for the thickness of one monolayer, and $f_{\mathrm{thin}} = 1.05 \times 10^{-5}$ is the fraction of the TE-WGM interacting with a film of 360 pm thickness (see Appendix B).

Using the value for the absorption coefficient at one monolayer of coverage ($\theta = 4.9 \times 10^{14}$ molecules/cm^2), the experimental absorption cross section is calculated as $\sigma = 2.7 \times 10^{-21}$ cm^2. By comparison, the bulk absorption cross section of EDA liquid at 1550 nm is $\sigma_{\mathrm{bulk}} = 2.9 \times 10^{-21}$ cm^2 [51]. For molecules as small as EDA, light attenuation by scattering is negligible [52].

The small difference between the measured cross section and the bulk value is readily explained. We emphasize that many of the values used in this estimate of the absorption cross section, such as l_{EDA}, f, θ, and $\alpha_m L$, have errors estimated to be in the 10%–20% range, and even the bulk absorption cross section of liquid EDA, σ_{bulk}, [51], may be slightly inaccurate.

Using Eq. (6) one can readily calculate the molecular absorption cross section at other coverages [Fig. 4(c)]. We find a gradual decrease in the absorption cross section after a coverage of one or two monolayers has been reached. This effect can again be explained using reorientation effects, or possibly using clustering and island formation. The TE-WGM used in this experiment has its electric field parallel to the microsphere surface. As a consequence, N–H bonds oriented parallel to the surface will be preferentially excited. Deviation from this optimal orientation will cause a reduced interaction with the mode field and reduced absorption. While it may appear that oscillations at submonolayer coverages are then attributable to a reorientation of the surface-bound amine group, one has to consider that the unbound amine group remains free to rotate. Similarly, the decrease in the apparent absorption cross section at higher coverage is likely not due to orientation effects, which cannot explain an absorption cross section that is so much lower than the bulk value. Other geometric effects such as a reduced density of the topmost layer appear to be a more likely cause for the decreased effective absorption cross section. Since we are dealing with only a few layers of molecules, it is possible that subsequent deposition may affect already deposited layers, causing a reconstruction of layers that interact more or less favorably with the microresonator field, and thereby lead to a variable absorption cross section.

By analogy to the adsorption isotherms of ammonia on silica [53], we expect that the interaction of EDA with surface silanol groups on the thermally annealed silica sphere results in an initial chemisorbed layer, which is strongly bound by hydrogen bonds or by electrostatic interactions after proton transfer (Fig. 5). Subsequent layers are physisorbed. It is therefore likely that EDA follows a Brunauer–Emmett–Teller-type adsorption isotherm. This hypothesis is consistent with the reduced effective absorption cross section after about two monolayers are formed [Fig. 4(c)].

When benchmarking the sensitivity of the PS-CRD measurements against those reported before, we calculate from Fig. 2(c) or Fig. 4(b) that the minimal detectable absorption loss is about $\alpha_{\mathrm{min}} = 5 \times 10^{-5}$ cm^{-1}, or $\alpha_{\mathrm{min}} L = 4.2 \times 10^{-6}$. From Eq. (4) one can determine that the smallest quantifiable absorption cross section is $\sigma_{\mathrm{min}} = 2.7 \times 10^{-12}$ cm^2. Assuming a coverage of $\theta = 1/1500$ μm^{-2} (i.e., one particle in the evanescent mode volume), it is then apparent that one should be able to perform an absolute measurement of the absorption cross section of a single particle with this method as long as the optical loss per particle exceeds $\sigma_{\mathrm{min}} = 2.7 \times 10^{-12}$ cm^2 (270 nm^2). This absorption cross section and the molecular dimensions are comparable to those of, e.g., single gold nanoparticles, or the scattering cross sections of aerosol particles.

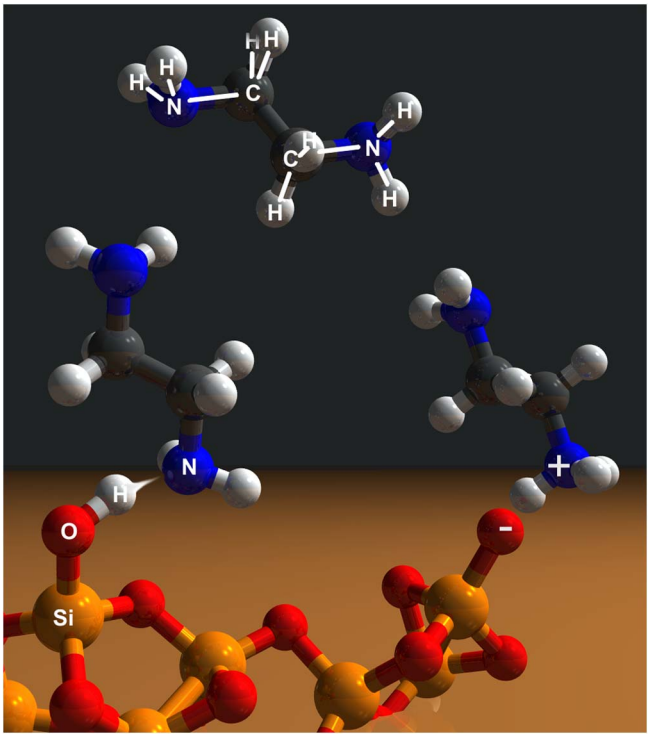

Fig. 5. Schematic depiction of EDA molecules adsorbed to silica through either hydrogen bonding to a surface silanol group (left molecule), electrostatic interactions following proton transfer (right), or weak dispersion forces (top). (Image inspired by Fig. 3 of Ref. [32]).

We therefore propose that the present method is a viable route to absolute absorption or scattering measurements of single particles.

The above method requires some prior knowledge about the adsorbed molecule. To determine the absorption cross section as was done here, one needs a reliable value for the transverse polarizability (TE mode) or both transverse and radial polarizabilities (TM mode). For most molecules with a flexible carbon frame, the value for the isotropic polarizability is expected to be quite similar to both values and is readily accessible through the refractive index and, e.g., the Clausius–Mosotti relation. Of course, one may invert the problem and calculate the polarizability from a known absorption cross section.

APPENDIX A: DERIVATION OF EQ. (1)

Teraoka *et al.* have derived an expression describing the wavelength shift of a WGM due to molecules adsorbed on a microsphere surface [10,19,41]. Their calculation is based on the polarization induced in an adsorbed molecule by the evanescent tail of the WGM. The interaction energy between the induced dipole and the evanescent field provides a first-order correction to the WGM energy. Using a perturbation approach for calculating the wavelength shift induced by a change, $\delta\varepsilon_r$, in the dielectric medium external to the microsphere, they derived the following expression for the fractional change in the wave vector:

$$\left(\frac{\delta k}{k_0}\right) = -\frac{\int_{V_p} \delta\varepsilon_r \mathbf{E_0^*}\cdot\mathbf{E_p}\mathrm{d}\mathbf{r}}{2\int_V \varepsilon_r \mathbf{E_0^*}\cdot\mathbf{E_0}\mathrm{d}\mathbf{r}}, \tag{A1}$$

where $\mathbf{E_0}$ is the unperturbed field of the microsphere and $\mathbf{E_p}$ is the perturbed field. The integral in the numerator is over the volume of the external perturbing medium, and that in the denominator is over all space. This expression applies to both TE and TM modes. For the adsorption of a thin layer ($\Delta R \ll \lambda_0$) of molecules onto a microsphere of radius R, this expression reduces to

$$\left(\frac{\delta k}{k_0}\right)_{\mathrm{TE}} = -\frac{1}{R(n_1^2 - n_2^2)}\int_R^{R+\Delta R}(n_p(r)^2 - n_2^2)\mathrm{d}r, \tag{A2}$$

where $n_1 = 1.444$ is the microsphere's refractive index, $n_2 = 1.0$ is that of the surrounding air, and $n_p(r)$ is that of the adsorbed material, here EDA. If the refractive index of the adsorbed material is assumed constant, Eq. (A2) can be related to the surface coverage, σ, through the equation

$$\left(\frac{\delta k}{k_0}\right)_{\mathrm{TE}} = -\frac{\alpha_t \sigma}{\varepsilon_0 R}\frac{1}{(n_1^2 - n_2^2)}, \tag{A3}$$

where α_t is the transverse polarizability of the adsorbed molecule. The transverse component of the polarizability depends on the components of the polarizability tensor and on the orientation of the adsorbed molecule on the surface [42]. Equations (1) and (A3) depend on the value of the transverse polarizability of the adsorbed molecule for TE modes and on both radial and transverse polarizabilities for TM modes. In our case of EDA, theoretical values are available for the diagonalized polarizability tensor components [43]. From these values we determined the transverse and radial polarizability components as $6.7\times10^{-24}\ \mathrm{cm}^3 < \alpha_t < 7.1\times10^{-24}\ \mathrm{cm}^3$ and $5.7\times10^{-24}\ \mathrm{cm}^3 < \alpha_r < 6.6\times10^{-24}\ \mathrm{cm}^3$, respectively. Our estimate for the isotropic polarizability of $6.7\times10^{-24}\ \mathrm{cm}^3$ is therefore close to the value for α_t and also agrees well with the isotropic polarizability calculated from the refractive index using the Clausius–Mosotti relation, $7.0\times10^{-24}\ \mathrm{cm}^3$. Note that in all calculations the small correction to the real part of the complex polarizability due to the absorption band at 1550 nm was neglected.

APPENDIX B: ESTIMATE OF THE VOLUME FRACTION, f, OF THE EVANESCENT WAVE IN EQ. (6)

To estimate the fraction of the WGM volume that interacts with the adsorbed molecular layer, we require the fraction of the WGM propagating in the evanescent wave. Assuming first that the layer is homogeneous and thick compared to the penetration depth of the evanescent wave, we can, for a TE mode, write the ratio of the evanescent field to the field inside the sphere as [19]

$$f_{\text{thick}} = \frac{\varepsilon_m \int_{r=R}^{\infty} j_l^2(k_0 n_s R)\exp(-2(r-R)/r_{ev}) r^2 \mathrm{d}r \int_{\phi=0}^{2\pi}\int_{\theta=0}^{\pi}[Y_l^m(\phi,\theta)]^2 \sin\theta \mathrm{d}\theta\mathrm{d}\phi}{\varepsilon_s \int_{r=0}^{R} j_l^2(k_0 n_s r) r^2 \mathrm{d}r \int_{\phi=0}^{2\pi}\int_{\theta=0}^{\pi}[Y_l^m(\phi,\theta)]^2 \sin\theta \mathrm{d}\theta\mathrm{d}\phi}$$
$$\approx \frac{\varepsilon_0 n_m^2 j_l^2(k_0 n_s R)\int_{r=R}^{\infty}\exp(-2(r-R)/r_{ev}) r^2 \mathrm{d}r}{\varepsilon_0 n_s^2 j_l^2(k_0 n_s R)\frac{R^3}{2}\frac{n_s^2-n_m^2}{n_s^2}} \approx (R^2 r_{ev}/2 + R r_{ev}^2/2 + r_{ev}^3/4)\frac{2}{R^3}\frac{n_m^2}{n_s^2-n_m^2} \approx \frac{r_{ev}}{R}\frac{n_m^2}{n_s^2-n_m^2} \approx \frac{\lambda_0}{2\pi R}\frac{n_m^2}{(n_s^2-n_m^2)^{3/2}}, \quad \textbf{(B1)}$$

where we integrated the spherical Bessel function j_l according to Lam *et al.* [54] and made use of the evanescent field decay length $r_{ev} \approx (\lambda_0/2\pi)(n_s^2 - n_m^2)^{-1/2} \ll R$.

The refractive index of the microresonator sphere material at $\lambda = 1.55$ μm was calculated from the Sellmeier coefficients for silica as $n_s = 1.444$. Assuming that a sphere with a 300 μm diameter is suspended in vacuum ($n_m = 1$), only 0.14% of the TE-WGM field is in the evanescent wave. This number increases to 1.3% if the surrounding medium is water ($n_m = 1.31$) and 7.3% if $n_m = 1.40$.

The present case is slightly more complicated, since the WGM interacts only with the thin EDA layer of subwavelength thickness with a refractive index $n_{\text{EDA}} = 1.4413$ that is close to that of the silica microsphere, n_s. Given that only a small fraction of the WGM power resides in air, we can approximate the fraction of the TE mode field in the overlayer as the ratio between the field in the EDA layer and that inside the sphere, i.e., as

$$f_{\text{thin}} \approx \frac{\varepsilon_{\text{EDA}} \int_{r=R}^{R+\Delta R} j_l^2(k_0 n_s R) r^2 \mathrm{d}r \int_{\phi=0}^{2\pi}\int_{\theta=0}^{\pi}[Y_l^m(\phi,\theta)]^2 \sin\theta \mathrm{d}\theta\mathrm{d}\phi}{\varepsilon_s \int_{r=0}^{R+\Delta R} j_l^2(k_0 n_s r) r^2 \mathrm{d}r \int_{\phi=0}^{2\pi}\int_{\theta=0}^{\pi}[Y_l^m(\phi,\theta)]^2 \sin\theta \mathrm{d}\theta\mathrm{d}\phi}$$
$$\approx \frac{\varepsilon_0 n_{\text{EDA}}^2 j_l^2(k_0 n_s R)\left(\frac{(R+\Delta R)^3}{3} - \frac{R^3}{3}\right)}{\varepsilon_0 n_s^2 j_l^2(k_0 n_s (R+\Delta R))\frac{(R+\Delta R)^3}{2}\frac{n_s^2-n_m^2}{n_s^2}} \approx \frac{2}{3}\frac{(R+\Delta R)^3 - R^3}{(R+\Delta R)^3}\frac{n_{\text{EDA}}^2}{n_s^2-n_m^2}. \quad \textbf{(B2)}$$

Here, we assumed that the field (value of the squared spherical Bessel function) is constant over the thickness of the EDA layer and that $n_s \approx n_{\text{EDA}}$. Using $n_s = 1.4439$, $n_{\text{EDA}} = 1.4413$, $n_m = 1.0$, $R = 136$ μm, and, for one monolayer, $\Delta R = 0.36$ nm, one obtains $f_{\text{thin}} = 1.05 \times 10^{-5}$ independent of the wavelength of the light. The actual fraction of the total WGM residing in the overlayer is slightly less, since we neglected the fraction of the light traveling outside the overlayer in the denominator of Eq. (B2). For a TM-polarized WGM the fraction, f, depends on the value assumed for l, and the expression is more complicated.

FUNDING INFORMATION

Consiglio Nazionale delle Ricerche; Natural Sciences and Engineering Research Council of Canada (NSERC).

ACKNOWLEDGMENTS

We thank John Saunders for writing the LabView program and Saverio Avino for his contributions to the PDH-laser locking setup.

REFERENCES

1. J. Goldwin, M. Trupke, J. Kenner, A. Ratnapala, and E. A. Hinds, "Fast cavity-enhanced atom detection with low noise and high fidelity," Nat. Commun. **2**, 418 (2011).
2. M. Pirchi, G. Ziv, I. Riven, S. S. Cohen, N. Zohar, Y. Barak, and G. Haran, "Single-molecule fluorescence spectroscopy maps the folding landscape of a large protein," Nat. Commun. **2**, 493 (2011).
3. X. J. G. Xu, M. Rang, I. M. Craig, and M. B. Raschke, "Pushing the sample-size limit of infrared vibrational nanospectroscopy: from monolayer toward single molecule sensitivity," J. Phys. Chem. Lett. **3**, 1836–1841 (2012).
4. M. Celebrano, P. Kukura, A. Renn, and V. Sandoghdar, "Single-molecule imaging by optical absorption," Nat. Photonics **5**, 95–98 (2011).
5. P. G. Etchegoin and E. C. Le Ru, "A perspective on single molecule SERS: current status and future challenges," Phys. Chem. Chem. Phys. **10**, 6079–6089 (2008).
6. K. Kneipp, Y. Wang, H. Kneipp, L. T. Perelman, I. Itzkan, R. Dasari, and M. S. Feld, "Single molecule detection using surface-enhanced Raman scattering (SERS)," Phys. Rev. Lett. **78**, 1667–1670 (1997).
7. P. Zijlstra, P. M. R. Paulo, and M. Orrit, "Optical detection of single non-absorbing molecules using the surface plasmon resonance of a gold nanorod," Nat. Nanotechnol. **7**, 379–382 (2012).
8. A. M. Armani, "Label-free, single-molecule detection with optical microcavities (August, pg 783, 2007)," Science **334**, 1496 (2011).
9. A. M. Armani, R. P. Kulkarni, S. E. Fraser, R. C. Flagan, and K. J. Vahala, "Label-free, single-molecule detection with optical microcavities," Science **317**, 783–787 (2007).
10. I. Teraoka, S. Arnold, and F. Vollmer, "Perturbation approach to resonance shifts of whispering-gallery modes in a dielectric microsphere as a probe of a surrounding medium," J. Opt. Soc. Am. B **20**, 1937–1946 (2003).
11. F. Vollmer and S. Arnold, "Whispering-gallery-mode biosensing: label-free detection down to single molecules," Nat. Methods **5**, 591–596 (2008).
12. M. Pelton, M. Z. Liu, H. Y. Kim, G. Smith, P. Guyot-Sionnest, and N. E. Scherer, "Optical trapping and alignment of single gold nanorods by using plasmon resonances," Opt. Lett. **31**, 2075–2077 (2006).
13. J. Zhu, S. K. Ozdemir, L. He, D. R. Chen, and L. Yang, "Single virus and nanoparticle size spectrometry by whispering-gallery-mode microcavities," Opt. Express **19**, 16195–16206 (2011).
14. J. G. Zhu, S. K. Ozdemir, Y. F. Xiao, L. Li, L. N. He, D. R. Chen, and L. Yang, "On-chip single nanoparticle detection and sizing by mode

splitting in an ultrahigh-Q microresonator," Nat. Photonics **4**, 46–49 (2010).
15. J. D. Swaim, J. Knittel, and W. P. Bowen, "Detection of nanoparticles with a frequency locked whispering gallery mode microresonator," Appl. Phys. Lett. **102**, 183106 (2013).
16. L. Stern, I. Goykhman, B. Desiatov, and U. Levy, "Frequency locked micro disk resonator for real time and precise monitoring of refractive index," Opt. Lett. **37**, 1313–1315 (2012).
17. T. Lu, H. Lee, T. Chen, S. Herchak, J. H. Kim, S. E. Fraser, R. C. Flagan, and K. Vahala, "High sensitivity nanoparticle detection using optical microcavities," Proc. Natl. Acad. Sci. USA **108**, 5976–5979 (2011).
18. V. R. Dantham, S. Holler, V. Kolchenko, Z. Wan, and S. Arnold, "Taking whispering gallery-mode single virus detection and sizing to the limit," Appl. Phys. Lett. **101**, 043704 (2012).
19. S. Arnold, M. Khoshsima, I. Teraoka, S. Holler, and F. Vollmer, "Shift of whispering-gallery modes in microspheres by protein adsorption," Opt. Lett. **28**, 272–274 (2003).
20. M. L. Gorodetsky, A. A. Savchenkov, and V. S. Ilchenko, "Ultimate *Q* of optical microsphere resonators," Opt. Lett. **21**, 453–455 (1996).
21. G. Farca, S. I. Shopova, and A. T. Rosenberger, "Cavity-enhanced laser absorption spectroscopy using microresonator whispering-gallery modes," Opt. Express **15**, 17443–17448 (2007).
22. A. C. R. Pipino, J. P. M. Hoefnagels, and N. Watanabe, "Absolute surface coverage measurement using a vibrational overtone," J. Chem. Phys. **120**, 2879–2888 (2004).
23. M. Mazurenka, A. J. Orr-Ewing, R. Peverall, and G. A. D. Ritchie, "Cavity ring-down and cavity enhanced spectroscopy using diode lasers," Ann. Rep. Prog. Chem. C **101**, 100–142 (2005).
24. A. C. R. Pipino, "Ultrasensitive surface spectroscopy with a miniature optical resonator," Phys. Rev. Lett. **83**, 3093–3096 (1999).
25. V. S. Ilchenko, X. S. Yao, and L. Maleki, "Pigtailing the high-*Q* microsphere cavity: a simple fiber coupler for optical whispering-gallery modes," Opt. Lett. **24**, 723–725 (1999).
26. D. K. Armani, T. J. Kippenberg, S. M. Spillane, and K. J. Vahala, "Ultra-high-*Q* toroid microcavity on a chip," Nature **421**, 925–928 (2003).
27. J. M. Herbelin, J. A. McKay, M. A. Kwok, R. H. Ueunten, D. S. Urevig, D. J. Spencer, and D. J. Benard, "Sensitive measurement of photon lifetime and true reflectances in an optical cavity by a phase-shift method," Appl. Opt. **19**, 144–147 (1980).
28. R. Engeln, G. von Helden, G. Berden, and G. Meijer, "Phase shift cavity ring down absorption spectroscopy," Chem. Phys. Lett. **262**, 105–109 (1996).
29. Z. G. Tong, A. Wright, T. McCormick, R. K. Li, R. D. Oleschuk, and H. P. Loock, "Phase-shift fiber-loop ring-down spectroscopy," Anal. Chem. **76**, 6594–6599 (2004).
30. J. A. Barnes, B. Carver, J. M. Fraser, G. Gagliardi, H. P. Loock, Z. Tian, M. Wilson, S. S. H. Yam, and O. Yastrubshak, "Loss determination in microsphere resonators by phase-shift cavity ring-down measurements," Opt. Express **16**, 13158–13167 (2008).
31. M. I. Cheema, S. Mehrabani, A. A. Hayat, Y. A. Peter, A. M. Armani, and A. G. Kirk, "Simultaneous measurement of quality factor and wavelength shift by phase shift microcavity ring down spectroscopy," Opt. Express **20**, 9090–9098 (2012).
32. M. Xu, D. F. Liu, and H. C. Allen, "Ethylenediamine at air/liquid and air/silica interfaces: protonation versus hydrogen bonding investigated by sum frequency generation spectroscopy," Environ. Sci. Technol. **40**, 1566–1572 (2006).
33. M. L. Gorodetsky, A. D. Pryamikov, and V. S. Ilchenko, "Rayleigh scattering in high-*Q* microspheres," J. Opt. Soc. Am. B **17**, 1051–1057 (2000).
34. T. J. Kippenberg, S. M. Spillane, and K. J. Vahala, "Modal coupling in traveling-wave resonators," Opt. Lett. **27**, 1669–1671 (2002).
35. J. A. Barnes, G. Gagliardi, and H. P. Loock, "Phase-shift cavity ring-down spectroscopy on a microresonator by Rayleigh backscattering," Phys. Rev. A **87**, 053843 (2013).
36. J. A. Barnes, G. Gagliardi, and H. P. Loock, "Erratum: Phase-shift cavity ring-down spectroscopy on a microsphere resonator by Rayleigh backscattering [Phys. Rev. A 87, 053843 (2013)]," Phys. Rev. A **88**, 059905 (2013).
37. E. D. Black, "An introduction to Pound-Drever-Hall laser frequency stabilization," Am. J. Phys. **69**, 79–87 (2001).
38. S. Avino, J. A. Barnes, G. Gagliardi, X. J. Gu, D. Gutstein, J. R. Mester, C. Nicholaou, and H. P. Loock, "Musical instrument pickup based on a laser locked to an optical fiber resonator," Opt. Express **19**, 25057–25065 (2011).
39. G. Gagliardi, M. Salza, S. Avino, P. Ferraro, and P. De Natale, "Probing the ultimate limit of fiber-optic strain sensing," Science **330**, 1081–1084 (2010).
40. V. Tsionsky and E. Gileadi, "Use of the quartz crystal microbalance for the study of adsorption from the gas phase," Langmuir **10**, 2830–2835 (1994).
41. I. Teraoka and S. Arnold, "Theory of resonance shifts in TE and TM whispering gallery modes by nonradial perturbations for sensing applications," J. Opt. Soc. Am. B **23**, 1381–1389 (2006).
42. I. Teraoka and S. Arnold, "Estimation of surface density of molecules adsorbed on a whispering gallery mode resonator: utility of isotropic polarizability," J. Appl. Phys. **102**, 076109 (2007).
43. L. V. Lanshina, M. N. Rodnikova, and K. T. Dudnikova, "Structure of liquid ethylene diamine according to data on molecular-scattering of light," J. Struct. Chem. **30**, 684–687 (1990).
44. M. T. S. R. Gomes, M. I. S. Verissimo, and J. A. B. P. Oliveira, "Detection of volatile amines using a quartz crystal with gold electrodes," Sens. Actuators B **57**, 261–267 (1999).
45. V. Dong, S. V. Pappu, and Z. Xu, "Detection of local density distributions of isolated silanol groups on planar silica surfaces using nonlinear optical molecular probes," Anal. Chem. **70**, 4730–4735 (1998).
46. J. D. Lambert and E. D. T. Strong, "The dimerization of ammonia and amines," Proc. R. Soc. A **200**, 566–572 (1950).
47. J. Rezac, "Properties and applications of whispering-gallery mode resonances in fused silica microspheres," Ph.D. thesis (Oklahoma State University, 2002).
48. C. Schmidt, A. Chipouline, T. Pertsch, A. Tunnermann, O. Egorov, F. Lederer, and L. Deych, "Nonlinear thermal effects in optical microspheres at different wavelength sweeping speeds," Opt. Express **16**, 6285–6301 (2008).
49. J. A. Barnes, H. P. Loock, and G. Gagliardi, "Phase shift cavity ring-down measurements on silica sphere microresponators," in *Cavity Enhanced Spectroscopy and Sensing*, H. P. Loock and G. Gagliardi, eds. (Springer, 2013).
50. G. Adamovsky, S. F. Lyuksyutov, J. R. Mackey, B. M. Floyd, U. Abeywickrema, I. Fedin, and M. Rackaitis, "Peculiarities of thermo-optic coefficient under different temperature regimes in optical fibers containing fiber Bragg gratings," Opt. Commun. **285**, 766–773 (2012).
51. M. Buback and H. P. Vogele, *FT-NIR Atlas* (VCH, 1993).
52. C. F. Bohren and D. R. Huffman, *Absorption and Scattering of Light by Small Particles* (Wiley-VCH, 1998).
53. B. Fubini, V. Bolis, A. Cavenago, E. Garrone, and P. Ugliengo, "Structural and induced heterogeneity at the surface of some SiO_2 polymorphs from the enthalpy of adsorption of various molecules," Langmuir **9**, 2712–2720 (1993).
54. C. C. Lam, P. T. Leung, and K. Young, "Explicit asymptotic formulas for the positions, widths, and strengths of resonances in Mie scattering," J. Opt. Soc. Am. B **9**, 1585–1592 (1992).

optica

Photon pairs with coherence time exceeding 1 μs

LUWEI ZHAO, XIANXIN GUO, CHANG LIU, YUAN SUN, M. M. T. LOY, AND SHENGWANG DU*

Department of Physics, The Hong Kong University of Science and Technology, Clear Water Bay, Kowloon, Hong Kong, China
**Corresponding author: dusw@ust.hk*

Received 7 April 2014; revised 4 June 2014; accepted 5 June 2014 (Doc. ID 209700); published 6 August 2014

The generation of nonclassical photon pairs with a long coherence time is key for applications that range from fundamental to quantum communication and metrology. Spontaneous four-wave mixing with electromagnetically induced transparency has been demonstrated as one of the most efficient methods; however, narrowing the bandwidth and producing photon pairs with a temporal length beyond 1 μs remains a technical challenge due to noise considerations and the need for cold atoms with a high optical depth (OD). In this work, we demonstrate the generation of narrowband photon pairs with a controllable coherence time up to 1.72 μs in a laser-cooled atomic ensemble with an OD as high as 130. At such a high OD, we find that the pump laser field spatial profile has a significant effect on the time–frequency entangled two-photon waveform. We also confirm the quantum particle nature of heralded narrowband single photons generated from this source.

OCIS codes: (270.0270) Quantum optics; (190.4380) Nonlinear optics, four-wave mixing.

http://dx.doi.org/10.1364/OPTICA.1.000084

Nonclassical photon pairs are standard tools to probe and exploit the quantum realm beyond the classical limits. For a quantum network whose atomic matter nodes are linked by flying single photons, its quantum connectivity and scalability strongly depend on the interaction between atoms and photons [1,2]. An efficient photon–atom quantum interface requires that the photons have a bandwidth sufficiently narrower than the natural linewidth of related atomic transitions. Among many efforts to produce narrowband photon pairs [3–9], spontaneous four-wave mixing (SFWM) using electromagnetically induced transparency (EIT) [10] in cold atoms has been demonstrated as one of the most efficient methods [11,12]. Using laser-cooled atoms with an optical depth (OD) of 53 and working at the EIT group delay regime, Du *et al.* at Stanford University generated time–frequency entangled photon pairs with a temporal length of about 0.9 μs, corresponding to a bandwidth of about 0.75 MHz [13]. These narrowband biphotons are ideal for producing heralded single photons with arbitrary waveforms using electro-optical modulation [14]. Their capability to interact with atoms resonantly has been applied to observing single-photon optical precursors [15], efficiently storing a single photon in an atomic quantum memory [16], and coherently controlling single-photon absorption and re-emission [17]. Besides the fundamental interest of the time–space nonlocality of their extended wave packets [18], narrowband single photons with a long coherence time also have applications in quantum metrology [19] and quantum state teleportation [20] based on single-photon or multiphoton interference. The recently demonstrated highly efficient EIT optical memory [21] for quantum state operation requires single photons with microsecond coherence time. However, further narrowing the biphoton bandwidth and having a temporal length longer than 1 μs remains a technical challenge, because a longer single-photon time window significantly increases the probability of receiving accidental noise counts and thus reduces its immunity to a noisy environment. Meanwhile, producing photon pairs with a longer temporal length requires cold atoms with a much higher OD.

In this Letter, we report the generation of narrowband photon pairs with a coherence time up to 1.72 μs, using ^{85}Rb cold atoms in our recently developed dark-line two-dimensional (2D) magneto-optical trap (MOT) [22] with an OD as high as 130. We find that at such a high OD the pump laser spatial profile has a significant effect on the biphoton waveform. The estimated bandwidth of about 0.43 MHz is the narrowest biphoton bandwidth reported to date to the best of our knowledge. We also demonstrate that this source can be used to produce narrowband heralded single photons with high purity.

The experiment setup and relevant ^{85}Rb atomic energy level diagram are illustrated in Fig. 1. The 2D MOT has a

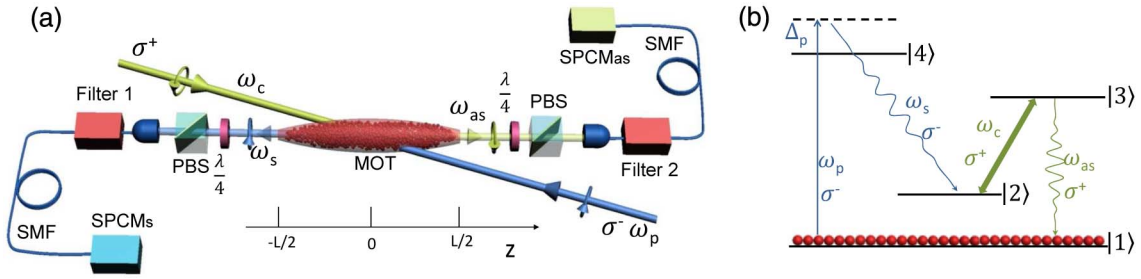

Fig. 1. (a) Schematic of the experiment setup for producing narrowband photon pairs and (b) the relevant ^{85}Rb atomic energy level diagram for spontaneous four-wave mixing. The ^{85}Rb energy levels are chosen as $|1\rangle = |5S_{1/2}, F = 2\rangle$, $|2\rangle = |5S_{1/2}, F = 3\rangle$, $|3\rangle = |5P_{1/2}, F = 3\rangle$, and $|4\rangle = |5P_{3/2}, F = 3\rangle$.

longitudinal length $L = 1.5$ cm and a temperature of 100 μK. The experiment is run periodically with 4.5 ms MOT time followed by 0.5 ms biphoton generation time in each cycle. At end of the MOT time, the trapping and repumping lasers (not shown in Fig. 1) are switched off and all the atoms are optically pumped to the ground level $|1\rangle$. During the biphoton generation time, phase-matched Stokes (ω_s) and anti-Stokes (ω_{as}) paired photons are produced in opposing directions along the MOT longitudinal z axis in the presence of the counter-propagating coupling (ω_c) and pumping (ω_p) laser beams, which are aligned at an angle of 2.8° with respect to the longitudinal z axis. The pump laser (780 nm), σ^- circularly polarized, is blue detuned by 60 MHz from the transition $|1\rangle \rightarrow |4\rangle$. The coupling laser (795 nm), σ^+ circularly polarized, is on resonance to the transition $|2\rangle \rightarrow |3\rangle$. Both pump and couping beams are collimated with the same $1/e^2$ diameter of 1.40 mm. The spontaneously generated Stokes and anti-Stokes photons have σ^- and σ^+ polarizations, respectively. After passing through the polarization filters [composed of a $\lambda/4$ waveplate and polarization beam splitter (PBS)], the paired photons are coupled into two opposing single-mode fibers (SMFs), followed by Fabry–Perot etalon filters (500 MHz bandwidth), and detected by two single-photon counting modules (SPCM$_s$ and SPCM$_{as}$, Excelitas/PerkinElmer SPCM-AQRH-16-FC). The fiber–fiber coupling efficiency, etalon filter transmission, and SPCM detection efficiency are 70%, 65%, and 50%, respectively. The coincidence counts are recorded by a time-to-digit converter (Fast Comtec P7888) with a bin width of 2 ns. The MOT magnetic field remains on all the time.

The dark-line 2D MOT configuration allows us to obtain cold atoms with OD > 100 on the anti-Stokes transition. At such a high OD, we find that the pump laser intensity distribution along the longitudinal z axis of the photon pair generation has a significant effect on the two-photon waveform. Because of the 2.8° angle between the pump beam propagation direction and the photon pair longitudinal z axis, the pump beam transverse Gaussian profile is projected to the z axis. Following the perturbation treatment [23], and taking into account the pump field profile, we have the Stokes–anti-Stokes two-photon state

$$|\Psi\rangle = \int d\omega \kappa(\omega) F(\Delta k) \hat{a}_{as}^{\dagger}(\omega_{as0} + \omega) \hat{a}_{s}^{\dagger}(\omega_{s0} - \omega)|00\rangle, \quad \textbf{(1)}$$

where $\kappa(\omega)$ is the nonlinear parametric coupling coefficient and $F(\Delta k)$ is the Fourier transform of the pump field profile $f(z) = 1/(2\pi) \int dk F(k) e^{ikz}$ along the z axis. ω_{s0} and ω_{as0} are the central frequencies of Stokes and anti-Stokes photons, respectively. $\Delta k(\omega) = (\vec{k}_{as} + \vec{k}_s - \vec{k}_c - \vec{k}_p) \cdot \hat{z}$ is the complex phase mismatching of the four waves inside the atomic medium. $|00\rangle$ represents the vacuum state in the Stokes and anti-Stokes modes. As seen from Eq. (1), the frequencies of the Stokes and anti-Stokes photons are entangled due to the energy conservation. The corresponding two-photon wave packet can be described as $e^{-i\omega_{s0}t_s} e^{-i\omega_{as0}t_{as}} \psi(\tau)$, with $\tau = t_{as} - t_s$. The relative wave amplitude is

$$\psi(\tau) = \frac{1}{2\pi} \int d\omega \kappa(\omega) F(\Delta k) e^{i(k_{as}+k_s)L/2} e^{-i\omega\tau}, \quad \textbf{(2)}$$

which displays the entanglement in the time domain. We work in the group delay regime, where the anti-Stokes photons travel with a slow group velocity V_g and the Stokes photons travel nearly at the speed of light in vacuum. In this regime, the spatial phase propagation in Eq. (2) can approximated as

$$(k_{as} + k_s)L/2 \simeq \phi_0 + \omega\tau_g/2, \quad \textbf{(3)}$$

where ϕ_0 is a constant phase factor. The EIT group delay, $\tau_g = L/V_g = (2\gamma_{13}/|\Omega_c|^2)\text{OD}$, can be controlled by changing the coupling Rabi frequency Ω_c and OD [23], where $\gamma_{13} = 2\pi \times 3$ MHz is the electric dipole relaxation rate between $|1\rangle$ and $|3\rangle$. The two-photon spectrum is mainly determined by the phase-matching longitudinal function $F[\Delta k(\omega)]$. The full width at half-maximum (FWHM) bandwidth of the photons can be estimated as $\Delta\omega = 2\pi \times 0.88/\tau_g$. Under these conditions, $\kappa(\omega) \simeq \kappa_0$ varies slowly in frequency, and we can reduce Eq. (2) to

$$\psi(\tau) \simeq \kappa_0 V_g f(L/2 - V_g\tau) e^{i\phi_0}. \quad \textbf{(4)}$$

It is clear that the pump field spatial variation is mapped onto the two-photon quantum temporal waveform, with its origin delayed by $L/(2V_g) = \tau_g/2$. The two-photon temporal correlation time is determined by the group delay τ_g of the slow anti-Stokes photon.

The Glauber correlation function can be obtained as $G^{(2)}(\tau) = |\psi(\tau)|^2$. With a joint detection efficiency (including all loss and detection quantum efficiency) η, time bin width Δt_{bin}, collection time T, and duty cycle ζ, the two-photon coincidence counts can be calculated from $\eta\zeta G^{(2)}(\tau)\Delta t_{\text{bin}} T$.

Figure 2 shows our experimental results at OD = 130 and the coupling Rabi frequency $\Omega_c = 2\pi \times 11.34$ MHz, which is determined from the measured coupling laser power and beam size. The EIT spectrum in Fig. 2(a) shows that the on-resonance transmission exceeds 0.8. The finite EIT loss is caused by the ground-state dephasing rate between $|1\rangle$ and $|2\rangle$, which is $\gamma_{12} = 2\pi \times 30$ kHz in our setup. The two-photon coincidence counts collected over $T = 2000$ s are shown in Fig. 2(b). The solid theoretical curve calculated from Eq. (2) agrees well with the experimental data. There are two features of the two-photon correlation function. The fast oscillating spike at the leading edge is the biphoton optical precursor, which travels at the speed of light in vacuum [15,24]. The following slowly varying long waveform is generated from the narrow EIT window and has a $1/e$ correlation time of 854 ns. The Gaussian shape reveals the pump laser intensity profile, as we expected from Eq. (4). As we reduce the OD below 60, the Gaussian shape is not apparent; this may be the reason why this effect has not been observed experimentally or discussed theoretically before.

To characterize the nonclassical property of the photon pair source, we confirm its violation of the Cauchy–Schwartz inequality [25]. Normalizing the coincidence counts to the accidental background floor in Fig. 2(b), we get the normalized cross-correlation function $g^{(2)}_{s,as}(\tau)$, which has a peak value of 60. With the autocorrelations $g^{(2)}_{s,s}(0) = g^{(2)}_{as,as}(0) = 2$, we obtain the violation of the Cauchy–Schwartz inequality $[g^{(2)}_{s,as}(\tau)]^2/[g^{(2)}_{s,s}(0)g^{(2)}_{as,as}(0)] \leq 1$ by a factor of 900.

Another measure of the quantum nature of the photon pairs is the conditional autocorrelation function of the heralded single anti-Stokes photons trigged by detection of their paired Stokes photons. We pass the anti-Stokes photons through a fiber-coupled beam splitter whose outputs are connected to two SPCMs (SPCM_1 and SPCM_2). The conditional autocorrelation is obtained from $g^{(2)}_c = (N_s N_{s12}/N_{s1}N_{s2})$, where N_s is the Stokes counts, N_{s1} and N_{s2} are the twofold coincidence counts, and N_{s12} is the threefold coincidence counts [26]. The measured conditional autocorrelation function $g^{(2)}_c$ of the heralded anti-Stokes photons as a function of coincidence window width is displayed in Fig. 2(c). The coherent state, two-photon Fock state, and single-photon state give $g^{(2)}_c = 1$, 0.5, and 0, respectively. Our measured $g^{(2)}_c$ is far below the threshold value of 0.5.

We then reduce the coupling laser power to narrow the EIT window. Figure 3 shows the result at $\Omega_c = 2\pi \times 7.77$ MHz. From the EIT spectrum in Fig. 3(a), the on-resonance transmission drops down to 0.3. In Fig. 3(b), the two-photon waveform has a longer temporal duration of 1720 ns. The normalized cross-correlation function has a maximum value of 47,

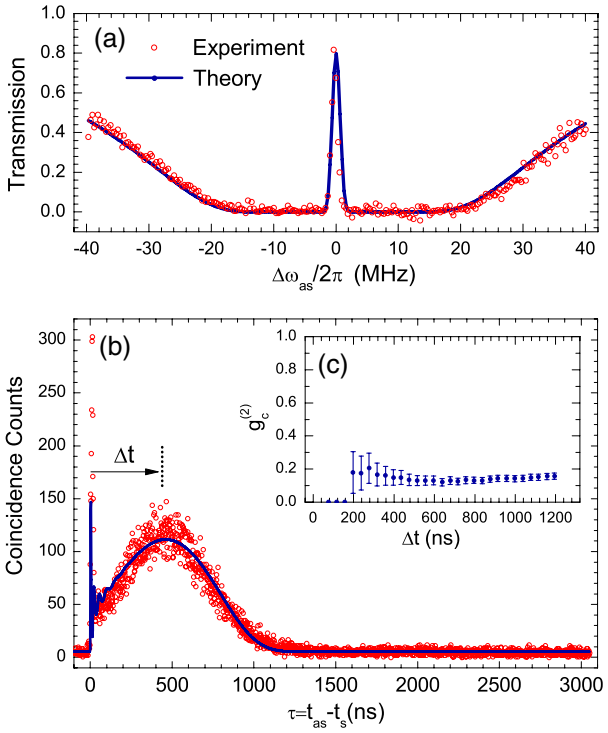

Fig. 2. (a) Anti-Stokes EIT transmission spectrum, (b) two-photon coincidence counts with 2 ns bin width collected over 2000 s as a function of relative time delay. Operating parameters are OD = 130, $\Omega_c = 2\pi \times 11.34$ MHz, and $\Omega_p = 2\pi \times 0.60$ MHz. (c) The measured conditional autocorrelation $g^{(2)}_c$ of heralded anti-Stokes photons as a function of coincidence window width Δt.

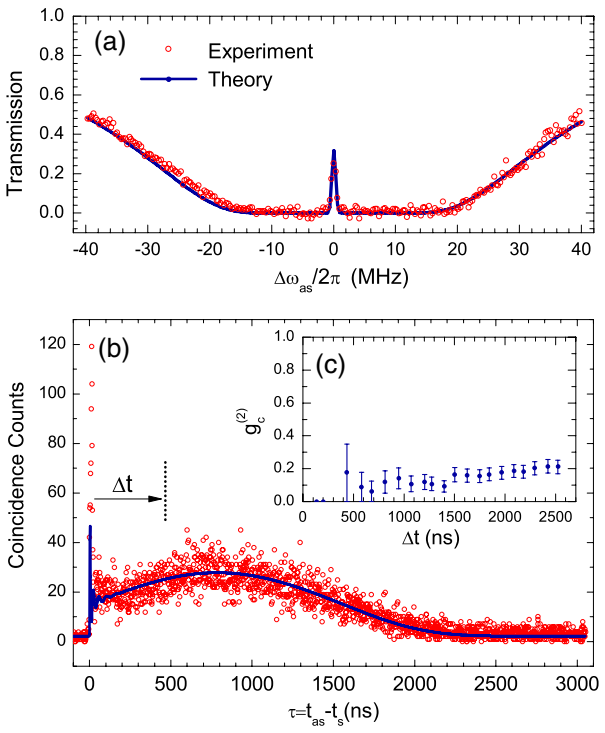

Fig. 3. (a) Anti-Stokes EIT transmission spectrum, (b) two-photon coincidence counts with 2 ns bin width collected over 2000 s as a function of relative time delay. Operating parameters are OD = 130, $\Omega_c = 2\pi \times 7.77$ MHz, and $\Omega_p = 2\pi \times 0.60$ MHz. (c) The measured conditional autocorrelation $g^{(2)}_c$ of heralded anti-Stokes photons as a function of coincidence window width Δt.

which violates the Cauchy–Schwartz inequality by a factor of 552. The conditional autocorrelation $g_c^{(2)}$ as a function of coincidence time window width is shown in Fig. 3(c), which confirms the quantum nature of the heralded single anti-Stokes photons.

In both cases, the pump laser has a power of 1.25 μW. Taking into account the SMF fiber–fiber coupling efficiency, filter transmission, SPCM detecting efficiency, and duty cycle, we estimate biphoton generation rates from cold atoms to be 3200 pairs/s and 2000 pairs/s for the conditions of Fig. 2 and Fig. 3, respectively. Higher photon pair generation rates can be achieved by increasing the pump laser power, but the uncorrelated accidental counts increase quadratically. Because our theory agrees well with experiment in the entire parameter space (see Figs. 2 and 3 for examples), we calculate the FWHM bandwidth of the generated photons from the power spectrum $|\kappa(\omega)F[\Delta k]e^{i(k_{as}+k_s)L/2}|^2$. we obtain bandwidths of 0.92 and 0.43 MHz for the cases in Fig. 2 and Fig. 3, respectively.

We further reduce the coupling laser power and find no significant increase in the temporal correlation time, while the EIT transmission and biphoton counts drop. As the EIT loss is significant, the coherence time approaches τ_g/β, where $\beta > 1$ is the absorption depth (the EIT transmission is characterized as $e^{-\beta}$) [23]. The ultimate correlation time is limited by the ground-state coherence time, i.e., $1/(2\gamma_{12}) \approx 2.65$ μs, which is consistent with our experimental observation.

To verify the control effect of the pump field profile on the biphoton waveform, we shift the pump-coupling beams toward the anti-Stokes photon side so that the pump laser intensity profile on the atomic medium is not symmetric along the z axis. The measured two-photon correlations at different coupling powers are displayed in Figs. 4(a) and 4(b). Consistent with our prediction from Eq. (4), the peak of the Gaussian profile on the main waveform moves toward the side of the shorter time delay. The solid theoretical curves agree well with the experimental data.

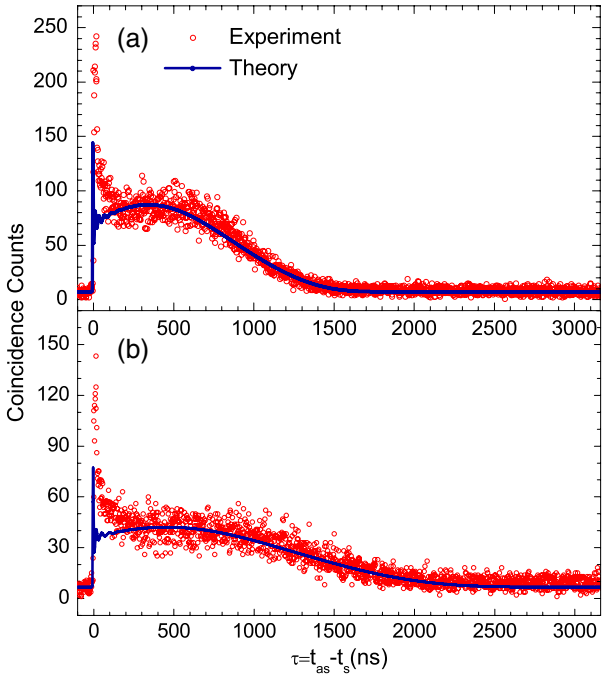

Fig. 4. Biphoton waveforms with a nonsymmetric intensity distribution of the pump laser beam across the atomic medium. The operating parameters in (a) and (b) are similar to those in Fig. 2 and Fig. 3, respectively.

In summary, we produced photon pairs with a controllable temporal length up to 1.72 μs, which corresponds to a bandwidth of 0.43 MHz. This is achieved by making use of EIT-assisted SFWM in cold atoms at a high OD of 130. We also demonstrated the efficient generation of narrowband heralded single photons with an autocorrelation value below 0.2 in a 2 μs coincidence window. We found that at such a high OD the pump laser field profile has a significant effect on the biphoton waveform. This technique can be used to engineer the biphoton waveform by manipulating the spatial profile of the pump beam. Our narrowband photon pairs with such a long coherence time can have immediate improvement for single-photon based differential-phase-shift quantum key distribution [27].

FUNDING INFORMATION

Hong Kong Research Grants Council (601411).

ACKNOWLEDGMENTS

The authors thank Peng Chen and Chi Shu for technical support.

REFERENCES

1. H. J. Kimble, Nature **453**, 1023 (2008).
2. L. M. Duan, M. D. Lukin, J. I. Cirac, and P. Zoller, Nature **414**, 413 (2001).
3. Z. Y. Ou and Y. J. Lu, Phys. Rev. Lett. **83**, 2556 (1999).
4. H. Wang, T. Horikiri, and T. Kobayashi, Phys. Rev. A **70**, 043804 (2004).
5. X. H. Bao, Y. Qian, J. Yang, H. Zhang, Z.-B. Chen, T. Yang, and J.-W. Pan, Phys. Rev. Lett. **101**, 190501 (2008).
6. B. Srivathsan, G. K. Gulati, B. Chng, G. Maslennikov, D. Matsukevich, and C. Kurtsiefer, Phys. Rev. Lett. **111**, 123602 (2013).
7. M. Scholz, L. Koch, and O. Benson, Phys. Rev. Lett. **102**, 063603 (2009).
8. M. Fortsch, J. U. Furst, C. Wittmann, D. Strekalov, A. Aiello, M. V. Chekhova, C. Silberhorn, G. Leuchs, and C. Marquardt, Nat. Commun. **4**, 1818 (2013).
9. J. Fekete, D. Rielander, M. Cristiani, and H. de Riedmatten, Phys. Rev. Lett. **110**, 220502 (2013).
10. S. Harris, Phys. Today **50**(7), 36 (1997).
11. V. Balic, D. A. Braje, P. Kolchin, G. Y. Yin, and S. E. Harris, Phys. Rev. Lett. **94**, 183601 (2005).
12. J. K. Thompson, J. Simon, H. Loh, and V. Vuletic, Science **313**, 74 (2006).
13. S. Du, P. Kolchin, C. Belthangady, G. Yin, and S. Harris, Phys. Rev. Lett. **100**, 183603 (2008).
14. P. Kolchin, C. Belthangady, S. Du, G. Y. Yin, and S. E. Harris, Phys. Rev. Lett. **101**, 103601 (2008).
15. S. Zhang, J. F. Chen, C. Liu, M. M. T. Loy, G. K. L. Wong, and S. Du, Phys. Rev. Lett. **106**, 243602 (2011).
16. S. Zhou, S. Zhang, C. Liu, J. F. Chen, J. Wen, M. M. T. Loy, G. K. L. Wong, and S. Du, Opt. Express **20**, 24124 (2012).
17. S. Zhang, C. Liu, S. Zhou, C.-S. Chuu, M. M. T. Loy, and S. Du, Phys. Rev. Lett. **109**, 263601 (2012).

18. S. M. Tan, D. F. Walls, and M. J. Collett, Phys. Rev. Lett. **66**, 252 (1991).
19. F. Wolfgramm, C. Vitelli, F. A. Beduini, N. Godbout, and M. W. Mitchell, Nat. Photonics **7**, 28 (2013).
20. W. B. Gao, P. Fallahi, E. Togan, A. Delteil, Y. S. Chin, J. Miguel-Sanchez, and A. Imamoglu, Nat. Commun. **4**, 2744 (2013).
21. Y.-H. Chen, M.-J. Lee, I.-C. Wang, S. Du, Y.-F. Chen, Y.-C. Chen, and I. A. Yu, Phys. Rev. Lett. **110**, 083601 (2013).
22. S. Zhang, J. F. Chen, C. Liu, S. Zhou, M. M. T. Loy, G. Wong, and S. Du, Rev. Sci. Instrum. **83**, 073102 (2012).
23. S. Du, J. Wen, and M. H. Rubin, J. Opt. Soc. Am. B **25**, C98 (2008).
24. S. Du, C. Belthangady, P. Kolchin, G. Y. Yin, and S. E. Harris, Opt. Lett. **33**, 2149 (2008).
25. J. F. Clauser, Phys. Rev. D **9**, 853 (1974).
26. P. Grangier, G. Roger, and A. Aspect, Europhys. Lett. **1**, 173 (1986).
27. C. Liu, S. Zhang, L. Zhao, P. Chen, C.-H. F. Fung, H. F. Chau, M. M. T. Loy, and S. Du, Opt. Express **21**, 9505 (2013).

Research Article Vol. 1, No. 2 / August 2014 / Optica 89

SUSY-inspired one-dimensional transformation optics

MOHAMMAD-ALI MIRI,[1,*] MATTHIAS HEINRICH,[1,2] AND DEMETRIOS N. CHRISTODOULIDES[1]

[1]CREOL, College of Optics and Photonics, University of Central Florida, Orlando, Florida 32816–2700, USA

[2]Institute of Applied Physics, Abbe Center of Photonics, Friedrich-Schiller-Universität Jena, Max-Wien-Platz 1, 07743 Jena, Germany

*Corresponding author: miri@knights.ucf.edu

Received 9 April 2014; revised 27 June 2014; accepted 29 June 2014 (Doc. ID 209850); published 6 August 2014

Transformation optics aims to identify artificial materials and structures with desired electromagnetic properties by means of pertinent coordinate transformations. In general, such schemes are meant to appropriately tailor the constitutive parameters of metamaterials in order to control the trajectory of light in two and three dimensions. Here, we introduce a new class of one-dimensional optical transformations that exploits the mathematical framework of supersymmetry (SUSY). This systematic approach can be utilized to synthesize photonic configurations with identical reflection and transmission characteristics, down to the phase, for all incident angles, thus rendering them perfectly indistinguishable to an external observer. Along these lines, low-contrast dielectric arrangements can be designed to fully mimic the behavior of a given high-contrast structure that would have been otherwise beyond the reach of available materials and existing fabrication techniques. Similar strategies can also be adopted to replace negative-permittivity domains, thus averting unwanted optical losses.

OCIS codes: (290.0290) Scattering; (290.5839) Scattering, invisibility; (260.2710) Inhomogeneous optical media.

http://dx.doi.org/10.1364/OPTICA.1.000089

1. INTRODUCTION

The problem of reconstructing the shape of a potential distribution solely from information carried by its scattering pattern has a long-standing history in a number of diverse disciplines of science and technology [1–5]. Naturally, in such inverse problems, the question of uniqueness is of crucial importance: are the properties of an object fully determined by its corresponding far-field scattering data? In general, the answer is no. In quantum mechanical settings, for example, one can always identify an N-parameter family of different potentials that support the same discrete set of N bound-state eigenvalues and exhibit similar scattering characteristics [4]. Closely related to this subject is the idea of supersymmetry (SUSY) [6–10]. This mathematical framework emerged in quantum field theory as a means to treat fermions and bosons on equal footing [9]. Subsequently, notions of SUSY were utilized to obtain isospectral and phase-equivalent potentials within the context of nonrelativistic quantum mechanics [10].

On the other hand, recent developments in transformation optics and optical conformal mapping have brought about novel methodologies to address inverse problems [11–16]. By virtue of coordinate transformations, such schemes can in principle provide the spatial distribution of electric permittivities and magnetic permeabilities that would perform a desired task such as cloaking [17–22]. As one would expect, the material properties required to implement such configurations might not always be available in practice. Clearly of interest would be to develop alternative strategies that allow one to judiciously control the scattering properties of an object, while at the same time reducing the complexity of the structures involved.

As we will see, SUSY can provide a new avenue for 1D transformation optics that would have been otherwise impossible using other multidimensional approaches (see Fig. 1). Along these lines, we introduce appropriate optical transformations in 1D refractive index landscapes and explore their implications in terms of their far-field response. In addition

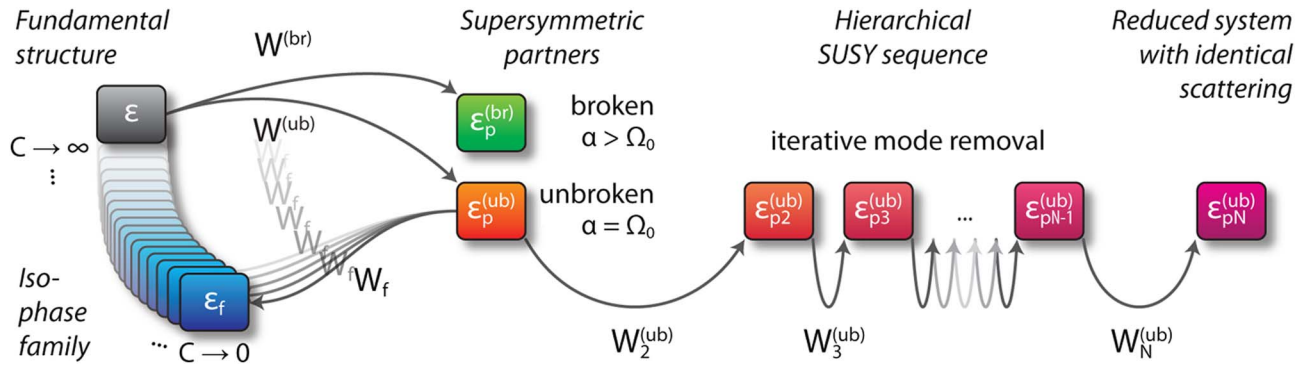

Fig. 1. Schematic overview of the different SUSY optical transformations. Starting from a given fundamental structure ϵ, supersymmetric partners ϵ_p can be constructed. Whereas the broken SUSY system $\epsilon_p^{(br)}$ preserves all bound modes, unbroken SUSY ($\epsilon_p^{(ub)}$) removes the fundamental mode. Regardless, in both cases, the intensity reflection and transmission coefficients of the superpartners are identical to those of the fundamental system. In order to maintain the full complex scattering characteristics, a family ϵ_f of isophase structures can be synthesized. Finally, a hierarchical sequence of higher-order superpartners $\epsilon_{p,2\ldots N}^{(ub)}$ may be utilized to obtain a scattering-equivalent structure, which requires a substantially lower refractive index contrast than that involved in the original system ϵ.

to finding superpartners with similar scattering behavior, systematic SUSY deformations allow us to design systems that exhibit identical complex reflection and transmission coefficients for all incident angles. As a result, two such dielectric objects, however dissimilar, become virtually indistinguishable. Remarkably, the proposed formalism can be employed to synthesize photonic configurations that behave in exactly the same way as high-refractive-index-contrast devices, by only utilizing low-contrast dielectric media. Similar methodologies can be employed to substitute negative-permittivity inclusions with purely dielectric media as a means to obtain the intended functionality without introducing any additional loss.

2. SUPERSYMMETRIC OPTICAL TRANSFORMATIONS

In 1D inhomogeneous settings, the propagation of TE-polarized waves is known to obey the Helmholtz equation [23], $[\partial_{xx} + \partial_{yy} + k_0^2\epsilon(x)]E_z(x,y) = 0$, where k_0 is the vacuum wavenumber and $\epsilon(x)$ is the relative permittivity of a given (fundamental) structure to be emulated via SUSY transformations (see Fig. 1). The analysis of TM waves can be carried out in a similar manner (see Supplement 1). In the TE case, the spatial dependence of the electric field E_z can be described via $E_z(x,y) = \psi(x)e^{i\beta y}$. Here, $\beta = k_0 n_0 \sin\theta$ represents the y component of the wave vector for an incidence angle θ, and $n_0 = \sqrt{\epsilon(X \to \pm\infty)}$ is the background refractive index. By employing the normalized quantities $X = k_0 x$, $Y = k_0 y$, and $\Omega = \beta^2/k_0^2$, the Helmholtz equation then reduces to a 1D Schrödinger-like equation:

$$H\psi(X) = \Omega\psi(X). \tag{1}$$

The resulting Hamiltonian $H = \partial_{XX} + \epsilon(X)$ can be factorized as $H = BA + \alpha$, where the operators A and B are defined as $A = \partial_X + W(X)$, $B = \partial_X - W(X)$, and α is an auxiliary constant of the problem. Here $B = -A^\dagger$, where "†" represents the Hermitian conjugate. The superpotential W can then be obtained as a solution of the Riccati equation [7],

$$\epsilon(X) = +W' - W^2 + \alpha, \tag{2}$$

in terms of the fundamental permittivity profile $\epsilon(X)$. Once W has been determined, one can establish a partner Hamiltonian $H_p = AB + \alpha$, which corresponds to a new distribution in the electric permittivity:

$$\epsilon_p(X) = -W' - W^2 + \alpha. \tag{3}$$

As a direct consequence of this construction, the modes ψ_p of the partner potential ϵ_p are related [24] to the ones of the fundamental through the expressions $\psi_p \propto (\partial_X + W)\psi$ and $\psi \propto (\partial_X - W)\psi_p$. These latter relations hold for guided waves as well as for radiation modes, and each such pair of states is characterized by a common eigenvalue. We note that two options for choosing α exist: (a) Assuming that the structure supports at least one bound state, one may opt to set α equal to the fundamental mode's eigenvalue, i.e., $\alpha = \Omega_0$. (b) The other possibility is to choose $\alpha > \Omega_0$, irrespective of whether the system supports bound states or not. The first case corresponds to an unbroken SUSY: the two potentials share the guided wave eigenvalue spectra except for that of the fundamental mode, which does not have a corresponding state in the partner. In the second case, however, SUSY is broken, and the two arrangements share an identical eigenvalue spectrum, including that of the fundamental mode. As an example, Fig. 2(a) depicts the relative permittivity distribution $\epsilon(X) = 1 + \exp[-(X/5)^8]$, corresponding to a step-index-like waveguide; its unbroken and broken SUSY partners are shown in Figs. 2(b) and 2(c), respectively. W can also be found analytically [7] via

$$W = -\partial_X \ln(\psi_0) \tag{4}$$

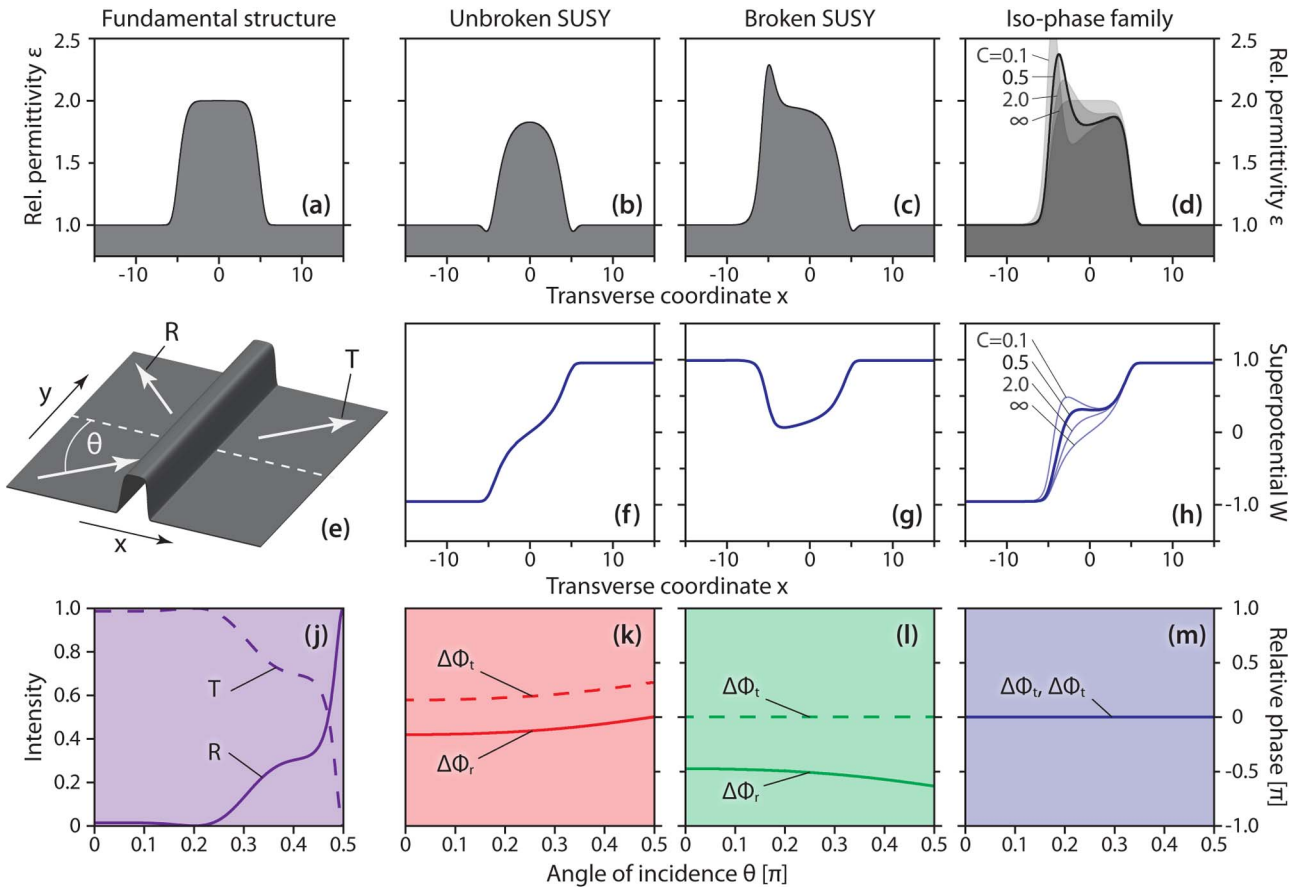

Fig. 2. Relative permittivity distributions of the original and the transformed potentials. (a) The fundamental system has a step-like profile $\epsilon(X) = 1 + \exp[-(X/5)^8]$. (b) Superpartner in the unbroken SUSY regime. (c) Superpartner in the broken SUSY case. (d) Phase-equivalent structures. (e) Scattering geometry. (f–h) Superpotentials W corresponding to panels (b–d). (j) Identical reflectivity R (solid line) and transmittivity T (dashed line) corresponding to Figs. 1(a)–1(d). (k–m) Relative phases of the reflection ($\Delta\Phi_r$, solid line) and transmission ($\Delta\Phi_t$, dashed) coefficients of the structures in (b–d) compared to the fundamental system (a) as a function of the incident angle θ. The scattering characteristics were evaluated by means of the differential transfer matrix method [23].

in the unbroken SUSY case, i.e., for $\alpha = \Omega_0$, when ϵ supports at least one bound state ψ_0. In either regime, Eq. (2) can always be solved numerically to obtain the superpotential W. An alternative approach is to start with an arbitrary superpotential and construct the two superpartner structures ϵ and ϵ_p according to Eqs. (2) and (3). In this scenario, it still remains to be determined whether SUSY is unbroken or broken. This question can be resolved by the so-called Witten index [6]. In general, if $W(X)$ approaches $W_\pm$ at $X \to \pm\infty$, unbroken SUSY requires $W_+ = -W_-$, while a broken SUSY demands that $W_+ = W_-$.

3. ISOPHASE FAMILIES OF OPTICAL POTENTIALS

It is important to note that more than one superpotential can exist for any given distribution $\epsilon(X)$. In fact, as we show here, one can systematically generate an entire parametric family W_f of viable superpotentials that satisfy Eq. (3). To show this, let us start from Eq. (3), which relates the superpartner ϵ_p to the superpotential W. Starting from a particular W, this solution can be generalized by adopting the form $W_f = W + 1/v$, in which case the unknown function v satisfies $(\partial_X - 2W)v = 1$. Direct integration readily leads to $v = e^{+2\int_{-\infty}^{X} W\mathrm{d}X'}\left(C + \int_{-\infty}^{X} e^{-2\int_{-\infty}^{X'} W\mathrm{d}X''}\mathrm{d}X'\right)$, where C is an arbitrary real-valued constant, giving rise to a parametric family W_f of superpotentials $W_f(X;C) = W + \partial_X \ln\left(C + \int_{-\infty}^{X} e^{-2\int_{-\infty}^{X'} W\mathrm{d}X''}\mathrm{d}X'\right)$. If the superpotential W has been specifically obtained from the bound state ψ_0 [from Eq. (4)], then this parametric family can be obtained via

$$W_f(X;C) = W + \partial_X \ln\left(C + \int_{-\infty}^{X} \psi_0^2(X')\mathrm{d}X'\right). \quad (5)$$

Whereas all members of this family lead to the same superpartner ϵ_p, each of them describes a different permittivity distribution ϵ according to Eq. (2). The resulting parametric family [10] of structures $\epsilon_f(X;C)$ is associated with the fundamental distribution ϵ and its ground state ψ_0 as follows:

Table 1. Reflection and Transmission Coefficients for the Different SUSY Transformations[a]

Coefficient	Unbroken SUSY	Broken SUSY	Isophase
Reflection	$r_p = r \cdot \exp\left[-2i \tan^{-1}\left(\frac{n_0 \cos\theta}{W_-}\right)\right]$	$r_p = r \cdot \exp\left[-2i \tan^{-1}\left(\frac{n_0 \cos\theta}{W_-}\right)\right]$	$r_f = r$
Transmission	$t_p = t \cdot \exp\left[-2i \tan^{-1}\left(\frac{n_0 \cos\theta}{W_-}\right)\right]$	$t_p = t$	$t_f = t$

[a] $W_- = W(-\infty)$ designates the asymptotic value of the superpotential on the left side of the structure, and r, t are the coefficients of the original structure.

$$\epsilon_f(X;C) = \epsilon(X) + 2\partial_{XX} \ln\left(C + \int_{-\infty}^{X} \psi_0^2(X')\mathrm{d}X'\right), \quad \textbf{(6)}$$

where C represents a free parameter. Note that here the transformation between the original structure and its superpartner was only used to prove Eq. (6), which itself is completely independent from the superpartner. According to this equation, simply by starting from a given potential and its ground state eigenfunction, a whole family of isospectral potentials can be established. Figure 2(d) depicts such family members for the fundamental structure ϵ shown in Fig. 2(a) when $C = 0.1$, 0.5, or 2.0, respectively. Note that the original permittivity distribution ϵ is in itself a member of this family, since $\epsilon_f \to \epsilon$ for $C \to +\infty$. All the modes ψ_f of any other member are related to its states ψ, according to $\psi_f \propto (\partial_X - W_f)(\partial_X + W)\psi$. As a result, all family members share the same guided wave characteristics, e.g., they have identical sets of eigenvalues as in the case of broken SUSY. This in turn means that an unbroken SUSY partner cannot be a part of the isospectral family associated with its fundamental structure, since the superpartner per definition lacks one guided mode. Nevertheless, SUSY optical transformations can be employed to synthesize dedicated isospectral families for any initial index landscape. Figures 2(f)–2(h) provide an overview of the

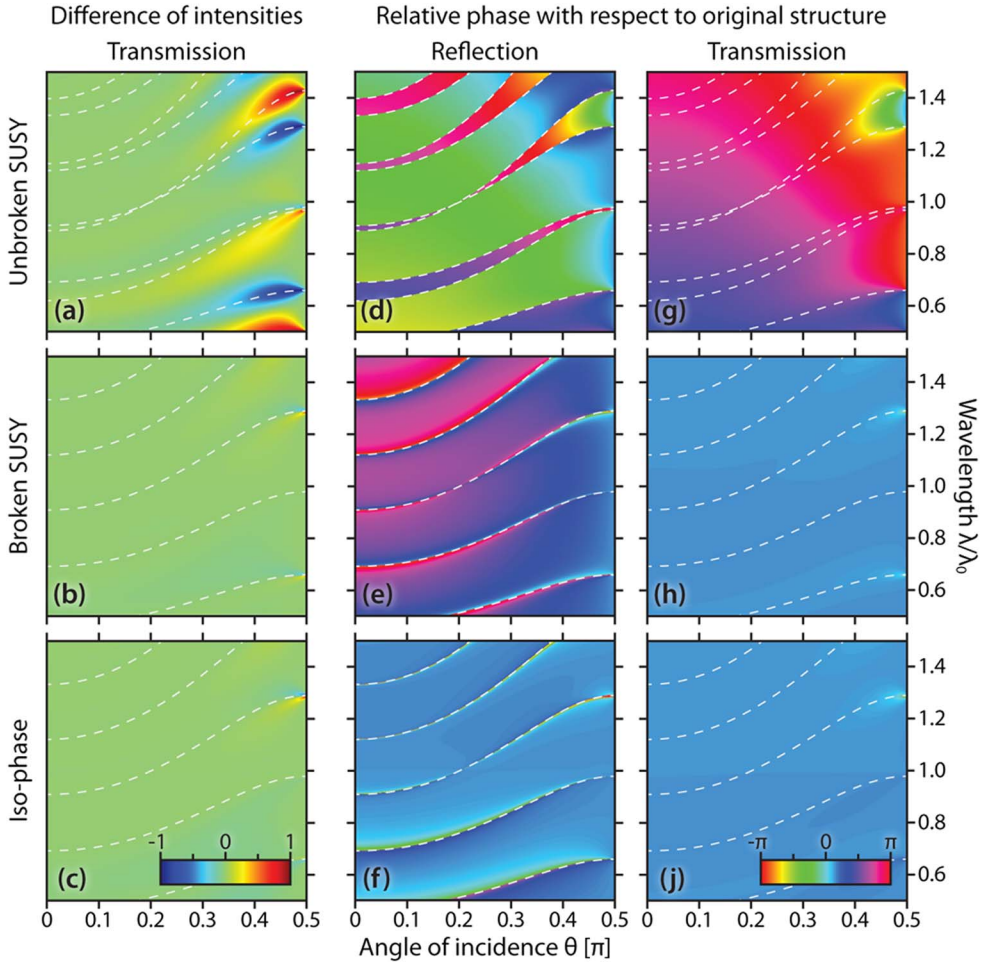

Fig. 3. Reflection/transmission characteristics of structures obtained by SUSY transformations depicted in Fig. 2 as functions of wavelength λ and angle of incidence θ. (a–c) Intensity difference in transmission. (d–f) Relative phases in reflection and (g–j) relative phases in transmission. The dashed lines follow the phase jumps of π, which originate from the interaction with guided modes in the fundamental structure and unbroken-SUSY partner. Top row, unbroken SUSY; middle row, broken SUSY; bottom row, isophase case ($C = 0.5$).

different superpotential functions in the regimes of unbroken and broken SUSY [Figs. 2(b), 2(c)], as well as for the family members shown in Fig. 2(d).

4. SCATTERING CHARACTERISTICS

Let us now turn our attention to the scattering characteristics of structures connected by SUSY transformations. Consider a plane wave $\exp(iXn_0 \cos\theta + iYn_0 \sin\theta)$ incident from the left, i.e., $X \to -\infty$, as shown schematically in Fig. 2(e). For reasons of simplicity, we assume a uniform background medium $n_+ = n_- = n_0$ at $X \to \pm\infty$; the general case of $n_+ \neq n_-$ is discussed in Supplement 1. Here, the reflected and transmitted waves in the far field are given as $r\exp(-iXn_0 \cos\theta + iYn_0 \sin\theta)$ and $t\exp(iXn_0 \cos\theta + iYn_0 \sin\theta)$ in terms of the complex reflection and transmission coefficients r and t [24]. By adopting similar solutions for the partner scatterer ϵ_p, its respective reflection and transmission coefficients r_p and t_p can readily be found. This is done by using the intervening relation $\psi_p \propto (\partial_X + W)\psi$, which connects the scattering states of the original structure to those of the superpartners. A similar approach can be followed for the isospectral configuration by utilizing $\psi_f \propto (\partial_X - W_f)(\partial_X + W)\psi$. Further details concerning this procedure can be found in Supplement 1. Table 1 summarizes the relations between the complex reflection/transmission coefficients of the original and the unbroken and broken superpartners, as well as the isophase families.

Interestingly, the SUSY transformation yields a partner structure with exactly the same absolute values in reflection and transmission, as illustrated in Fig. 2(j). Evidently, all the permittivity distributions from Figs. 2(a)–2(d) display identical reflectivities $R = |r|^2 = |r_p|^2$ and transmittivities $T = 1 - R$ for all angles of incidence. In contrast, the scattering phases depend on whether SUSY is broken or not (see Table 1). In the case of unbroken SUSY, both reflection and transmission coefficients acquire additional phases with respect to the fundamental scattering potential. If on the other hand SUSY is broken, the transmission coefficient is the same in both amplitude and phase. Finally, each member of the parametric family ϵ_f directly inherits all scattering properties of the original structure (in both intensity and phase), i.e., they are phase equivalent to ϵ. Figures 2(k)–2(m) illustrate these relations.

So far, the performance of these systems has been examined at a given operating wavelength λ_0. Of importance would be to investigate to what extent their supersymmetric properties persist when the wavelength λ varies around λ_0. As one would expect, even if two dissimilar profiles exhibit the same phases at a given wavelength, their internal light dynamics may gradually undergo different changes with λ. To elucidate this structural dispersion, we provide the spectral dependence of the difference in transmittivities ΔT (or reflectivities ΔR) between the fundamental structure [Fig. 2(a)] and its superpartners [Figs. 2(b)–2(d)] as a function of the incidence angle θ, as shown in Figs. 3(a)–3(c). As these figures indicate, this difference only becomes notable in the unbroken SUSY regime [Fig. 3(a)], while it is almost absent under broken SUSY and isophase conditions [Figs. 3(b), 3(c)]. The difference in the corresponding reflection phases is similarly presented in Figs. 3(d)–3(f). The dashed lines trace the abrupt phase jumps of π, which mark the interaction with guided modes in the two partners and intersect at the design wavelength λ_0. Evidently, the isophase design displays the greatest resilience with respect to spectral deviations. Note that such phase jumps do not occur in the transmission phases, as can be seen in Figs. 3(g)–3(j). In this latter case, the isophase system again proves to be the least susceptible to spectral deviations. These results demonstrate that SUSY transformations can be robust over a broad spectral range around the design wavelength.

5. REFRACTIVE INDEX ENGINEERING USING SUSY TRANSFORMATIONS

One of the main challenges in designing optical systems is the limited dynamic range of refractive indices associated with available materials. This issue becomes particularly acute when high-contrast arrangements are desirable. For example, the number of grating unit cells required to achieve a certain diffraction efficiency grows with the inverse logarithm of the index contrast n_2/n_1 between the individual layers [23]. As it turns out, SUSY optical transformations can be utilized to reduce the index contrast needed for a given structure. This can be done through a hierarchical ladder of superpartners, i.e., sequentially removing the bound states of the original high-contrast setting [Fig. 4(a)]. In this example, the relative permittivity in the original structure is supposed to vary between 2 and 9, leading to a considerable contrast. Evidently, this range may be difficult to implement in practice in such a wavelength-scale arrangement. On the other hand, each successive step demands less contrast in the corresponding index landscape than the previous one [Fig. 4(b)]. We would like to point out that since reflection and transmission are only relevant for propagating waves, the removal of guided modes is in no way detrimental to scattering-based functionalities. The ultimate result is a low-contrast equivalent structure that fully inherits the intensity reflectivity R and transmittivity T of the original configuration under all incident angles [Figs. 4(c)–4(d)]. For this particular example, we see an approximately four-fold decrease in the required permittivity contrast.

Finally, SUSY transformations can provide a possible avenue in replacing negative-permittivity inclusions (typically accompanied by losses) by purely dielectric materials. In this respect, inverse SUSY transformations, which now add modes with certain propagation constants to a given structure, can instead be used to locally elevate the permittivity (see Supplement 1). Along similar lines, it is possible to find superpotentials that relate a structure with metallic or negative-permittivity regions to an equivalent arrangement with entirely positive ε, as depicted in Fig. 5. Here, we make use of the fact that in a broken-SUSY transformation, the spatial average of ϵ happens to be a conserved quantity. Therefore, changes in the broader vicinity of the original metal–dielectric structure can be used to achieve this goal.

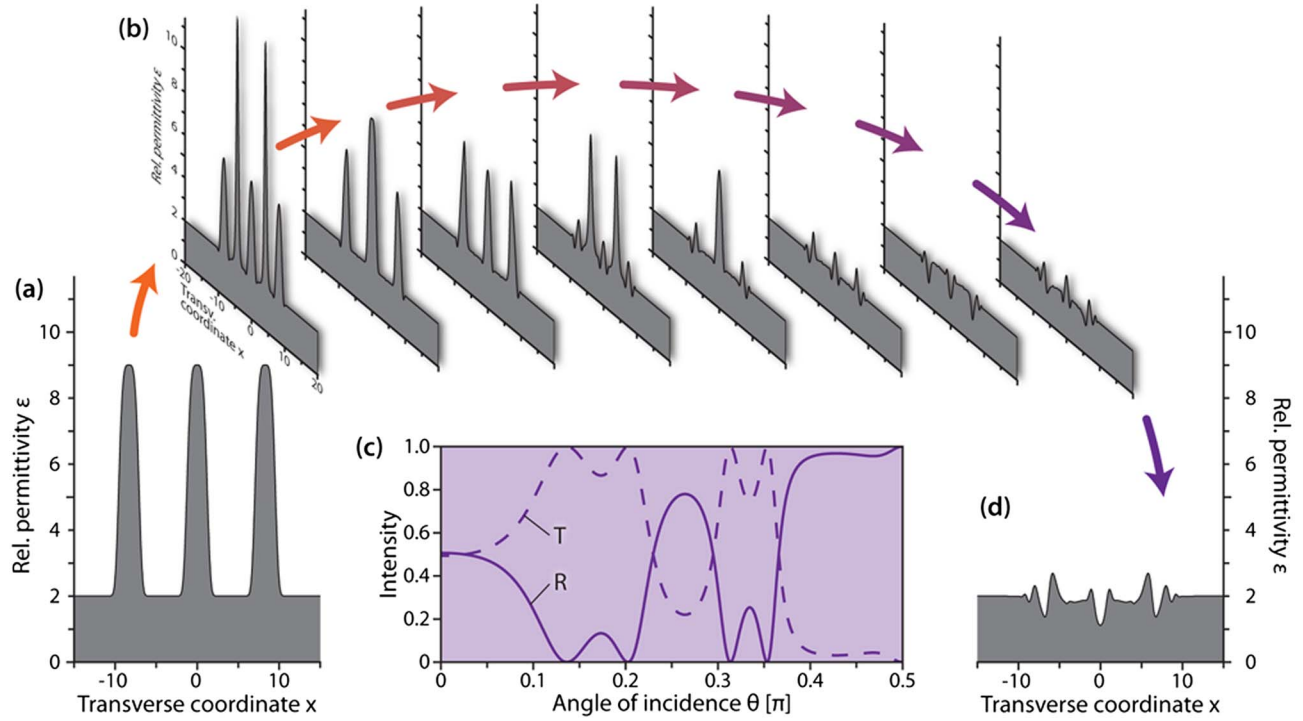

Fig. 4. (a) Hypothetical high-contrast dielectric layer arrangement that supports $N = 9$ guided modes. (b) Hierarchical sequence of partner structures obtained through iterative SUSY transformations. (c) Despite the general trend toward lower-contrast configurations, each intermediate step inherits the reflectivity and transmittivity of the fundamental system (a). (d) The resulting low-contrast structure is free of bound states and faithfully mimics the intensity-scattering characteristics of the original high-contrast configuration for all angles of incidence. Note that the transverse coordinate x scales in units of $\lambda_0/2\pi$.

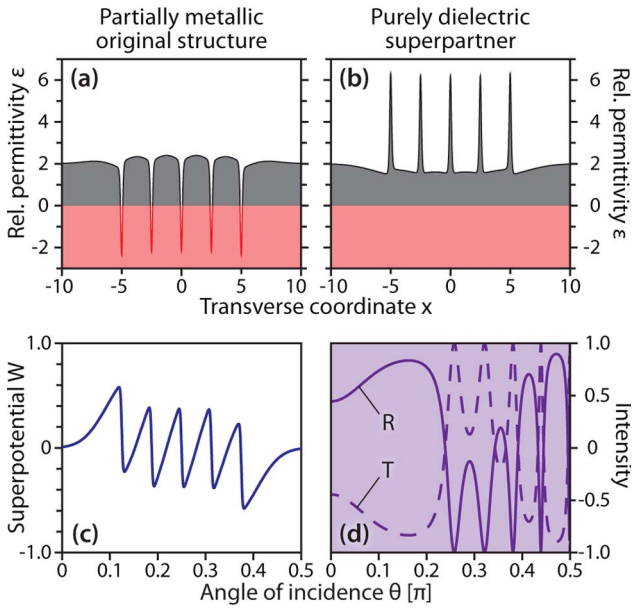

Fig. 5. (a) Metal–dielectric grating arrangement comprising five layers of negative electrical permittivity (red sections). (b) An entirely dielectric superpartner grating constructed in the broken SUSY regime, using the respective superpotential (c). (d) Despite the absence of any metallic regions, the equivalent structure exhibits identical reflectivities/transmittivities.

6. CONCLUSION

We have introduced a new type of supersymmetric optical transformation for arbitrary 1D refractive index landscapes. Compared to conventional transformation optics, our approach poses significantly less stringent requirements on the constituent parameters, and does not involve any modifications to the magnetic response of the materials involved. This method can be utilized to construct photonic arrangements that faithfully mimic the scattering characteristics of high-index-contrast or even metal–dielectric structures. We would like to emphasize that this approach is readily capable of emulating the behavior of arrangements whose permittivity distributions are far beyond the reach of naturally occurring materials. As such, SUSY transformation optics can likewise be employed to narrow the necessary range of effective parameters, and thereby complement the design process of metamaterial devices. SUSY transformation optics may have potential applications in a wide range of scenarios that rely on engineered scattering and transmission properties such as, for example, optical metasurfaces, antireflection coatings, and diffraction gratings. Of interest will be to explore how the aforementioned strategies could be paired up with recently developed transformation schemes for guided-wave photonics based on dielectric materials [25,26]. Finally, the unique characteristics of supersymmetric optical structures may open new opportunities for tailoring the response of non-Hermitian systems beyond PT symmetry [27], and could be employed for a new class of integrated optical mode converters [28].

FUNDING INFORMATION

Air Force Office of Scientific Research (AFOSR) (FA9550-14-1-0037, FA9550-12-1-0148); National Science Foundation (NSF) (ECCs-1128520); The German National Academy of Sciences Leopoldina (LPDS 2012-01).

See Supplement 1 for supporting content.

REFERENCES

1. I. M. Gel'fand and B. M. Levitan, "On the determination of a differential equation from its spectral function," Izvest. Akad. Nauk. **15**, 309–360 (1951).
2. E. Wolf, "Three-dimensional structure determination of semi-transparent objects from holographic data," Opt. Commun. **1**, 153–156 (1969).
3. K. Chadan and P. C. Sabatier, *Inverse Problems in Quantum Scattering Theory* (Springer, 1977).
4. P. Deift and E. Trubowitz, "Inverse scattering on the line," Comm. Pure Appl. Math. **32**, 121–251 (1979).
5. I. Kay and H. E. Moses, "Reflectionless transmission through dielectrics and scattering potentials," J. Appl. Phys. **27**, 1503–1508 (1956).
6. E. Witten, "Dynamical breaking of supersymmetry," Nucl. Phys. **B185**, 513–554 (1981).
7. F. Cooper, A. Khare, and U. Sukhatme, "Supersymmetry and quantum mechanics," Phys. Rep. **251**, 267–385 (1995).
8. M. M. Nieto, "Relationship between supersymmetry and the inverse method in quantum mechanics," Phys. Lett. B **145**, 208–210 (1984).
9. A. Neveu and J. H. Schwarz, "Factorizable dual model of pions," Nucl. Phys. **B31**, 86–112 (1971).
10. A. Khare and U. Sukhatme, "Phase-equivalent potentials obtained from supersymmetry," J. Phys. A **22**, 2847–2860 (1989).
11. J. B. Pendry, D. Schurig, and D. R. Smith, "Controlling electromagnetic fields," Science **312**, 1780–1782 (2006).
12. U. Leonhardt, "Optical conformal mapping," Science **312**, 1777–1780 (2006).
13. A. Vakil and N. Engheta, "Transformation optics using graphene," Science **332**, 1291–1294 (2011).
14. V. M. Shalaev, "Transforming light," Science **322**, 384–386 (2008).
15. U. Leonhardt and T. G. Philbin, "Transformation optics and the geometry of light," Prog. Opt. **53**, 69–152 (2009).
16. H. Chen, C. T. Chan, and P. Sheng, "Transformation optics and metamaterials," Nat. Mater. **9**, 387–396 (2010).
17. A. Alù, M. Silveirinha, A. Salandrino, and N. Engheta, "Epsilon-near-zero metamaterials and electromagnetic sources: tailoring the radiation phase pattern," Phys. Rev. B **75**, 155410 (2007).
18. G. W. Milton, M. Briane, and J. R. Willis, "On cloaking for elasticity and physical equations with a transformation invariant form," New J. Phys. **8**, 248 (2006).
19. J. Valentine, J. Li, T. Zentgraf, G. Bartal, and X. Zhang, "An optical cloak made of dielectrics," Nat. Mater. **8**, 568–571 (2009).
20. L. H. Gabrielli, J. Cardenas, C. B. Poitras, and M. Lipson, "Silicon nanostructure cloak operating at optical frequencies," Nat. Photonics **3**, 461–463 (2009).
21. Y. Lai, J. Ng, H. Y. Chen, D. Z. Han, J. J. Xiao, Z.-Q. Zhang, and C. T. Chan, "Illusion optics: the optical transformation of an object into another object," Phys. Rev. Lett. **102**, 253902 (2009).
22. B. Zhang, Y. Luo, X. Liu, and G. Barbastathis, "Macroscopic invisibility cloak for visible light," Phys. Rev. Lett. **106**, 033901 (2011).
23. P. Yeh, A. Yariv, and C. S. Hong, "Electromagnetic propagation in periodic stratified media. I. General theory," J. Opt. Soc. Am. **67**, 423–438 (1977).
24. M.-A. Miri, M. Heinrich, R. El-Ganainy, and D. N. Christodoulides, "Supersymmetric optical structures," Phys. Rev. Lett. **110**, 233902 (2013).
25. H. Xu, B. Zhang, T. Yu, G. Barbastathis, and H. Sun, "Dielectric waveguide bending adapter with ideal transmission: practical design strategy of area-preserving affine transformation optics," J. Opt. Soc. Am. B **29**, 1287–1290 (2012).
26. D. Liu, L. H. Gabrielli, M. Lipson, and S. G. Johnson, "Transformation inverse design," Opt. Express **21**, 14223–14243 (2013).
27. M.-A. Miri, M. Heinrich, and D. N. Christodoulides, "Supersymmetry-generated complex optical potentials with real spectra," Phys. Rev. A **87**, 043819 (2013).
28. M. Heinrich, M.-A. Miri, S. Stützer, R. El-Ganainy, S. Nolte, A. Szameit, and D. N. Christodoulides, "Supersymmetric mode converters," Nat. Commun. **5**, 3698 (2014).

Research Article Vol. 1, No. 2 / August 2014 / Optica 96

Transparent subdiffraction optics: nanoscale light confinement without metal

SAMAN JAHANI AND ZUBIN JACOB*

Department of Electrical and Computer Engineering, University of Alberta, Edmonton T6G 2V4, Canada

**Corresponding author: zjacob@ualberta.ca*

Received 9 April 2014; revised 17 June 2014; accepted 23 June 2014 (Doc. ID 209661); published 12 August 2014

The integration of nanoscale electronics with conventional optical devices is restricted by the diffraction limit of light. Metals can confine light at the subwavelength scales needed, but they are lossy, while dielectric materials do not confine evanescent waves outside a waveguide or resonator, leading to cross talk between components. We introduce a paradigm shift in light confinement strategy and show that light can be confined below the diffraction limit using completely transparent artificial media (metamaterials with $\varepsilon_{ij} > 1, \mu_{ij} = 1$). Our approach relies on controlling the optical momentum of evanescent waves—an important electromagnetic property overlooked in photonic devices. For practical applications, we propose a class of waveguides using this approach that outperforms the cross-talk performance by 1 order of magnitude as compared to any existing photonic structure. Our work overcomes a critical stumbling block for nanophotonics by completely averting the use of metals and can impact electromagnetic devices from the visible to microwave frequency ranges.

OCIS codes: (250.5403) Plasmonics; (160.3918) Metamaterials.

http://dx.doi.org/10.1364/OPTICA.1.000096

1. INTRODUCTION

Modern computation and communication systems rely on the ability to route and transfer information using electronic and electromagnetic signals. Massive efforts over the last decade have been driven by miniaturization and integration of electronics and photonics on the same platform [1]. However, the diffraction limit of light is a fundamental barrier to interfacing micrometer-scale waveguides to nanoscale electronic circuitry. Furthermore, dense photonic integration is hampered because cross talk between waveguides increases as the separation between them is reduced.

At low frequencies, metals, due to their high reflectivity, can be used for confining light at the subwavelength scale [2]. At optical frequencies, metals can achieve the same task by coupling light to free electrons. This leads to a surface plasmon polariton (SPP) that shows properties of nanoscale waveguiding [3,4]. However, due to absorption in metals, this approach cannot guide light more than a few micrometers [3,5,6]. Furthermore, the dissipated energy leads to thermal issues, which are especially significant in miniaturized circuits, hindering dense photonic integration. Hence, low-loss approaches to light confinement at the nanoscale are a fundamental necessity for photonics.

Prevalent all-dielectric nanophotonic approaches can be classified according to two fundamental principles governing them, one that utilizes the large index contrast between media to confine light within nanoscale slots [7–9] and another that uses Bragg reflection of waves in the bandgap of photonic crystals [10–12]. However, neither of these approaches functions on the evanescent fields outside the core of the resonator or waveguide. These unchecked evanescent waves are the fundamental origin of cross talk in nanophotonics and this significantly limits the ability of these classes of dielectric waveguides for photonic integration [13,14].

In this paper, we surpass the diffraction limit of light by a new class of all-dielectric artificial materials that are lossless. This overcomes one of the fundamental challenges of light confinement in metamaterials and plasmonics: metallic loss. Our approach relies on controlling the optical momentum of evanescent waves as opposed to conventional photonic devices, which manipulate propagating waves. This leads to

a counterintuitive confinement strategy for electromagnetic waves across the entire spectrum. Finally, based on these momentum transformations, we propose a class of practically achievable waveguides that exhibit dramatically reduced cross talk compared to any dielectric waveguide (slot, photonic crystal, or conventional).

2. PARADIGM SHIFT IN LIGHT CONFINEMENT STRATEGY

We introduce two distinct photonic design principles that can ideally lead to subdiffraction light confinement without metal.

A. Relaxed Total Internal Reflection

First, we revisit the conventional light confinement mechanism of total internal reflection (TIR), which is widely utilized for waveguides and resonators. We consider a simple 2D case with an interface along the z axis between medium 1 and medium 2 and TM-polarized incident light. A habitual prejudice immediately leads us to conclude that $n_1 > n_2$ is the condition for total internal reflection of light moving from medium 1 to medium 2 [Fig. 1(a)]. Here, we argue that the above is a sufficient but not necessary condition and the requirement can be relaxed to

$$n_1 > \sqrt{\varepsilon_x}, \tag{1}$$

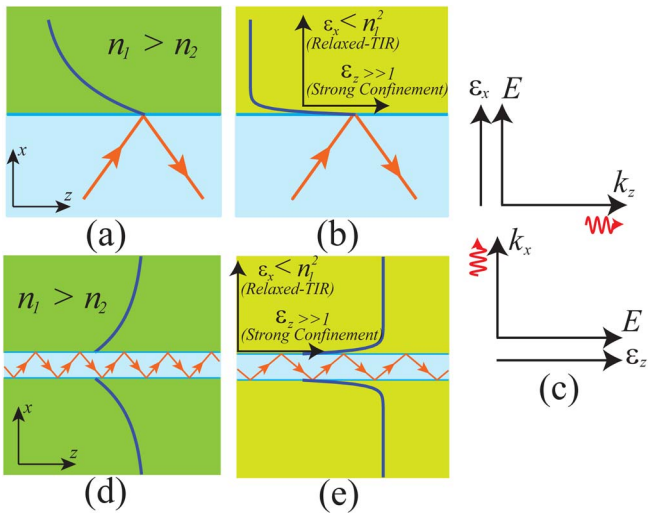

Fig. 1. (a) Conventional TIR: if $n_1 > n_2$ and the incident angle is larger than the critical angle, the light is totally reflected to medium 1 and decays in medium 2. (b) Relaxed-TIR: if $n_1 > \sqrt{\varepsilon_x}$ and the incident angle is larger than the critical angle, the light is totally reflected. However, the penetration depth can be decreased considerably if $\varepsilon_z \gg 1$. (c) Wave propagation along the optical axis of a uniaxial medium. As the electric field is perpendicular to the momentum direction, permittivity in a specific direction controls the momentum in the perpendicular direction. (d) Conventional waveguide based on TIR: as the core size is decreased, most of the power lies outside and decays slowly in the cladding. (e) TCW: relaxed-TIR ($n_1 > \sqrt{\varepsilon_x}$) preserves the conventional waveguiding mechanism. Furthermore, the light decays fast in the cladding as the optical momentum in the cladding is transformed using anisotropy ($\varepsilon_z \gg 1$). Thus, the wave can be confined inside the core, giving rise to subdiffraction optics with completely transparent media.

where the z axis is parallel to the interface and the x axis is normal to it. Note that ε_x is defined as the dielectric constant of medium 2 perpendicular to the interface. We call this condition relaxed-TIR. We provide a simple proof of this using momentum conservation of light parallel to the interface in uniaxial anisotropic media. The tangential momentum of light, $k_z^{\parallel} = n_1 k_0 \sin\theta$, is conserved along the interface. Here, $k_0 = \omega/c = 2\pi/\lambda$ is the free-space wave vector of light and θ is the angle of incidence. Once the light enters medium 2, even though the parallel momentum is conserved, the dispersion relation of TM polarized waves changes to

$$\frac{(k_z^{\parallel})^2}{\varepsilon_x} + \frac{(k_x^{\perp})^2}{\varepsilon_z} = (k_0)^2. \tag{2}$$

We see that the perpendicular component of the wave vector in the second medium $k_x^{\perp}$ can be zero or imaginary (evanescent wave) if $k_z^{\parallel} > \sqrt{\varepsilon_x} k_0$, i.e., $n_1 > \sqrt{\varepsilon_x}$. Note that, as expected, for angles of incidence greater than the critical angle of relaxed-TIR ($\theta_c = \sin^{-1}(\sqrt{\varepsilon_x}/n_1)$), we have an evanescent wave decaying into medium 2.

B. Transforming Optical Momentum

In conventional TIR, the evanescent wave penetrates considerably into medium 2. Here, we show how to transform the optical momentum of evanescent waves, leading to a reduced penetration depth in medium 2 after TIR. The argument in the previous subsection about relaxed-TIR opens up a fundamentally new degree of freedom for confining evanescent waves penetrating into medium 2: the component of the dielectric tensor parallel to the interface. The evanescent wave decay constant for TM-polarized waves in medium 2 is given by

$$k_x^{\perp} = \sqrt{\frac{\varepsilon_z}{\varepsilon_x}} \sqrt{\varepsilon_x (k_0)^2 - (k_z^{\parallel})^2}. \tag{3}$$

The penetration depth (skin depth) of evanescent fields into the second medium is thus governed by the ratio of permittivity components $\sqrt{\varepsilon_z/\varepsilon_x}$. We thus arrive at the condition $\varepsilon_z \gg 1$ to increase the momentum of evanescent waves, i.e., make them decay faster, which confines them very close to the interface. Note that since we have decoupled the TIR criterion ($n_1 > \sqrt{\varepsilon_x}$) from the momentum confinement condition ($\varepsilon_z \gg 1$), both can be simultaneously achieved, leading to a fundamentally new approach to light confinement in transparent media [Fig. 1(b)].

C. Controlling Optical Momentum with Dielectric Anisotropy

In essence, our nonresonant transparent medium alters the momentum of light entering it. The upper limit to the momentum tangential to the interface is set by the dielectric constant perpendicular to the interface, while the perpendicular momentum is increased by the dielectric constant parallel to the interface. This nonintuitive concept of controlling wave momentum in a given direction by the dielectric constant perpendicular to the phase propagation is depicted in Fig. 1(c). It is seen that, for plane wave propagation along the symmetry

axes of anisotropic media, the field direction and the relevant dielectric tensor component are perpendicular to the wave vector (k_x governed by ε_z and k_z governed by ε_x).

3. SUBDIFFRACTION LIGHT CONFINEMENT WITHOUT METAL

We now show how the previous momentum transformations can be used for subdiffraction confinement of light without metallic plasmons. Note that our approach can be applied to multiple devices across the visible, terahertz, and microwave regimes; however, for the sake of elucidation, we consider a waveguide geometry.

As the core size of a conventional slab waveguide is decreased, all modes are cut off, except the lowest order TE and TM modes. Even though these modes exist, most of the power actually lies outside the core and decays very slowly in air (cladding). We propose to use metamaterial claddings that transform the momentum of evanescent waves and confine the light within the core of the waveguide [Figs. 1(d) and 1(e)]. We call such waveguides as extreme skin depth (e-skid) waveguides. We emphasize the counterintuitive nature of the waveguiding since the index of the cladding averaged over all directions is greater than that of the core. The relaxed-TIR condition still allows the lowest order mode to propagate, similar in principle to the conventional case. Note that the confinement is achieved for the TM_0 mode since the dispersion relation is anisotropic only for TM waves.

In Fig. 2, we show the field plots for the fundamental mode in a conventional waveguide and a 1D e-skid waveguide. This engineered anisotropy allows us to control the evanescent field outside the core. For the same input energy, we note the increased power in the core and a striking difference between the evanescent decay in the cladding for the two waveguides.

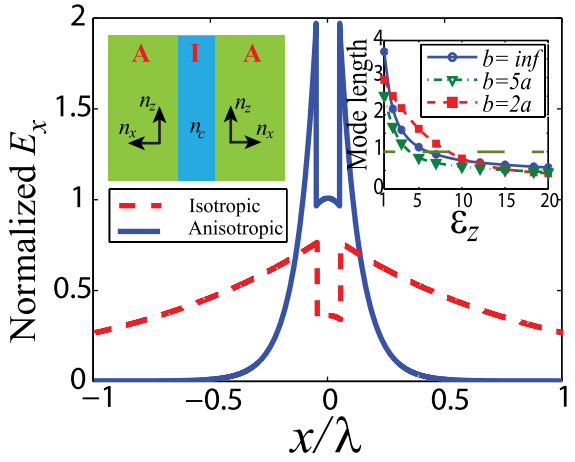

Fig. 2. Normalized tangential electric field of the TM mode for a glass slab waveguide with a size of 0.1λ surrounded with all-dielectric metamaterial cladding. The metamaterial has dielectric constants of $\varepsilon_x = 1.1$ and $\varepsilon_z = 15$. On comparison with a conventional mode that has air as the surrounding medium, a rapid decay of the evanescent fields is observed. The plots are normalized to the same input electric energy. Inset: as the anisotropy of the cladding is increased, the mode length decreases significantly below the diffraction limit with completely transparent media. This can be achieved with a cladding size (width b) three times that of the core size (width a).

We follow the conventional definition of mode length adopted from the concept of mode volume in quantum optics and widely used in nanoscale waveguide theory [5,15]. For the lowest order TM_0 waveguide mode, it is given by $L_m = \int_{-\infty}^{\infty} W(x)\mathrm{d}x / \max\{W(x)\}$, where $W(x)$ is the energy density of the mode [5,15]. It is clear from the inset of Fig. 2 that the mode length is diffraction limited (above $\lambda/2n_{\mathrm{core}}$) for conventional waveguides. However, once the cladding is made anisotropic, the mode length achieves subdiffraction values. We plot the role of the component of the dielectric tensor (ε_z) that is responsible for confining the evanescent waves. The increase of this constant helps compress the evanescent waves in the cladding, decreasing the mode length below the diffraction limit when the index crosses $n_z = \sqrt{\varepsilon_z} \approx 3$. We emphasize that this is within reach at optical communication wavelengths. The anisotropic metamaterial cladding also achieves a significantly better power confinement in the core as compared to the conventional waveguide (Fig. 3). This increase in power confinement is accompanied by a proportionate decrease in mode length as compared to the conventional waveguide (Fig. 3, inset). For any given core, irrespective of its subwavelength size, we can achieve subdiffraction confinement of light and extreme power concentration in the core if the cladding anisotropy is increased. Note the diffraction limit is defined as per convention with respect to the core index where most of the power is confined. This shows that optical mode volumes can also be governed by the index felt by the evanescent fields outside of the core.

The optimum performance occurs when $\varepsilon_x \to 1^+$ and $\varepsilon_z \gg 1$. In Supplement 1 we show a detailed study that the cladding anisotropy and cladding size are degrees of freedom that can be exploited to confine the mode, irrespective of core index and core size.

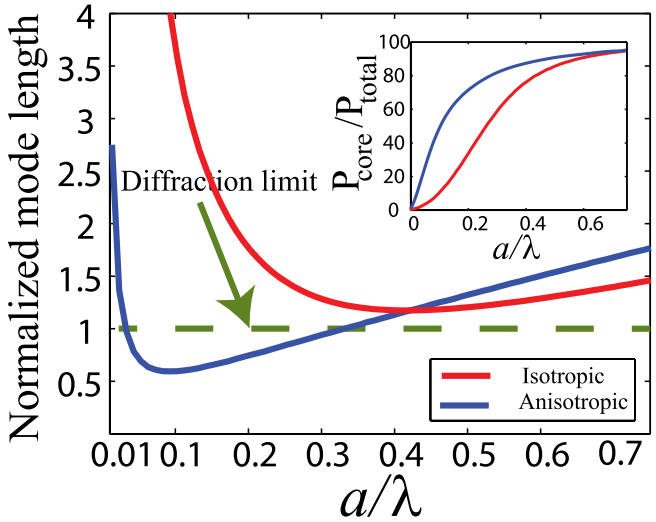

Fig. 3. Mode length comparison of slab waveguides with core size. It shows that the anisotropic cladding ($\varepsilon_x = 1.1$ and $\varepsilon_z = 15$) can confine the TM mode to subdiffraction values. Inset: we emphasize that the net power in the core is also higher for the TCW as compared to conventional waveguides.

We have decoupled the momentum of the propagating mode in the core (related to effective mode index) from the momentum of the evanescent wave in the cladding (related to confinement). This implies that the enhanced confinement does not require a high effective mode index, in contrast to conventional approaches. We expect this fundamental difference to be a major design advantage for mode matching in various devices and couplers.

4. 1D PRACTICAL REALIZATION

We discuss how to practically achieve these momentum transformations. First, we argue that no naturally occurring medium has a strong anisotropy, and the maximum contrast between permittivity tensor components is low for natural dielectrics (e.g., TiO_2) and artificial polymers [16]. Thus, we cannot use natural dielectrics to preserve TIR with a glass or silicon waveguide core interface while simultaneously increasing the momentum of evanescent waves. However, we can realize this extreme anisotropy by artificially structured media using available lossless dielectrics.

One practical approach consists of a multilayer structure consisting of two materials with high index contrast and layer thicknesses far below the wavelength of light [17]. Effective medium theory [18] for this superlattice predicts a homogenized medium with an anisotropic dielectric tensor given by $\varepsilon_{\parallel} = \varepsilon_{\text{high}}\rho + \varepsilon_{\text{low}}(1-\rho)$, where $\varepsilon_{\parallel}$ is the dielectric constant parallel to the layers and $1/\varepsilon_{\perp} = \rho/\varepsilon_{\text{high}} + (1-\rho)/\varepsilon_{\text{low}}$ is the dielectric constant perpendicular to the layers. ρ is the fill fraction of the high-index material $\varepsilon_{\text{high}}$.

A. Application to Photonic Integration

The major advantage of our approach for practical applications is the reduction in cross talk once the metamaterial is introduced in the region between any conventional dielectric waveguides. This is because our approach relies on altering the evanescent field outside the core for confinement, the fundamental origin of cross talk. This is a key figure of merit for photonic integration [19] and we outperform state-of-the-art structures by 1 order of magnitude taking nonidealities into account.

Figure 4(a) shows the schematic for two coupled slab waveguides where the cladding has been transformed to allow TIR and cause fast decay of evanescent waves in the cladding to reduce the cross talk. We consider two silicon slab waveguides ($n_{\text{Si}} = 3.47$) with a center-to-center separation of $s = 0.5\lambda$. A periodic multilayer combination of high-index and low-index dielectrics shows the extreme effective anisotropy that is needed for the optical momentum transformation. The metamaterial claddings are made of high-index ($n_1 = 4.3$) and low-index thin films ($n_2 = 1.5$) at the operating wavelength of 1550 nm. Two representative materials with such indices are germanium and silica. We emphasize that the band-edge loss at 1.55 μm in germanium is not a fundamental impediment. For a medium 1 filling fraction of $\rho = 0.6$, multilayer effective medium theory predicts anisotropic dielectric constants of $\varepsilon_x = 4.8$ and $\varepsilon_z = 11.9$. Figure 4(b) shows the coupling length of the fundamental mode in the waveguide with increasing core size. For comparison, we also show the coupling length when the surrounding medium is simply silica. A dramatic impact of the anisotropy is clearly evident in the coupling length, which shows 1 order of magnitude increase for various core sizes for the transformed cladding structure. For completeness, we have also compared the cross-talk performance of our waveguide with another state of the art structure—slot waveguides [7,13]. Higher index cores in slot waveguides and photonic crystals can lead to enhanced power confinement; however, the cross talk of our TCWs always outperforms them by 1 order of magnitude.

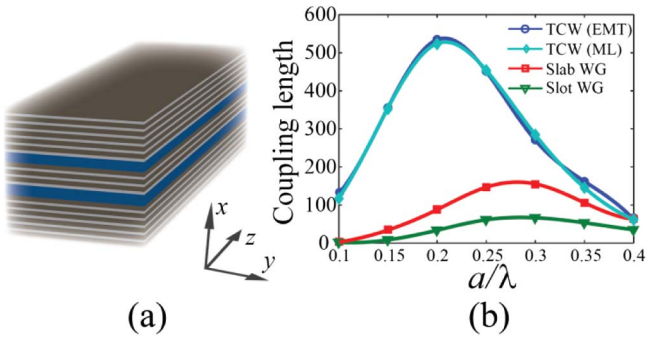

Fig. 4. Dense photonic integration at optical telecommunication wavelength ($\lambda = 1550$ nm). (a) Extreme skin depth cladding with low cross talk between closely spaced waveguides. This can be achieved by surrounding the waveguide cores (thick blue layers) with multilayer all-dielectric metamaterials. The multilayer metamaterial consists of alternating subwavelength layers of germanium (26 nm) and silica (14 nm). This all-dielectric structure achieves anisotropy of $\varepsilon_x = 4.8$ and $\varepsilon_z = 11.9$. (b) Comparison of coupling length (cross talk) for conventional slab waveguides, slot waveguides, and TCWs. It is seen that the TCW improves the cross talk by 1 order of magnitude and the practical multilayer structure result is in excellent agreement with the effectively anisotropic cladding. The core is silicon with a center-to-center separation of 0.5λ between waveguides. Each slot waveguide has the same net size as the core of the other waveguides; the slot size is 0.01λ and is filled with glass. If the slot size is larger or the slot index is lower, the cross-talk performance is worse than that shown. Also note that the slot waveguide cross talk is, in fact, always more than that in the conventional waveguide.

The anisotropic cladding can be exploited for designing bends and splitters, as well. The dielectric constant of the cladding perpendicular to the core governs TIR and can be minimized or altered to decrease power loss. A detailed analysis of quasi-2D waveguides, splitters and bends with extreme skin depth claddings and their performance will be presented elsewhere, but we now focus on showing how our approach can be generalized to 2D waveguides.

5. 2D EXTREME SKIN DEPTH WAVEGUIDES

The momentum transformation can be used to strongly confine light in an infinitely long glass rod with an arbitrarily shaped cross section ($A \ll \lambda^2$). The cladding has to be anisotropic to allow for the lowest order mode (HE11) to travel inside the glass core and bounce off by TIR but simultaneously decay away rapidly, causing subdiffraction confinement of the mode (Fig. 5). The set of nonmagnetic media that can cause the momentum transformation are anisotropic

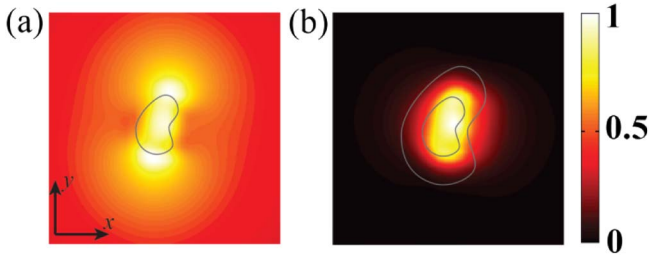

Fig. 5. Simulated distribution of the electric energy density inside a low-index 2D dielectric waveguide with arbitrary cross section using metamaterial claddings. (a) Waveguide without cladding, and (b) the waveguide with all-dielectric nonmagnetic cladding ($\varepsilon_x = \varepsilon_y = 1.2$ and $\varepsilon_z = 15$). When the anisotropic cladding is added, the mode area of the waveguide is decreased from about $80\,A_0$ to $0.7\,A_0$, and the fraction of power inside the core to the total power is increased from less than 1% to about 36%.

homogenous dielectric materials with $1 < \varepsilon_x = \varepsilon_y < \varepsilon_{\text{glass}}$ and $\varepsilon_z \gg 1$.

The simulated electric energy density of the arbitrarily shaped waveguide with an all-dielectric anisotropic cladding ($\varepsilon_x = \varepsilon_y = 1.2$ and $\varepsilon_z = 15$) is shown in Fig. 5(b). The shape of the cladding is chosen to be the same shape as the arbitrary core, but with twice the local radius. The numerical calculation shows that about 36% of the total power is inside the low-refractive-index core and the mode area for this waveguide is about $0.7\,A_0$ ($A_0 = (\lambda/2n_{\text{core}})^2$). Note that, without the momentum transformed cladding, the fundamental mode of the subwavelength core is weakly guided and most of the power lies outside the core [Fig. 5(a)]. The calculated mode area for the bare waveguide is about $80\,A_0$ and only 1% of the total power lies inside the core. Availability of high-index building blocks for metamaterials at lower frequencies can lead to better performance specifically for the 2D designs [20]. Nanowire metamaterials in the cladding can achieve the desired anisotropy (see Supplement 1).

6. CONCLUSION

In conclusion, we have introduced a paradigm shift in light confinement strategy that rests on transforming the momentum of evanescent waves. Our transformations can be achieved by all-dielectric media fundamentally overcoming the foremost challenge in the field of plasmonics and metamaterials: optical absorption. We showed that, for practical device applications, the introduction of our engineered anisotropy in the space between conventional waveguides confines evanescent waves and always decreases the cross talk, irrespective of core index or size. The approach of altering the momentum of evanescent waves can be utilized all across the spectrum for electromagnetic waves, leading to a new class of devices that work on controlling evanescent field momentum.

FUNDING INFORMATION

Natural Sciences and Engineering Research Council of Canada, Helmholtz Alberta Initiative.

ACKNOWLEDGMENTS

We wish to acknowledge Prashant Shekhar and Ward Newman for input.

See Supplement 1 for supporting content.

REFERENCES

1. D. A. B. Miller, "Device requirements for optical interconnects to silicon chips," Proc. IEEE **97**, 1166–1185 (2009).
2. S. Ramo, J. R. Whinnery, and T. Van Duzer, *Fields and Waves in Communication Electronics* (Wiley, 1994).
3. D. K. Gramotnev and S. I. Bozhevolnyi, "Plasmonics beyond the diffraction limit," Nat. Photonics **4**, 83–91 (2010).
4. Z. Han and S. I. Bozhevolnyi, "Radiation guiding with surface plasmon polaritons," Rep. Prog. Phys. **76**, 016402 (2013).
5. R. F. Oulton, V. J. Sorger, D. A. Genov, D. F. P. Pile, and X. Zhang, "A hybrid plasmonic waveguide for subwavelength confinement and long-range propagation," Nat. Photonics **2**, 496–500 (2008).
6. R. Zia, M. D. Selker, P. B. Catrysse, and M. L. Brongersma, "Geometries and materials for subwavelength surface plasmon modes," J. Opt. Soc. Am. A **21**, 2442–2446 (2004).
7. V. R. Almeida, Q. Xu, C. A. Barrios, and M. Lipson, "Guiding and confining light in void nanostructure," Opt. Lett. **29**, 1209–1211 (2004).
8. G. S. Wiederhecker, C. M. B. Cordeiro, F. Couny, F. Benabid, S. A. Maier, J. C. Knight, C. H. B. Cruz, and H. L. Fragnito, "Field enhancement within an optical fibre with a subwavelength air core," Nat. Photonics **1**, 115–118 (2007).
9. C. Koos, P. Vorreau, T. Vallaitis, P. Dumon, W. Bogaerts, R. Baets, B. Esembeson, I. Biaggio, T. Michinobu, F. Diederich, W. Freude, and J. Leuthold, "All-optical high-speed signal processing with silicon–organic hybrid slot waveguides," Nat. Photonics **3**, 216–219 (2009).
10. J. D. Joannopoulos, P. R. Villeneuve, and S. Fan, "Photonic crystals: putting a new twist on light," Nature **386**, 143–149 (1997).
11. T. F. Krauss, "Planar photonic crystal waveguide devices for integrated optics," Phys. Status Solidi A **197**, 688–702 (2003).
12. S.-Y. Lin, E. Chow, V. Hietala, P. R. Villeneuve, and J. D. Joannopoulos, "Experimental demonstration of guiding and bending of electromagnetic waves in a photonic crystal," Science **282**, 274–276 (1998).
13. D. Dai, Y. Shi, and S. He, "Comparative study of the integration density for passive linear planar light-wave circuits based on three different kinds of nanophotonic waveguide," Appl. Opt. **46**, 1126–1131 (2007).
14. S. Tomljenovic-Hanic, C. Martijn de Sterke, and M. J. Steel, "Packing density of conventional waveguides and photonic crystal waveguides," Opt. Commun. **259**, 142–148 (2006).
15. S. A. Maier, "Plasmonic field enhancement and SERS in the effective mode volume picture," Opt. Express **14**, 1957–1964 (2006).
16. M. F. Weber, C. A. Stover, L. R. Gilbert, T. J. Nevitt, and A. J. Ouderkirk, "Giant birefringent optics in multilayer polymer mirrors," Science **287**, 2451–2456 (2000).
17. A. Fiore, V. Berger, E. Rosencher, P. Bravetti, and J. Nagle, "Phase matching using an isotropic nonlinear optical material," Nature **391**, 463–466 (1998).
18. G. W. Milton, *The Theory of Composites* (Cambridge University, 2002).
19. G. Veronis and S. Fan, "Crosstalk between three-dimensional plasmonic slot waveguides," Opt. Express **16**, 2129–2140 (2008).
20. P. B. Catrysse and S. Fan, "Transverse electromagnetic modes in aperture waveguides containing a metamaterial with extreme anisotropy," Phys. Rev. Lett. **106**, 223902 (2011).

optica

Spatiotemporal soliton laser

WILLIAM H. RENNINGER* AND FRANK W. WISE

School of Applied and Engineering Physics, Cornell University, Ithaca, New York 14853, USA

**Corresponding author: william.renninger@yale.edu*

Received 10 April 2014; revised 2 June 2014; accepted 4 June 2014 (Doc. ID 209907); published 13 August 2014

Spatiotemporal solitons (STSs) are waves that are localized in all three dimensions of space as well as in time. They are of interest intrinsically as well as for ultrafast optical information processing, but their experimental observation remains a major challenge in nonlinear science. Two decades of investigation of STSs in optics has yielded only a few experimental demonstrations in conservative media. We present the realistic design and modeling of a solid-state laser that depends on the formation of dissipative STSs, which balance nonlinear gain and loss as well as linear and nonlinear phases. Numerical calculations show that stable, three-dimensional solitons can form in lasers containing self-focusing nonlinear materials with large normal dispersion. Experimental realization will be challenging but appears to be technologically achievable.

OCIS codes: (060.5530) Pulse propagation and temporal solitons; (140.3580) Lasers, solid-state; (140.4050) Mode-locked lasers; (190.6135) Spatial solitons.

http://dx.doi.org/10.1364/OPTICA.1.000101

Solitons are localized waves that propagate without decaying. They occur in a variety of physical systems, including liquids [1,2], optical fibers [3], plasmas [4], and condensed matter [5,6]. They generate significant interest fundamentally as well as for applications such as telecommunications. Initial research focused on the nonlinear localization of wave packets in one dimension, such as temporal solitons in optical fibers or spatial solitons in planar waveguides. One of the major goals in the field of nonlinear science is the generation of waves that are localized in all three dimensions of space as well as time [7]. Spatiotemporal solitons (STSs) have been investigated since the early days of nonlinear optics [8,9]. Aside from their intrinsic scientific interest, STSs have potential utility in ultrafast optical information processing [10].

Although soliton solutions of nonlinear wave equations may exist in higher dimensions, they are often unstable. There are only isolated reports of optical STSs: two-dimensional (2D) STSs have been observed in quadratic nonlinear media [11], and three-dimensional (3D) STSs were generated in an array of waveguides [12]. In each case the solitons were only stable for a few characteristic lengths, and there is still no report of 3D solitons in a homogeneous medium.

An alternative approach to STSs relies on dissipative processes. Systems that incorporate dissipation (in addition to diffractive, dispersive, and nonlinear phase modulations) have been shown theoretically to support stable solitons that are referred to as "dissipative optical bullets" [13–16]. While STSs in conservative systems require anomalous group-velocity dispersion, in dissipative systems stable STSs can also exist with normal dispersion. 2D spatial dissipative solitons in a cavity have been the subject of major interest recently [17]. One potential route to the experimental observation of a dissipative optical bullet would be an extension of this work to include localization in the time domain [17–19].

Lasers based on dielectric media doped with active ions may also be able to stabilize STSs. Temporal dissipative solitons have already been observed in both solid-state [20,21] and fiber [22] lasers. STSs would extend dissipative solitons to the two transverse dimensions. Theoretical work on models that are generally relevant to 3D dissipative systems strongly suggests that stable STSs are possible [13–16,18,19] and motivates further research to identify realistic experiments.

Here, we show through numerical modeling that stable STSs form in a solid-state laser with large self-focusing nonlinearity, significant normal group-velocity dispersion, and an unstable resonator (Fig. 1). To ensure that spatial localization is achieved primarily by optical nonlinearity, linear focusing elements must be removed from the cavity. In order to compensate for the diffraction in a realistic laser resonator, the total nonlinear phase shift must be significant, and this is accumulated in normal-dispersion material. Operation of the laser yields STSs that are stable over numerous propagation lengths. In addition to nearly static solutions, we observe qualitatively new phenomena, such as spontaneous spatiotemporal symmetry breaking and breathing limit cycles. As a secondary

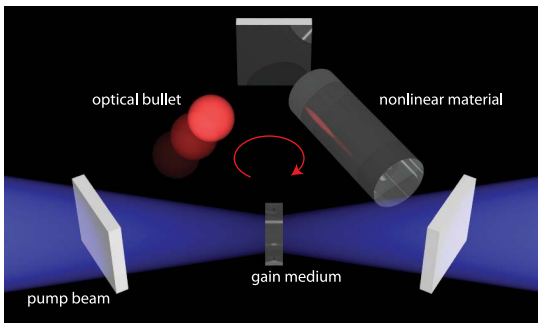

Fig. 1. Illustration of an STS laser.

point, in the future this type of laser may offer performance advances over current designs [23].

A mode-locked laser must include a gain medium and a saturable absorber. The gain medium also provides refractive nonlinearity, group-velocity dispersion, diffraction, and filtering by the gain spectrum. We assume flat cavity mirrors. In any real system with discrete optical elements, the majority of diffraction will occur from propagation in air. Intensity-dependent loss from a saturable absorber is needed to start a pulsed laser from noise and to stabilize the steady-state solutions. Initial simulations show that ordinary gain media could provide adequate nonlinear refraction with microjoule pulses, in which case chirped mirrors could provide the needed normal dispersion. The simplicity of this approach is attractive, but it will require a kilowatt-class pump laser. To achieve a practical design based on 100 W pump lasers, we must add a material with high refractive nonlinearity and normal group-velocity dispersion to the cavity. The STS laser therefore consists of a gain medium, air, a nonlinear material, a saturable absorber, and a spectral filter. The filter helps compensate the nonlinear phase in time, as is done in temporal dissipative-soliton lasers [22]. A ring cavity is assumed.

Numerical simulations are employed to find stable solutions to this system. The gain is modeled by a simple transfer function,

$$\frac{A_{\text{out}}(x,y,\omega)}{A_{\text{in}}(x,y,\omega)} = \exp\left(\frac{g_0}{1+\frac{E}{E_{\text{sat}}}} - 2\frac{x^4+y^4}{w_p^4} - \frac{\omega^2}{\Delta\omega^2}\right), \quad (1)$$

where g_0 is the small signal gain, E_{sat} is the saturation energy, w_p corresponds to the pump beam size (a super-Gaussian profile is chosen here to represent a multimode pump beam), and $\Delta\omega$ corresponds to the gain bandwidth. Pulse evolution in air and the nonlinear section are modeled with the standard nonlinear Schrodinger equation:

$$\frac{\partial A}{\partial z} = \frac{i}{2k_0}\left(\frac{\partial^2 A}{\partial x^2}+\frac{\partial^2 A}{\partial y^2}\right) - i\frac{\beta_2}{2}\frac{\partial^2 A}{\partial t^2} + i\gamma|A|^2 A, \quad (2)$$

where A is the slowly varying envelope at center frequency ω_0, t is time in a reference frame moving at the group velocity of the pulse, β_2 corresponds to the group velocity dispersion, $\gamma = \omega_0 n_2/c$ is the nonlinear coefficient, and $k_0 = \omega_0 n/c$. The saturable absorber is modeled with a transfer function $T = 1 - l_o/[1 + P(\tau)/P_{\text{sat}}]$, where l_o is the unsaturated loss, $P(\tau)$ is the instantaneous pulse power, and P_{sat} is the saturation power. Finally, the filter is Gaussian in the frequency domain. Simulations utilize a standard split-step Fourier transform technique. The initial condition is a low-intensity Gaussian pulse in three dimensions. Identification of converged (i.e., stable) solutions requires propagation through thousands of cavity round trips, until there is no noticeable change in the evolution of the solution. To dramatically reduce the computation time, simulations were initially run with only one transverse spatial dimension. These simulations identified the relevant parameter ranges, and 3D simulations were then performed over limited ranges of the parameters.

The search for stable solutions begins with the choice of roughly equal diffraction, dispersion, and nonlinear lengths, and we have confined our search to physically realizable parameter values. For example, stable solutions are found with a standard Yb:KGW crystal as the gain medium, SF11 glass as the nonlinear material, and a semiconductor saturable absorber mirror (the parameters are listed in the caption of Fig. 2). It is important to emphasize that the laser only reaches threshold if STSs form. The intracavity pulse energy smoothly converges to 1.5 μJ [Fig. 2(a)]. This corresponds to a 3 W/μm^2 peak intensity, 4 ps pulse duration, 9 nm bandwidth, and 250 μm beam waist (Fig. 2). The pulse is symmetric in space and time and exhibits spatial narrowing at the center of the pulse, which illustrates the strong role of nonlinearity in the spatial domain [Fig. 2(b)]. At the center of the beam, the temporal frequency spectrum has steep sides [Fig. 2(c)] and the pulse is highly chirped [Fig. 2(d)], as is the case for dissipative solitons in normal-dispersion fiber lasers [22]. At the center of the pulse, the spatial frequency spectrum has multiple sidebands [Fig. 2(e)] and >90% of the beam is well fitted by a hyperbolic-secant profile [Fig. 2(f)], as is the case for solitons in a cavity. Nonlinear focusing is primarily responsible

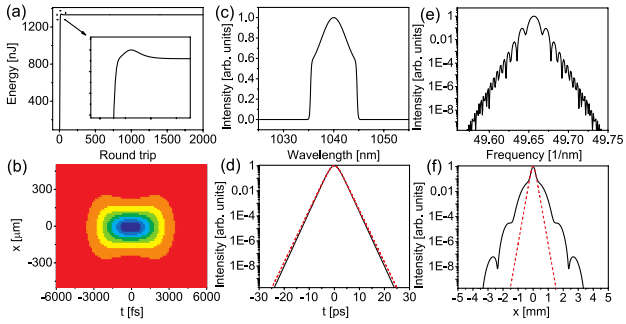

Fig. 2. Typical 2D simulation result: (a) energy convergence, (b) spatiotemporal color map of the pulse, (c) spectrum at the center of the beam, (d) temporal profile along with sech^2 fit (dashed line), (e) spatial-frequency spectrum at the center of the pulse, and (f) spatial profile along with sech^2 fit (dashed line). Parameters: the nonlinear material is 40 cm of SF11 glass ($n = 1.76$, $\beta_2 = 1520$ fs^2/cm [Schott glass], and $n_2 = 41 \times 10^{-8}$ μm^2/W [24]). The gain bandwidth is 40 nm, $E_{\text{sat}} = 600$ nJ, $w_p = 308$ μm (assuming 400 μm multimode pump fiber), there is 10 cm of air, the filter bandwidth is 12 nm, 2% power is coupled out, $l_o = 0.03$, and $P_{\text{sat}} = 51$ kW/μm (saturable absorber and output coupling parameters from Ref. [25]).

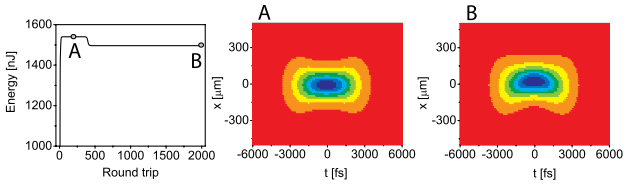

Fig. 3. Evolution of the pulse energy as a function of round trip around the oscillator and spatiotemporal profiles of the output at the indicated numbers of round trips.

for compensating diffraction, with a small (~1%) contribution from gain guiding. To summarize, diffraction and nonlinear phase balance as in solitons of the 1D nonlinear Schrodinger equation, while dispersion, spectral filtering, saturable absorption, and nonlinear phase balance as in 1D dissipative solitons. The pulse (beam) actually breathes by 20% (50%) as the pulse traverses the laser; the solution shown in Fig. 2 is the pulse after the saturable absorber.

With a slightly higher saturation energy of 650 nJ and all other parameters as above, a distinct change occurs in the solution. The pulse converges to a symmetric solution (middle panel of Fig. 3) similar to that in Fig. 2, but after several hundred round trips, this symmetry breaks and the solution finally converges to one which is asymmetric in space at every point in time. Seeding the simulation with the asymmetric pulse or its spatial mirror image shows that the asymmetric pulses are stable nodes of the system.

A further increase in the saturation energy, to 740 nJ, reveals a final solution, which is a long-period oscillation (Fig. 4 and Media 1. The symmetry, peak intensity, and spatiotemporal widths oscillate with a period of ~14 round trips (Fig. 4, left panel). This solution is a spatiotemporal limit cycle of the governing equation. Previously, oscillatory solutions were identified in a homogeneous model [18] and in the context of double bullet complexes [13,15].

To verify and refine the results quantitatively, 3D simulations were performed. With the same parameters as above and with a saturation energy of 450 nJ, a stable optical bullet converges (Fig. 5). Similar to the behavior in two dimensions (Fig. 3), symmetry breaking occurs after several hundred round trips [Fig. 5(a)], and the solution converges to a spatiotemporally asymmetric optical bullet [Fig. 5(b)]. The profiles in the x and y dimensions are nearly identical [Fig. 5(c)] and correspond to the symmetry of the spatial effects. The resulting three-dimensionally localized wave packet resembles a bean in an isointensity plot [Fig. 5(d)].

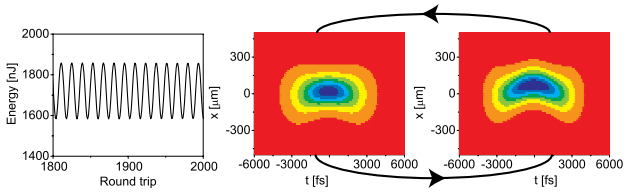

Fig. 4. Evolution of the energy as a function of round trip for the spatiotemporal limit cycle, with representative spatiotemporal profiles of the output field at the half-periods of the oscillation (Media 1).

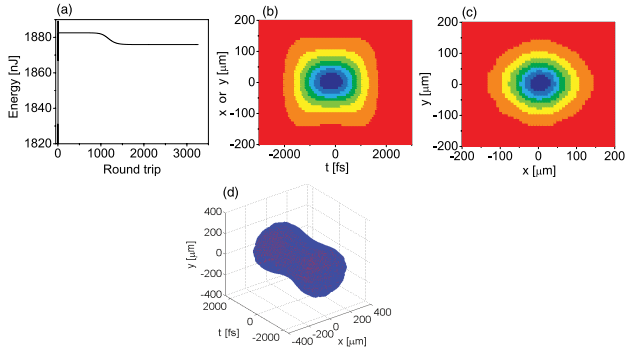

Fig. 5. Results of 3D simulations. (a) Evolution of the energy as a function of round trip, (b) spatiotemporal profile at $x = 0$ or $y = 0$, (c) beam at the center of the pulse, and (d) isointensity surface of the bullet at 5% of the peak intensity.

As the nonlinear processes must create dissipative-soliton solutions that are stable against perturbations, a primary consideration in the design of an STS laser is the choice of nonlinear material. The refractive nonlinearity must balance the effects of diffraction. However, because the nonlinear and diffractive segments are in separate locations in the cavity, there is an upper limit to the nonlinear phase that can be fully compensated. Guided by the numerical results, we assume that the ideal accumulated nonlinear phase shift (and thus the diffractive phase) will be π. The nonlinear phase is determined by the intensity, nonlinear index, and material length. The intensity is determined by the pump power, the loss of the material (including effective loss in the cavity due to wavefront distortions), the nonlinear loss of the material, the loss of the cavity, the gain medium, and the length of the cavity. Many of these variables are coupled. The relevant equations can be readily solved. While it is difficult to achieve the needed combination of length and loss with ordinary glasses such as fused silica, the requirements become more reasonable as the nonlinear index increases.

The beam size and the length of the air section also have significant influence on the design. The nonlinear material determines the size of the beam in the cavity (that is, total diffraction is related to the length of propagation through the material and the amount of nonlinear phase available to compensate for this diffraction, as well as the size of the beam). To study STS formation, it will be advantageous to minimize the effect of any aperture in the cavity by reducing the beam size. Therefore, it will be preferable to use the shorter, high-index materials for the smaller beam sizes that result. The air section should be as short as practically possible to minimize diffraction and therefore reduce the requirements on the nonlinear material. With care this could probably be reduced, which in turn would reduce the length of the nonlinear material.

A final practical issue will be the stringent requirements on the homogeneity of materials that are placed inside a low-loss laser cavity. We constructed a femtosecond Yb:KGW laser [25] as a test bed for candidate nonlinear materials. The internal transmittance of 10 cm of SF11 glass is >99% at the operating wavelength. However, we find that insertion of 50 cm of SF11 in the cavity introduces an effective loss of ~25%,

which arises from wavefront distortion. It will be important to find the appropriate lengths of laser-quality nonlinear materials. It may be more practical, however, to compensate for imperfect materials by instead relying on higher pump powers. As an example, a short segment of chalcogenide glass with high pump power is both theoretically suitable and seems to be within current capabilities, albeit with the possible challenges of larger material absorption and photodarkening.

Alternative embodiments of the STS laser are worth noting. For example, the narrow gain bandwidth of Yb:YAG will eliminate the need for a filter, and the larger pump beam in a thin-disk geometry will avoid aperture effects. In such a system STSs could be stable with a dense flint material and several hundred watts of pump power. Ultimately, it should be possible to generate femtosecond pulses with microjoule energies, which will be attractive for some applications.

In conclusion, we have demonstrated the existence and stability of STSs in a realistic model of a solid-state laser. Key to the design is recognition of the role of normal dispersion in stabilizing the localized wave packet. Numerical simulations reveal unique features at high pulse energies, such as spontaneous spatiotemporal symmetry breaking and breathing limit cycles. Experimental realization of an STS laser will be challenging but seems to be technologically feasible.

FUNDING INFORMATION

National Science Foundation (NSF) (ECCS-1306035, PHY-0653482).

ACKNOWLEDGMENTS

The authors thank Logan Wright for valuable discussions.

REFERENCES

1. J. S. Russell, *Report of the Fourteenth Meeting of the British Association for the Advancement of Science* (1844), pp. 311–390.
2. A. R. Osborne and T. L. Burch, Science **208**, 451 (1980).
3. L. F. Mollenauer, R. H. Stolen, and J. P. Gordon, Phys. Rev. Lett. **45**, 1095 (1980).
4. N. Zabusky and M. Kruskal, Phys. Rev. Lett. **15**, 240 (1965).
5. L. Khaykovich, F. Schreck, G. Ferrari, T. Bourdel, J. Cubizolles, L. D. Carr, Y. Castin, and C. Salomon, Science **296**, 1290 (2002).
6. S. O. Demokritov, A. A. Serga, V. E. Demidov, B. Hillebrands, M. P. Kostylev, and B. A. Kalinikos, Nature **426**, 159 (2003).
7. B. A. Malomed, D. Mihalache, F. Wise, and L. Torner, J. Opt. B **7**, R53 (2005).
8. R. Chiao, E. Garmire, and C. Townes, Phys. Rev. Lett. **13**, 479 (1964).
9. Y. Silberberg, Opt. Lett. **15**, 1282 (1990).
10. R. McLeod, K. Wagner, and S. Blair, Phys. Rev. A **52**, 3254 (1995).
11. X. Liu, L. Qian, and F. Wise, Phys. Rev. Lett. **82**, 4631 (1999).
12. S. Minardi, F. Eilenberger, Y. V. Kartashov, A. Szameit, U. Röpke, J. Kobelke, K. Schuster, H. Bartelt, S. Nolte, L. Torner, F. Lederer, A. Tünnermann, and T. Pertsch, Phys. Rev. Lett. **105**, 263901 (2010).
13. N. Akhmediev, J. M. Soto-Crespo, and P. Grelu, Chaos **17**, 037112 (2007).
14. J. M. Soto-Crespo, P. Grelu, and N. Akhmediev, Opt. Express **14**, 4013 (2006).
15. J. M. Soto-Crespo, N. Akhmediev, and P. Grelu, Phys. Rev. E **74**, 46612 (2006).
16. P. Grelu, J. M. Soto-Crespo, and N. Akhmediev, Opt. Express **13**, 9352 (2005).
17. T. Ackemann, W. J. Firth, and G. Oppo, Adv. At. Mol. Opt. Phys. **57**, 323 (2009).
18. A. G. Vladimirov, S. V. Fedorov, N. A. Kaliteevskii, G. V. Khodova, and N. N. Rosanov, J. Opt. B **1**, 101 (1999).
19. M. Brambilla, T. Maggipinto, G. Patera, and L. Columbo, Phys. Rev. Lett. **93**, 203901 (2004).
20. B. Proctor, E. Westwig, and F. Wise, Opt. Lett. **18**, 1654 (1993).
21. S. Naumov, A. Fernandez, R. Graf, P. Dombi, F. Krausz, and A. Apolonski, New J. Phys. **7**, 216 (2005).
22. W. H. Renninger, A. Chong, and F. W. Wise, Phys. Rev. A **77**, 23814 (2008).
23. W. H. Renninger and F. W. Wise, "Fundamental limits to mode-locked lasers: toward terawatt peak powers," IEEE J. Sel. Top. Quantum Electron., doi:10.1109/JSTQE.2014.2329936 (to be published).
24. E. M. Vogel, M. J. Weber, and D. M. Krol, Phys. Chem. Glasses **32**, 231 (1991).
25. J. A. Berger, M. J. Greco, and W. A. Schroeder, Opt. Express **16**, 8629 (2008).

Research Article Vol. 1, No. 2 / August 2014 / Optica 105

Deep tissue imaging using spectroscopic analysis of multiply scattered light

THOMAS E. MATTHEWS,[1] MANUEL MEDINA,[2] JASON R. MAHER,[1] HOWARD LEVINSON,[2] WILLIAM J. BROWN,[1] AND ADAM WAX[1,*]

[1]Department of Biomedical Engineering, Duke University, Durham, North Carolina 27708, USA

[2]Department of Surgery, Duke University Medical Center, Durham, North Carolina 27708, USA

*Corresponding author: a.wax@duke.edu

Received 23 April 2014; revised 25 June 2014; accepted 26 June 2014 (Doc. ID 210734); published 13 August 2014

Scattering limits the penetration depth of most optical imaging techniques. Efforts to overcome this limitation often require complex optical or computational schemes. We have developed a new method of assessing tissue properties based on spectroscopic analysis of multiply scattered light. The technique, multispectral multiple-scattering low-coherence interferometry (ms2/LCI), uses coherence and spatial gating to produce images of tissue optical properties up to 9 mm deep, with millimeter-scale resolution. The capabilities of ms2/LCI are demonstrated using tissue phantoms composed of chicken breast. Discrimination of diseased and healthy tissues is shown through imaging and analysis of burns in *ex vivo* human skin samples. Our technique may provide a powerful way to assess burn depth and progression in sensitive, burned tissues where physical contact is undesirable.

OCIS codes: (290.4210) Multiple scattering; (170.6510) Spectroscopy, tissue diagnostics; (110.1650) Coherence imaging.

http://dx.doi.org/10.1364/OPTICA.1.000105

1. INTRODUCTION

Scattering is the dominant mechanism of light transport in tissue. It limits the penetration depth of most optical imaging techniques by attenuating the incident light while simultaneously burying it beneath a diffuse background signal. Techniques that image with photons that have only interacted a single time with tissue such as confocal microscopy and optical coherence tomography must have a way to separate these photons from the diffuse background. Confocal microscopy uses an aperture as a spatial filter to selectively detect light arising from a localized region and reject out-of-focus light. This approach is effective but is limited to roughly three scattering mean free paths (MFPs), defined as the average distance needed for light to experience one scattering event, typically about 150–200 μm in tissue depending on the tissue type and wavelength of illumination, in this case 800 nm [1]. Optical coherence tomography (OCT) and other low-coherence interferometry (LCI) methods use coherence gating to selectively detect photons by optical path length. OCT uses near-IR light and is effective in selecting singly scattered photons up to about 27 scattering MFPs or about 1–2 mm in tissue [2].

There have been several recent efforts to extend optical imaging beyond this few-millimeter depth. These include photoacoustic tomography, which detects ultrasonic signatures of absorptive features up to a few centimeters deep [3] but does not provide scattering contrast. Further, the need for acoustic impedance matching requires contact with the tissue, which may not be feasible in some clinical applications. Another approach is to shape the wavefront of light to focus deep within tissue using ultrasound [4] or speckle variance [5] encoding. These approaches offer great potential for deep tissue imaging but may be limited by the need for complex optical and computational schemes.

Recently, we have developed an alternative method for deep tissue optical imaging based on exploiting forward-scattered light. Multiple-scattering low-coherence interferometry (ms/LCI) uses coherence gating to restrict photon path length with spatial gating to localize photon paths to achieve imaging up to 90 scattering MFPs with millimeter resolution in tissue

2334-2536/14/020105-07$15/0$15.00

phantoms [6]. Further development of the method shifted detection from the time domain to the frequency domain [7], which greatly reduced data acquisition times while incorporating multispectral capabilities, covering a bandwidth of 60 nm centered at 633 nm. The multispectral multiple-scattering LCI (ms2/LCI) system was able to detect an absorptive feature at 90 MFPs (9.5 mm) within a tissue-like phantom.

In this article, we now present the first application of ms2/LCI to deep tissue imaging and analysis. Imaging is demonstrated by detecting a reflective target through 8.8 mm of chicken breast. Absorptive contrast is shown by detecting the spectroscopic signature of a dye-filled capillary through 6 mm of chicken breast using a purely biological feature to generate scattering contrast. Finally, the potential clinical utility of ms2/LCI is established by imaging scattering changes due to thermal damage in *ex vivo* human tissues at depths of several millimeters. Spectroscopic analysis of these images shows a potentially powerful way to assess burn progression.

2. EXPERIMENTAL SETUP

The tissue imaging experiments presented here use the Fourier domain scheme for ms2/LCI described previously [7]. Briefly, light from a supercontinuum source (Fianium SC-450) is filtered and split into two components, an input to the sample and a reference. The input to the sample was a 6 mm diameter beam focused using a 100 mm lens but offset from the optical axis. The result is light incident at an angle of approximately 4° relative to normal with an approximately 14 μm diameter spot at the focus. This corresponds to an effective input NA of 0.03 and a Rayleigh range of 0.9 mm. The schematic in Fig. 1 shows this arrangement along with a projected detection path also offset from the optical axis by the same distance that intersects the illumination beam within a focal zone several millimeters beneath the sample surface. The arrangement of separate illumination and detection apertures allows selective detection of light that has passed through the focal zone. Light that has been forward scattered en route to the focal zone or on the return path retains useful information about the sample. Diffusely scattered light is not efficiently collected by this geometry, and thus it is suppressed in the detected signal.

The ms2/LCI scheme uses a custom-built spectrometer with a spectral resolution of 0.014 nm, corresponding to a maximum detection range of $z_{max} = 5.6$ mm. An enhanced depth imaging approach was used [8] where the zero path delay point ($z = 0$), which offers the highest response for spectral detection, was set at the deepest sample feature. The coherence length that can be achieved with this scheme is 2.4 μm, but the effective axial resolution achieved with the ms/LCI geometry is typically 100 μm.

In the previous time-domain implementation of ms/LCI, long integration times were used to enable a high dynamic range. With the Fourier domain implementation, short sensor integration times must be used to avoid phase washout. The maximum A-scan rate allowed by the sensor in this scheme is 40 kHz. However, to enable a high enough SNR to obtain deep tissue imaging, multiple A-scans are averaged at a slightly lower rate. For each 3 s acquisition, approximately 75,000 A-scans are averaged to produce a 144 dB SNR. A digital lock-in scheme was also employed to correct for any baseline drift during this acquisition time [7].

Spectroscopic data were obtained from the A-scans using short-time Fourier transforms (STFTs), which can degrade depth resolution. By using the dual-window method [9], where spectra are processed individually using two windows

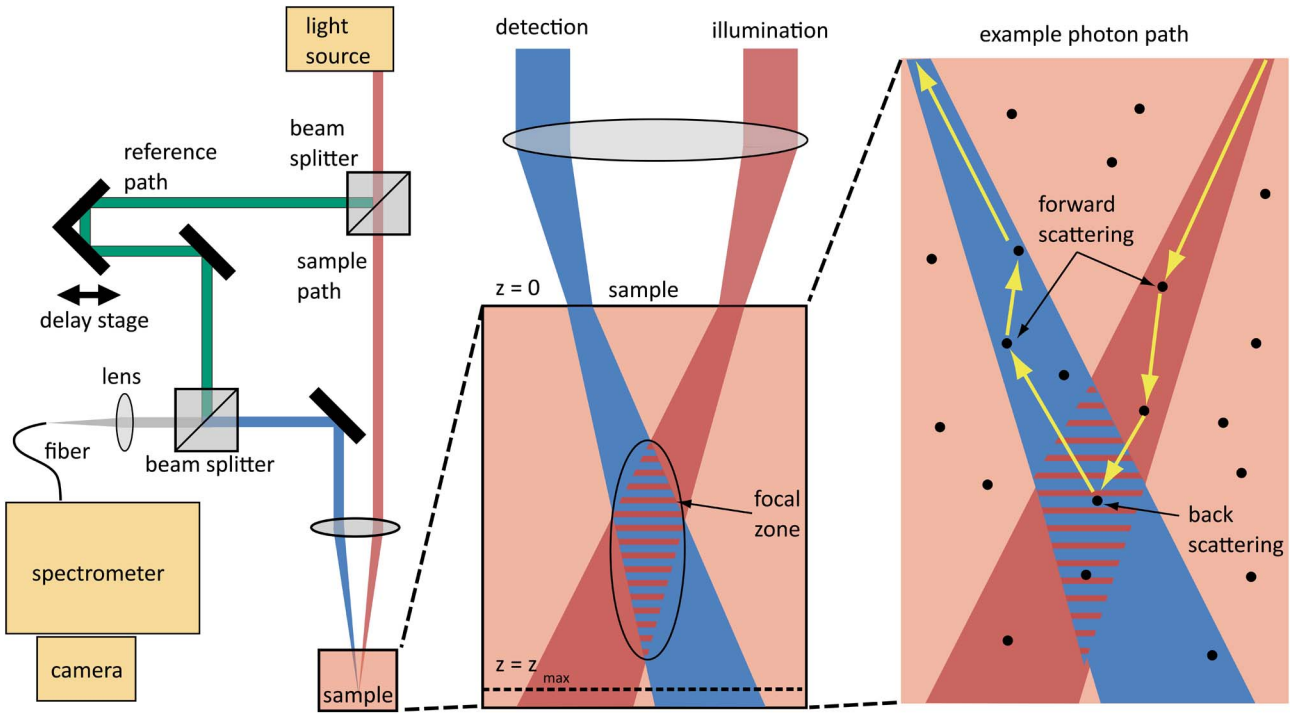

Fig. 1. Diagram of ms2/LCI scheme, including detail of focal zone and example photon path.

of 1.25 and 40 nm, this effect is mitigated. The corresponding depth resolution is defined by the wide window to be 5 μm, and the effective spectral resolution is defined by the narrow window. The STFTs are implemented in real time using GPU processing, significantly reducing the amount of time needed for signal analysis.

3. TISSUE IMAGING

To demonstrate the penetration depth of the technique, images of a technical target, in this case a mirrored surface, were acquired through various thicknesses of chicken breast by mechanically scanning the sample between A-scans. Figure 2 shows the geometry of the imaging sample. Chicken breast has a mean free scattering path of 43 μm [10]. Thus, the imaging data, acquired through tissue up to 8.8 mm thick, illustrate a penetration depth of greater than 200 MFPs (Fig. 3). Because light scattering in chicken breast is highly anisotropic, the *transport* MFP of the tissue (i.e., the length over which the direction of photon propagation is randomized) is one to two orders of magnitude larger than the scattering MFP and varies between approximately 1.25 and 2.5 mm [10,11].

Given that the total depth range of a single ms2/LCI acquisition is 6.8 mm, two frames were acquired at different depths to create the image in Fig. 3. Each frame required approximately 5 min to acquire. The first image at the top half of Fig. 3 shows the chicken breast surface and extends up to 5 mm deep across a range of 13 mm in the lateral direction. The second image at the bottom half was obtained by adjusting the selected depth range using the delay stage shown in Fig. 1 to access a deeper penetration depth of up to 8.8 mm. As the chicken breast section gets thicker from left to right, the signal from the mirror (top panel in Fig. 3) is seen to broaden in depth profile. The bottom panel shows the depth profiles at 0, 6, and 13 mm, illustrating how the depth profile broadens from 0.125 to 0.6 to >1 mm. A couple of interesting features warrant discussion. First, the spectral domain method exhibits artifacts due to aliasing, often termed the "complex conjugate." That is, because each depth is encoded by a spectral oscillation frequency, the approach cannot distinguish between positive and negative frequencies. Since the reflection from the mirror is a strong signal, the complex conjugate artifact is apparent in the top half of Fig. 3 but is not a significant confounding influence in subsequent tissue images below. We point out that several methods have been developed for eliminating this artifact that could be employed if this were found to limit imaging utility. Second, since the chicken breast has a higher

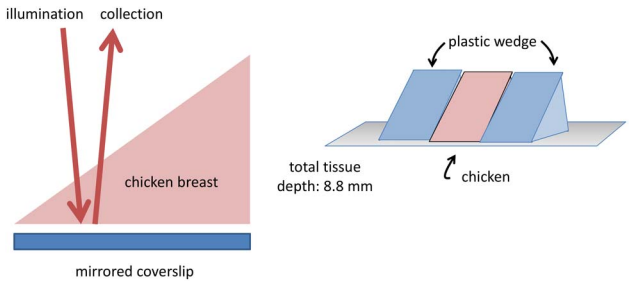

Fig. 2. Imaging geometry for chicken breast experiments.

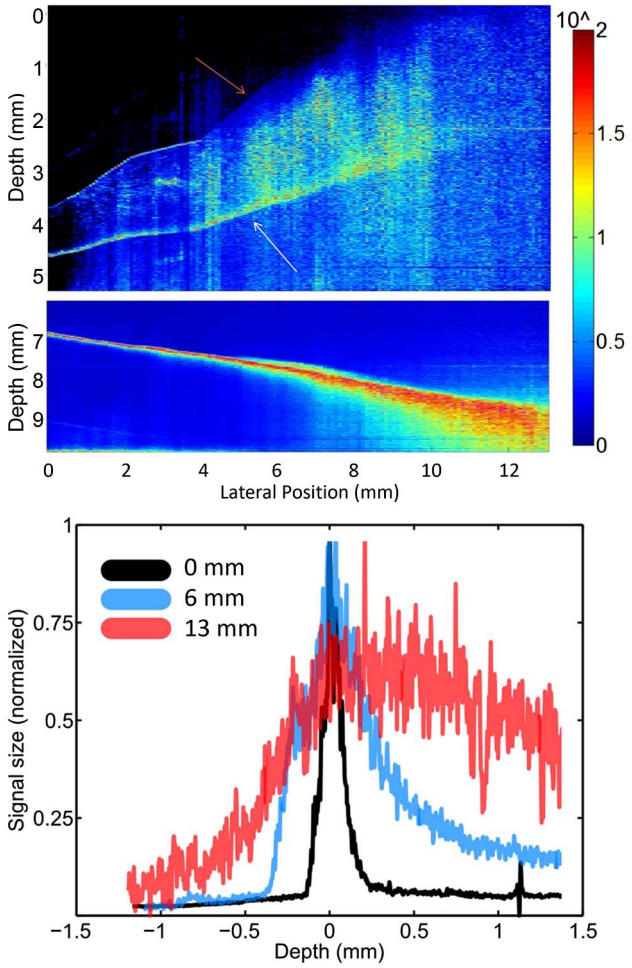

Fig. 3. Top: ms2/LCI imaging of a mirror sample through up to 8.8 mm thick chicken breast. The depth range of the technique is 5.6 mm, so two data acquisitions at different depths are shown here. The red arrow shows the surface of chicken breast, and the white arrow shows the complex conjugate artifact of a strong signal from the mirror that is seen below. Bottom: Depth profiles from the lower image showing depth profiles at 0, 6, and 13 mm lateral positions.

refractive index than the surrounding medium (air), the apparent depth of the surface appears to increase as the thickness of the chicken breast increases. Thus on the left (0 mm lateral position), the mirror appears at a depth position of 7 mm, yet on the right (13 mm lateral position), the mirror appears at a depth of 9 mm, even though the mirror is oriented perpendicular to the optical axis. The total optical depth is equal to the physical thickness times the refractive index such that for the largest physical thickness of 8.8 mm, the optical thickness appears to be >13 mm. This effect could be corrected using knowledge of the thickness and refractive index of tissue layers. However, when imaging tissue properties of substantially planar layers, it may not be strictly necessary to identify the physical depth of a particular feature for diagnostic utility.

The inclusion of spectroscopic information greatly increases the utility of the ms2/LCI technique for tissue diagnostics. Figure 4 shows an image of a tissue phantom as an example of the ability to distinguish tissue types using spectral

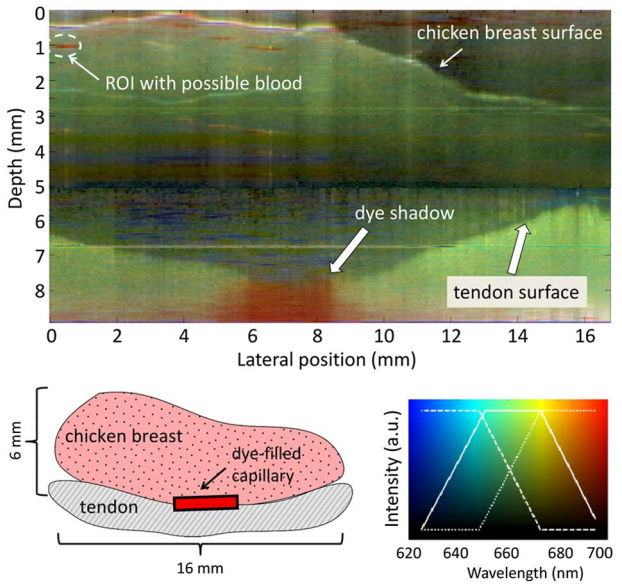

Fig. 4. Top: ms2/LCI imaging of chicken breast phantom with spectroscopic contrast. False coloring provided by mapping the spectral content to the provided color scheme appears in the bottom right panel. The chicken breast surface is evident at the top, while the tendon is visible at the bottom. The schematic on the bottom left shows the physical arrangement of the phantom components. Spectroscopic contrast reveals the presence of a dye-filled capillary by the apparent color shift. Detailed examination of the spectra (see Fig. 5) shows the dye absorption and that of the region of interest (ROI).

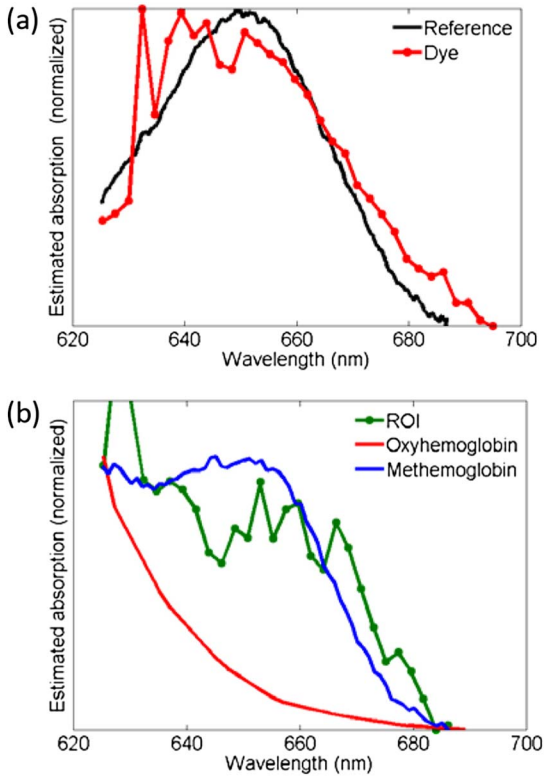

Fig. 5. Spectral detail for image in Fig. 4. (a) Recovered absoprtion spectrum of dye as compared to a reference measurement, (b) absorption spectrum of ROI compared to those of oxyhemoglobin and methemoglobin.

information. A schematic of the phantom, consisting of a piece of chicken breast atop a segment of tendon with a dye-filled capillary inserted in between is shown beneath in the bottom left panel. The dye used here is undiluted green food coloring (Kroger Private Label Product) contained within a glass capillary (200 μm i.d., 500 μm o.d.). In order to easily present the spectroscopic information, we created a false color image based on spectral subband coding of the spectral information, as used previously in spectroscopic OCT [12]. The intensity at each wavelength contributed to the weight of the RGB channels as shown by the spectral windows in the lower right panel of Fig. 4, with the bandwidth from 620 to 660 nm shown as blue (dashed line), 640–680 nm as green (solid line), and 660–700 nm as red (dotted line). The underlying coloring in this figure shows the expected coloring for a given spectral composition. As in Fig. 3, this image consists of two panels, the topmost panel, which shows the surface of the chicken breast, and the bottom panel, which shows the tendon and the dye capillary. The horizontal line at 4 mm depth indicates the point where the two panels were joined. A second horizontal line, visible at 2.2 mm depth, is due to incomplete subtraction of a common path artifact, i.e., fixed pattern noise from correlations in the spectral data. The signal from the chicken breast decreases with increasing depth until a sharp contrast is seen where the tendon is visible from the increased scattering contrast. The presence of the dye capillary can be detected by the spectroscopic features. The spectroscopic shadow of the capillary is colored red, since the shorter wavelengths have been absorbed.

Figure 5 shows the recovered spectrum for the light returned from beneath the dye-filled capillary as compared to that from the tendon alone. By normalizing to the source spectrum, the absorption of the dye can be obtained [Fig. 5(a)]. Compared to a reference measurement of the dye absorption, good agreement is seen ($R^2 = 0.8219$). Another interesting feature in Fig. 4 is the presence of red spots, which are visible near the tissue surface. The spectrum for the region of interest (ROI) shows a loss of low wavelengths (620–660 nm) compared to light returned from points at similar depths in the tissue. The absorption spectrum for this region was computed [Fig. 5(b)] but does not show good agreement with oxyhemoglobin, producing a negative R^2 value, indicating that the data would be fit better by a horizontal line than the oxyhemoglobin spectrum. Instead, the spectrum shows better agreement with that of methemoglobin ($R^2 = 0.6839$), the variant of hemoglobin usually found in blood stains and consistent with the red-brown spots sometimes observed on the surface of chicken breast samples.

To illustrate the applicability of ms2/LCI imaging for assessing tissue health status, several samples of *ex vivo* burned human skin were examined. In the first example (Fig. 6), the amplitude of the ms2/LCI signal is presented in a false color scale, with red representing the most intense and deep blue the least intense. This simulated burn was created by heating a brass rod and then applying it to the *ex vivo* skin sample for a fixed duration [13,14]. Figure 6(a) simulates a deep, second-degree burn where the rod was heated to 100°C and

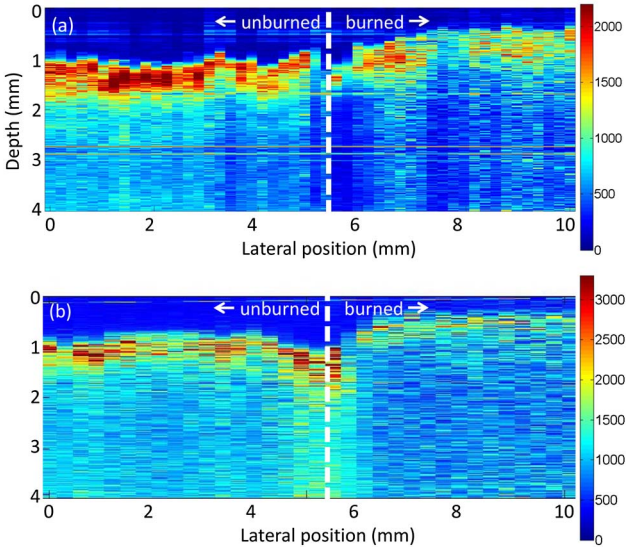

Fig. 6. Intensity-only ms2/LCI imaging of burned *ex vivo* human skin. (a) Deep second- degree burn created by applying a brass rod heated to 100°C for 30 s, (b) shallow second-degree burn created by applying a brass rod heated to 80°C for 20 s. Both examples show decreased scattering associated with the burned section compared to the unburned section in both the epidermis, the topmost 1 mm of the tissue, and the dermis, at deeper layers. The contrast is less apparent in the shallow second-degree burn.

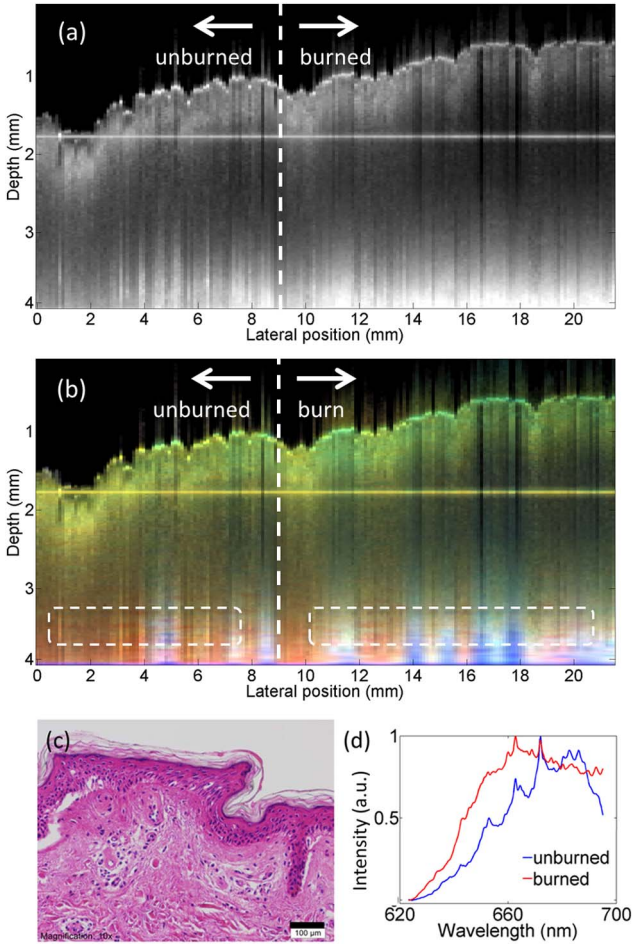

Fig. 7. False coloring of ms2/LCI images of burned *ex vivo* human tissues. (a) Intensity-only image of a deep second-degree burn (right) compared to unburned tissue (left). The epidermal layer shows changes in the signal at the surface, with a more organized structure at the surface of the unburned than the burned tissue. (b) False colored ms2/LCI image based on spectral content between 620 and 700 nm (same color scheme as in Fig. 4), (c) histological image of the same burned tissue at 10× magnification; (d) raw spectral data taken at the base of the dermis [dotted lines in (b)] show clear changes between the burned and unburned tissue. The increased signal intensity at lower wavelengths agrees with physiological changes due to burn.

applied for 30 s. The ms2/LCI image shows differences in the signal from the epidermis at the topmost 1 mm of the tissue, with a greater signal seen for the unburned tissue. The altered collagen architecture associated with the burn is also visible in this image. It appears as a decrease in signal in the dermis for deeper portions of the burned tissue. The decreased signal seen for the collagen is consistent with previous examples of *in vitro* collagen samples also exposed to a heated metal rod (data unpublished). Figure 6(b) shows an example of less severely burned sample. In this case, the rod was heated to 80°C and applied for only 20 s. The result was a shallow dermal second-degree burn. Here the signal from the epidermis again shows differences between unburned and burned, but the contrast is not as distinct as in the deep second-degree burn. Likewise, the collagen signal shows some difference between burned and unburned, yet it is not as apparent as in the case of the deep second-degree burn. Further clinical study is needed to assess if this amplitude-only image can be used as a clinical diagnostic method. However, the ability to visually discern the effects of thermal damage that correlate with burn stage is a promising indication of the utility of ms2/LCI.

Figure 7 shows another example of ms2/LCI imaging of *ex vivo* burned human skin at a higher resolution. While Fig. 6 presented B-scan images composed by sampling three A-scans per millimeter in the lateral direction, Fig. 7(a) uses the highest resolution of the ms2/LCI system to sample eight A-scans per millimeter. As with the previous example, the *ex vivo* human tissue samples were prepared by applying a brass rod heated to 80°C for 30 s. This protocol produced a deep second-degree burn, with the corresponding histology shown in Fig. 7(c). Evidence of the burn is apparent by the vacuolization in the epidermis, pyknosis of the cell nuclei, and alteration of the collagen structure. The image in Fig. 7(c) is at 10× magnification and thus only represents a small portion of the tissue region presented in Fig. 7(a), which extends for over 20 mm in the lateral direction. The intensity-only image in black and white shows some distinction between the unburned (left) and burned (right) tissue segments based on only the signal intensity, similar to the results in Fig. 6. In this representation, the largest difference is the lack of a distinct high-intensity layer in the epidermal surface of the burned region (right). Additionally, a decrease in the signal from collagen in the dermis can also be seen, similar to the other burned tissue images.

Upon incorporating spectroscopic information, the distinctions in tissue health become more apparent. Figure 7(b) shows a false colored ms2/LCI image created by the same coloring scheme as shown in Fig. 4 where the spectral content

is segmented into three bands and a red–green–blue (RGB) color scheme is used to indicate the spectral content between 620 and 700 nm. Figure 7(d) shows the detailed spectra for the burned and unburned sections for a depth of 3–4 mm at the base of the dermal layer. At this depth, there is significantly more short-wavelength spectral content for the burned tissue than the unburned tissue, which appears as regions of blue coloring, alternating with the reddish pink seen mostly for the unburned tissue. We investigated the spectral differences by dividing the spectral data by the source spectrum and then fit the result to a power law of the form $A\,\lambda^{-b}$, where λ is the wavelength. The exponent b is seen to provide distinction between the burned and unburned tissue, with the exponent increasing from $b = 14.7 \pm 2.5$ (unburned) to $b = 30.7 \pm 2.4$ (burned), a significant change. We note that the power law exponents are significantly larger than those found in the literature [15]. This departure suggests that the changes may not be entirely due to scattering and that absorption may also play a role here. While further investigation is needed to separate the interplay of these two factors in the ms2/LCI signal, the sharp difference may provide a simple, empirical method of discrimination.

For comparison, Fig. 8(a) shows a false colored ms2/LCI scan of a superficial first-degree burn, achieved by applying a brass rod heated to 80°C for 3 s. In this image both the left and right sides show similar spectral content. As expected for this shallow burn, the false coloring at the transition from the dermis to the adipose tissue beneath does not show the blue coloring. The spectra for burned and unburned regions show little to no difference [Fig. 8(c)]. There is no apparent change in the signal intensity of the bright epidermis between regions. Histology also shows little change in the tissue with only a small amount of inflammation and minor alterations to collagen architecture seen at the dermal–epidermal junction. However, the superficial dermis is not damaged.

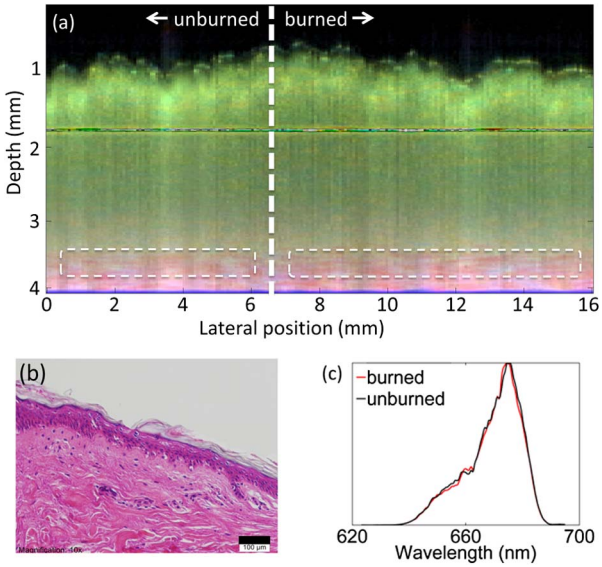

Fig. 8. ms/LCI imaging of burned *ex vivo* human tissues. (a) False colored ms2/LCI image of a superficial first-degree burn (right) compared to unburned tissue (left), with the same color scheme as in Fig. 4. Little change is seen in signal intensity or spectral content. (b) Histological image of the same burned tissue at 10× magnification; (c) the raw spectra from the base of the dermis [dotted lines in (a)] show no changes between burned and unburned tissue.

4. DISCUSSION

The data presented here demonstrate that ms2/LCI offers truly unique capabilities in tissue imaging. While existing optical imaging techniques cannot penetrate more than a millimeter or two with high resolution, the ms2/LCI technique shows a several-millimeter penetration depth. Approaches such as laminar optical tomography (LOT) have sought to image dermal lesions with a penetration of 1–2 mm [16], and like ms2/LCI, LOT can obtain multispectral measurements with a single acquisition [17]. Newer optical techniques that are in development [3–5] offer potential for even deeper tissue imaging, but they have their own limitations. In particular, none of these can image scattering-based contrast and instead must rely on fluorescence or absorption. For scenarios where there is a large scattering homogeneity to provide strong contrast, such as the chicken breast examples shown here, the potential exists to image as far as 9 mm deep with ms2/LCI. Many potential applications can be envisioned where scattering contrast in tissue is useful to this depth. The demonstration that endogenous sources such as bone or tendon can likewise provide the scattering contrast needed for achieving such depths points to further targeted applications.

Inclusion of spectroscopic information further extends the utility of ms2/LCI for tissue diagnostics. The ability to spectroscopically assess changes in scattering and absorption is an essential component of optical diagnostics. While spectroscopic contrast in OCT is not necessarily a new development, with the first experiments presented years ago [18,19], most spectroscopic OCT studies have focused on absorption signatures [20–24] often generated by exogenous contrast agents such as gold nanoparticles [25–27] and near-IR dyes [28,29]. Our group has used scattering contrast previously but sought to obtain single particle signatures [30,31] in an effort to assess early cancerous changes in superficial epithelium [32]. Thus, the work here is among the first to detect spectroscopic scattering changes to discriminate tissue types.

The data for detecting burns here are preliminary but demonstrate that the ms2/LCI technique has the potential to be used to distinguish between burned and unburned human tissues. The spectroscopic information, obtained from up to several millimeters deep, provides unique characterization of tissues and could address an unmet clinical need. In the United States, there are over 2 million burns reported each year, and in the military ~5%–20% of injuries are thermal related [33]. Burn injuries are estimated to cost ~$7.5 billion/year [34]. Currently, clinical judgment of burn depth is only ~70% accurate [35]. The ms2/LCI imaging technique has the potential to overcome existing hurdles in burn assessment, since it can image skin properties up to several millimeters deep in a noncontact modality. In contrast, photoacoustic imaging typically requires acoustic impedance matching through physical contact, an arrangement that may not lend itself to imaging of sensitive, burned tissues.

5. CONCLUSION

We have presented a new application of ms2/LCI for deep tissue imaging. Imaging depths up to nearly 1 cm were demonstrated in technical tissue samples. Significantly, the approach can incorporate spectroscopic contrast of absorptive and scattering features, although further work is needed to separate the influences of these two mechanisms. Potential application in assessing burn depth has been demonstrated with spectroscopic contrast from deep tissues (3–4 mm), offering a potential solution to an unmet clinical need.

FUNDING INFORMATION

National Science Foundation (NSF) (CBET 1133222).

REFERENCES

1. C. L. Smithpeter, A. K. Dunn, A. J. Welch, and R. Richards-Kortum, "Penetration depth limits of in vivo confocal reflectance imaging," Appl. Opt. **37**, 2749–2754 (1998).
2. M. R. Hee, J. A. Izatt, J. M. Jacobson, J. G. Fujimoto, and E. A. Swanson, "Femtosecond transillumination optical coherence tomography," Opt. Lett. **18**, 950–952 (1993).
3. L. V. Wang, "Multiscale photoacoustic microscopy and computed tomography," Nat. Photonics **3**, 503–509 (2009).
4. X. Xu, H. Liu, and L. V. Wang, "Time-reversed ultrasonically encoded optical focusing into scattering media," Nat. Photonics **5**, 154–157 (2011).
5. B. Judkewitz, Y. M. Wang, R. Horstmeyer, A. Mathy, and C. Yang, "Speckle-scale focusing in the diffusive regime with time reversal of variance-encoded light (TROVE)," Nat. Photonics **7**, 300–305 (2013).
6. M. G. Giacomelli and A. Wax, "Imaging beyond the ballistic limit in coherence imaging using multiply scattered light," Opt. Express **19**, 4268–4279 (2011).
7. T. E. Matthews, M. G. Giacomelli, W. J. Brown, and A. Wax, "Fourier domain multispectral multiple scattering low coherence interferometry," Appl. Opt. **52**, 8220–8228 (2013).
8. R. F. Spaide, H. Koizumi, and M. C. Pozonni, "Enhanced depth imaging spectral-domain optical coherence tomography," Am. J. Ophthalmol. **146**, 496–500 (2008).
9. F. Robles, R. N. Graf, and A. Wax, "Dual window method for processing spectroscopic optical coherence tomography signals with simultaneously high spectral and temporal resolution," Opt. Express **17**, 6799–6812 (2009).
10. W. F. Cheong, S. A. Prahl, and A. J. Welch, "A review of the optical properties of biological tissues," IEEE J. Quantum Electron. **26**, 2166–2185 (1990).
11. B. B. Das, K. M. Yoo, and R. R. Alfano, "Ultrafast time-gated imaging in thick tissues—a step toward optical mammography," Opt. Lett. **18**, 1092–1094 (1993).
12. C. Xu, C. Vinegoni, T. S. Ralston, W. Luo, W. Tan, and S. A. Boppart, "Spectroscopic spectral-domain optical coherence microscopy," Opt. Lett. **31**, 1079–1081 (2006).
13. A. J. Singer, D. Hirth, S. A. McClain, L. Crawford, F. Lin, and R. A. Clark, "Validation of a vertical progression porcine burn model," J. Burn Care Res. **32**, 638–646 (2011).
14. N. A. Coolen, M. Vlig, A. J. Van Den Bogaerdt, E. Middelkoop, and M. M. Ulrich, "Development of an in vitro burn wound model," Wound Repair Regen. **16**, 559–567 (2008).
15. V. V. Tuchin and V. Tuchin, *Tissue Optics: Light Scattering Methods and Instruments for Medical Diagnosis* (SPIE, 2007), Vol. **PM166**.
16. E. M. Hillman and S. A. Burgess, "Sub-millimeter resolution 3D optical imaging of living tissue using laminar optical tomography," Laser Photon. Rev. **3**, 159–179 (2009).
17. S. A. Burgess, M. B. Bouchard, B. Yuan, and E. Hillman, "Simultaneous multiwavelength laminar optical tomography," Opt. Lett. **33**, 2710–2712 (2008).
18. U. Morgner, W. Drexler, F. X. Kärtner, X. D. Li, C. Pitris, E. P. Ippen, and J. G. Fujimoto, "Spectroscopic optical coherence tomography," Opt. Lett. **25**, 111–113 (2000).
19. R. Leitgeb, M. Wojtkowski, A. Kowalczyk, C. K. Hitzenberger, M. Sticker, and A. F. Fercher, "Spectral measurement of absorption by spectroscopic frequency-domain optical coherence tomography," Opt. Lett. **25**, 820–822 (2000).
20. F. E. Robles, C. Wilson, G. Grant, and A. Wax, "Molecular imaging true-colour spectroscopic optical coherence tomography," Nat. Photonics **5**, 744–747 (2011).
21. F. E. Robles, S. Chowdhury, and A. Wax, "Assessing hemoglobin concentration using spectroscopic optical coherence tomography for feasibility of tissue diagnostics," Biomed. Opt. Express **1**, 310–317 (2010).
22. C.-W. Lu, C.-K. Lee, M.-T. Tsai, Y.-M. Wang, and C. C. Yang, "Measurement of the hemoglobin oxygen saturation level with spectroscopic spectral-domain optical coherence tomography," Opt. Lett. **33**, 416–418 (2008).
23. D. Jacob, R. L. Shelton, and B. E. Applegate, "Fourier domain pump-probe optical coherence tomography imaging of melanin," Opt. Express **18**, 12399–12410 (2010).
24. C. P. Fleming, J. Eckert, E. F. Halpern, J. A. Gardecki, and G. J. Tearney, "Depth resolved detection of lipid using spectroscopic optical coherence tomography," Biomed. Opt. Express **4**, 1269–1284 (2013).
25. Y. L. Li, K. Seekell, H. Yuan, F. E. Robles, and A. Wax, "Multispectral nanoparticle contrast agents for true-color spectroscopic optical coherence tomography," Biomed. Opt. Express **3**, 1914–1923 (2012).
26. A. L. Oldenburg, M. N. Hansen, T. S. Ralston, A. Wei, and S. A. Boppart, "Imaging gold nanorods in excised human breast carcinoma by spectroscopic optical coherence tomography," J. Mater. Chem. **19**, 6407–6411 (2009).
27. H. Cang, T. Sun, Z.-Y. Li, J. Chen, B. J. Wiley, Y. Xia, and X. Li, "Gold nanocages as contrast agents for spectroscopic optical coherence tomography," Opt. Lett. **30**, 3048–3050 (2005).
28. C. Xu, J. Ye, D. L. Marks, and S. A. Boppart, "Near-infrared dyes as contrast-enhancing agents for spectroscopic optical coherence tomography," Opt. Lett. **29**, 1647–1649 (2004).
29. C. Yang, L. E. L. McGuckin, J. D. Simon, M. A. Choma, B. Applegate, and J. A. Izatt, "Spectral triangulation molecular contrast optical coherence tomographywith indocyanine green as the contrast agent," Opt. Lett. **29**, 2016–2018 (2004).
30. F. E. Robles and A. Wax, "Separating the scattering and absorption coefficients using the real and imaginary parts of the refractive index with low-coherence interferometry," Opt. Lett. **35**, 2843–2845 (2010).
31. F. E. Robles and A. Wax, "Measuring morphological features using light-scattering spectroscopy and Fourier-domain low-coherence interferometry," Opt. Lett. **35**, 360–362 (2010).
32. F. E. Robles, Y. Zhu, J. Lee, S. Sharma, and A. Wax, "Detection of early colorectal cancer development in the azoxymethane rat carcinogenesis model with Fourier domain low coherence interferometry," Biomed. Opt. Express **1**, 736–745 (2010).
33. D. S. Kauvar, S. E. Wolf, C. E. Wade, L. C. Cancio, E. M. Renz, and J. B. Holcomb, "Burns sustained in combat explosions in Operations Iraqi and Enduring Freedom (OIF/OEF explosion burns)," Burns **32**, 853–857 (2006).
34. E. Finkelstein, P. S. Corso, and T. R. Miller, *The Incidence and Economic Burden of Injuries in the United States* (Oxford University, 2006).
35. A. D. Jaskille, J. C. Ramella-Roman, J. W. Shupp, M. H. Jordan, and J. C. Jeng, "Critical review of burn depth assessment techniques: part II. Review of laser doppler technology," J. Burn Care Res. **31**, 151–157 (2010).

Research Article Vol. 1, No. 2 / August 2014 / Optica 112

Hybrid silicon and lithium niobate electro-optical ring modulator

LI CHEN, QIANG XU, MICHAEL G. WOOD, AND RONALD M. REANO*

Electroscience Laboratory, Department of Electrical and Computer Engineering—The Ohio State University, Columbus, Ohio 43212, USA

**Corresponding author: reano.1@osu.edu*

Received 24 April 2014; revised 19 June 2014; accepted 25 June 2014 (Doc. ID 210673); published 15 August 2014

Of all oxides, lithium niobate ($LiNbO_3$) is the gold standard electro-optical material in fiber-optic transmission systems. Modulators based on diffused waveguides in bulk $LiNbO_3$ substrates are, however, relatively large. In contrast, ring modulators based on silicon-on-insulator are of interest for chip-scale electro-optical modulation, but unstrained crystalline silicon does not exhibit a linear electro-optic effect, so modulation is based on alternative mechanisms such as the plasma dispersion effect. Here, we present a hybrid silicon and $LiNbO_3$ electro-optical ring modulator operating at gigahertz frequencies. The modulator consists of a 15 μm radius silicon microring and an ion-sliced $LiNbO_3$ thin film bonded together via benzocyclobutene. Fabricated devices operating in the TE optical mode exhibit an optical loaded quality factor of 14,000 and a resonance tuning of 3.3 pm/V. The small-signal electrical-to-optical 3 dB bandwidth is measured to be 5 GHz. Digital modulation with an extinction ratio greater than 3 dB is demonstrated up to 9 Gb/s. High-speed and low-tuning-power chip-scale modulators that exploit the high-index contrast of silicon with the second-order susceptibility of $LiNbO_3$ are envisioned.

OCIS codes: (130.3120) Integrated optics devices; (130.3730) Lithium niobate; (130.4110) Modulators; (230.2090) Electro-optical devices; (230.5750) Resonators; (250.7360) Waveguide modulators.

http://dx.doi.org/10.1364/OPTICA.1.000112

1. INTRODUCTION

Modulators are fundamental components for optical links. Lithium niobate ($LiNbO_3$) guided-wave electro-optic modulators satisfy bandwidth, linearity, and chirp requirements in fiber-optic transmission systems [1]. The physical dimensions of diffused waveguide modulators in bulk $LiNbO_3$ substrates are, however, on the scale of centimeters. The potential for dense integration is limited.

Silicon-on-insulator (SOI) modulators are of interest for chip-scale modulation [2]. Applications include short-reach optical interconnects [3], long-haul optical communications [4], analog optical links [5], and reconfigurable optical filters [6]. While the large refractive index and low optical absorption of silicon make it an attractive medium in the telecommunications wavelength range, unstrained crystalline silicon does not exhibit a linear electro-optic effect. Consequently, silicon optical modulators rely on alternative mechanisms such as the plasma dispersion effect to achieve electro-optical modulation [7,8]. While effective, plasma dispersion relies on carrier transport. Consequently, refractive index modulation is accompanied by absorption, and steady-state electrical tuning of optical resonances can consume significant power. Alternatively, electro-optic effects from second-order susceptibility can be induced by straining silicon waveguides [9]. Reported values of $V_\pi L$ in the 100 V · cm range indicate, however, that the effect is relatively weak [10,11].

Recently, a hybrid silicon and $LiNbO_3$ material system consisting of silicon waveguide ring resonators bonded to ion-sliced $LiNbO_3$ thin films has been introduced to combine the dense integration of silicon photonics with the second-order susceptibility of $LiNbO_3$ [12–14]. In the hybrid system, a thin film of $LiNbO_3$ is bonded to the top of a silicon waveguide to serve as a portion of the top cladding of an optical waveguide mode. The advantages are threefold. First, the silicon waveguide can serve as an optically transparent electrode to enhance voltage-induced electric fields in the $LiNbO_3$ [14].

2334-2536/14/020112-07$15/0$15.00

Second, large shifts of optical resonance with applied voltage are enabled in the absence of significant absorption. Third, steady-state DC power consumption for the tuning of optical resonance frequencies can potentially be very low due to the capacitive geometry. Tunable filters and radio-frequency electric field sensors have been demonstrated; however, a high-speed electro-optical ring modulator has not been reported in the literature to date.

In this paper, we present the experimental demonstration of a hybrid silicon and $LiNbO_3$ electro-optical microring resonator modulator operating at gigahertz frequencies. The device consists of a 15 μm radius silicon ring resonator and a 1 μm thick z-cut $LiNbO_3$ ion-sliced thin film bonded together by benzocyclobutene (BCB). Fabricated devices operating in the transverse-electric (TE) optical mode exhibit an optical loaded quality factor of 14,000 and a resonance tuning of 3.3 pm/V. High-frequency scattering parameters are used to extract an RC circuit model for the modulator. The small-signal electrical-to-optical 3 dB bandwidth is measured to be 5 GHz. Digital modulation with an extinction ratio (ER) greater than 3 dB is demonstrated up to 9 Gb/s.

This paper is organized as follows. Design and fabrication details of the modulator are first described. Next, DC and small-signal high-frequency measurements are presented. High-speed data modulation results are then conveyed, followed by concluding remarks.

2. METHODS

A. Design

A schematic of the hybrid silicon and $LiNbO_3$ modulator is shown in Fig. 1. The cross section is through the center of the ring resonator. The device consists of a 15 μm radius silicon rib waveguide ring and a 1 μm thick z-cut ion-sliced $LiNbO_3$ thin film bonded via BCB [13]. The rib waveguides are 500 nm wide, with a 45 nm slab thickness and 205 nm rib height. The silicon slab is patterned so that it exists only around and exterior to the ring. The silicon core and surrounding silicon slab layer are doped to function as a transparent conductor with reduced series resistance [14]. A voltage applied between the top electrode and the bottom electrode produces an electric field confined between the top electrode and the silicon waveguide core. The electric field interacts with the portion of the optical mode in the $LiNbO_3$ cladding, modifying the mode effective index by the linear electro-optic effect. As a result, the optical transmission response of the ring resonator is modulated.

The 1550 nm wavelength TE optical mode distribution is shown in Fig. 2 calculated by the beam propagation method. The refractive indices of silicon, SiO_2, $LiNbO_3$, and BCB are set to 3.48, 1.44, 2.21, and 1.54, respectively, in the simulation. The effective index of the optical mode is 2.66. Also shown is the voltage-induced electric field (yellow vectors) from a DC voltage applied between the top electrode and the silicon transparent conductor, using material permittivities in finite element method calculations [15–17].

The optical mode and the electric field vectors overlap in the $LiNbO_3$. The fraction of the optical mode power in the $LiNbO_3$ is 11%. The TE mode accesses the r_{13} electro-optic coefficient in $LiNbO_3$ ($r_{13} = 8\ \mathrm{pm\,V^{-1}}$ in bulk $LiNbO_3$) [15] and takes advantage of the nearly vertical voltage-induced electric field in the $LiNbO_3$.

The device speed is limited by the RC time constant and the photon lifetime in the ring resonator [2]. The electrical resistance originates primarily from the silicon transparent conductor and the contact resistance. To reduce the resistance, the silicon waveguide is blanket implanted with P-type dopants at a light dose, followed by a P-type heavy dose on the slab. The heavily doped region is 300 nm away from the silicon core to avoid excessive optical loss.

B. Fabrication

The fabrication process begins with a SOI wafer with a silicon device layer thickness of 250 nm and a buried SiO_2 layer thickness of 1 μm. The silicon waveguides are patterned with hydrogen silsesquioxane (HSQ) resist using electron beam lithography and inductively coupled plasma reactive ion etching (ICP-RIE) to obtain a rib waveguide geometry with a slab thickness of 45 nm [18]. The coupling gap between the bus waveguides and the ring waveguides is 200 nm. The slab is patterned with a second HSQ resist layer and ICP-RIE. After patterning, the slab only exists around and exterior to the ring waveguides and on one side of the bus waveguides. After patterning the slab regions, the HSQ mask over the waveguide and the slab is removed, and 20 nm of plasma-enhanced chemical vapor deposition (PECVD) SiO_2 is deposited. The sample is then blanket implanted with 45 keV BF_2^+ ions at a fluence of 1.8×10^{13} ions $\mathrm{cm^{-2}}$ to lightly dope the silicon

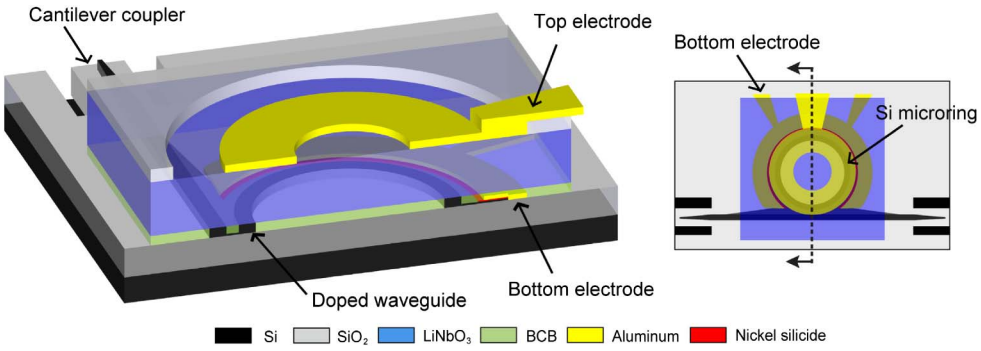

Fig. 1. Schematic of the hybrid silicon and $LiNbO_3$ ring modulator.

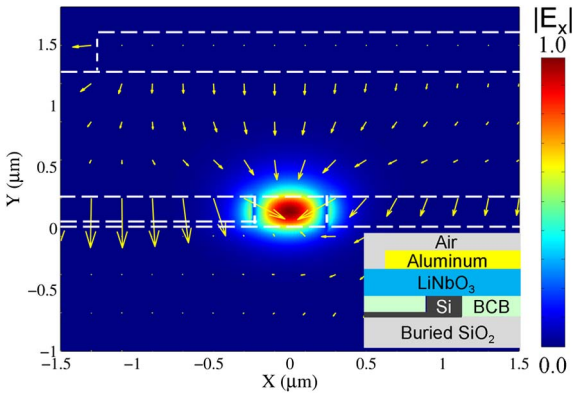

Fig. 2. Calculated optical TE mode distribution at 1550 nm wavelength (E_x component) and DC voltage-induced electric field vectors.

core. After implantation, the sample is annealed using rapid thermal annealing (RTA) to activate and drive in the dopants.

The slab is then heavily doped with 45 keV BF_2^+ ions at a fluence of 3×10^{15} cm^{-2}. Figure 3(a) shows the top-view scanning electron micrograph of the device after this step. Nickel silicide is formed in the heavily doped region before 100 nm of aluminum is deposited as the bottom electrode. A 350 nm thick BCB layer is then spin-coated and etched back to a 250 nm thickness to allow for planarization of the waveguide topology.

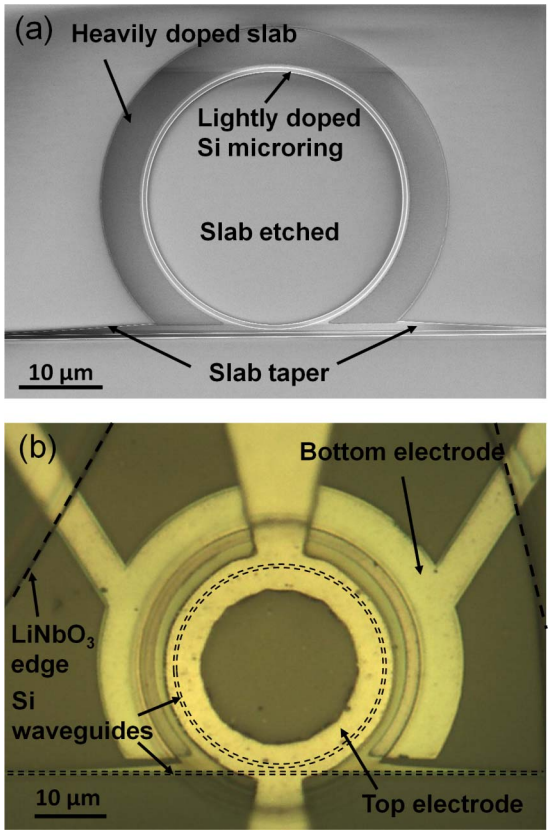

Fig. 3. (a) Scanning electron micrograph of the silicon microring resonator after slab patterning and doping; (b) top-view optical micrograph of the fabricated device.

To obtain $LiNbO_3$ thin films, a z-cut $LiNbO_3$ wafer is implanted with He^+ ions with an implantation energy of 342 keV and a fluence of 4×10^{16} ions cm^{-2}. After implantation, the wafer is flip bonded to an unpolished silicon wafer and baked on a hotplate at 300°C for 5 min. The heating causes blistering of the implanted $LiNbO_3$ wafer surface due to the aggregation of helium bubbles [19]. One micrometer thick $LiNbO_3$ thin films are exfoliated from the bulk and transferred to the silicon wafer. The exfoliated thin films on the silicon wafer are then annealed by RTA at 1000°C for 30 s to repair the crystal lattice and restore the electro-optic properties. The surface roughness of the exfoliated side of the $LiNbO_3$ thin film is 6 nm. $LiNbO_3$ thin films are transferred and bonded to the Si microring resonators using a micro-vacuum tip on a probe station. After transfer, the sample is annealed to cure the BCB. Residual BCB not covered by the $LiNbO_3$ thin film is etched via ICP-RIE with CF_4/O_2 chemistry. One micrometer thick PECVD SiO_2 film is deposited as a capping layer. The SiO_2 film over the ring resonator is removed to form a 40 μm diameter via hole. A 300 nm thick top aluminum electrode, connected to a ground-signal-ground radio-frequency (RF) pad, is patterned on top of the $LiNbO_3$ thin film. Finally, cantilever couplers are patterned for fiber-to-chip optical coupling [20,21]. A top-view optical micrograph of the fabricated device is shown in Fig. 3(b).

3. RESULTS AND DISCUSSION

A. DC and Small-Signal High-Frequency Measurements

Optical transmission measurements are performed to characterize the electrical tuning of optical resonances. TE-mode light from a tunable infrared continuous-wave laser source is coupled through the input and output fiber-to-chip cantilever couplers of the modulator. DC voltage is applied to the top electrode of the modulator while the bottom electrode is grounded. Figure 4 shows the measured TE-mode spectrum as a function of the applied DC voltage. The resonance wavelength redshifts with increasingly positive voltage. The total optical insertion loss is 4.3 dB. The insertion loss is from

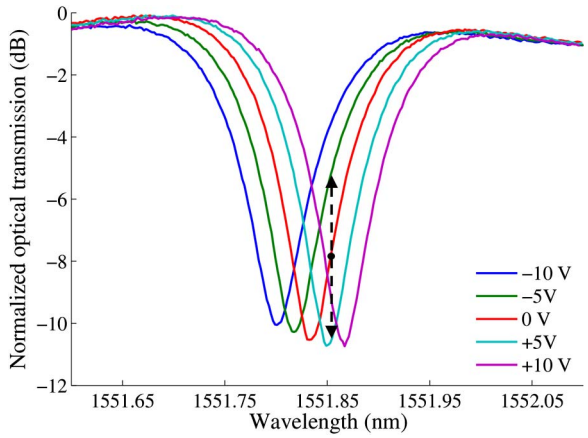

Fig. 4. Measured optical transmission of a single resonance as a function of applied voltage.

3 dB of fiber-to-waveguide coupling loss and 1.3 dB of waveguide transmission loss [18,20,21]. The decrease of the optical transmission minimum with voltage is attributed to Fabry–Perot fringes that are present due to fiber-to-chip coupling. The resonance shift is 66 pm for a change in DC bias from −10 to 10 V, indicating 3.3 pm/V tuning, which is equivalent to a $V_\pi L$ of 9.1 V · cm. The measured quality factor is 14,000, the FWHM is 13.7 GHz, and the group index is 4.0. At 1551.856 nm, the optical transmission intensity varies by 5.2 dB with a −5 to 5 V voltage swing, as indicated by the dashed arrow in Fig. 4.

The RF scattering parameter, S_{11}, is measured with a 20 GHz vector network analyzer operating in a 50 Ω system. Figure 5(a) shows the measured S_{11} magnitude and phase data. The magnitude of S_{11} drops sharply to −2 dB from 40 MHz to 2 GHz and then gradually rolls off to −4.5 dB at 20 GHz. An RC circuit model extracted from the measured S_{11} is shown in Fig. 5(b) [8]. Parameter R_C denotes the resistance of the metal electrodes. Parameter C_P represents the parasitic capacitance between the metal electrodes through the top dielectric materials and the air. Parameters C_J and R_S model the electrical path through the silicon transparent electrode and the $LiNbO_3$ layer. Parameters C_{OX} and R_{Si} model the electrical path through the buried oxide and the silicon substrate. The value of C_J is in good agreement with finite element method simulations. The relatively high value of R_S indicates a lower than expected doping concentration in the waveguide and a higher than expected contact resistance [22]. The relatively large C_p value is mainly attributed to the parasitic capacitance of the electric pads. The sharp drop at the lower frequency band is attributed to the RF coupling through the substrate.

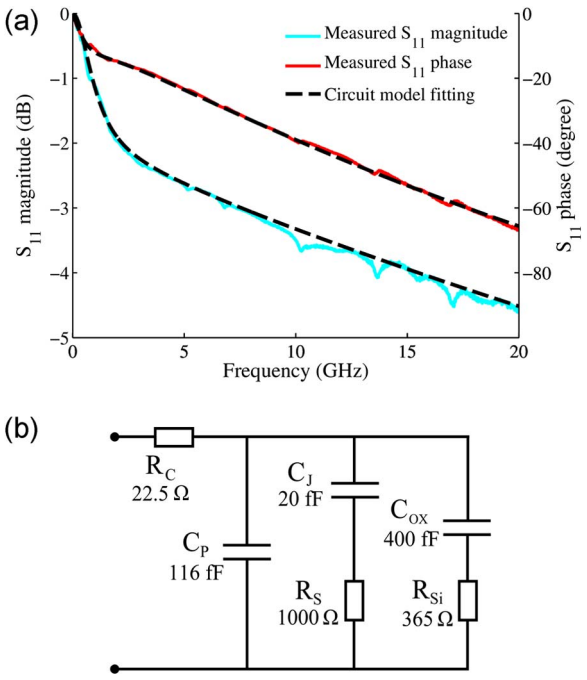

Fig. 5. (a) RF S_{11} scattering parameter; (b) RC circuit model of the modulator.

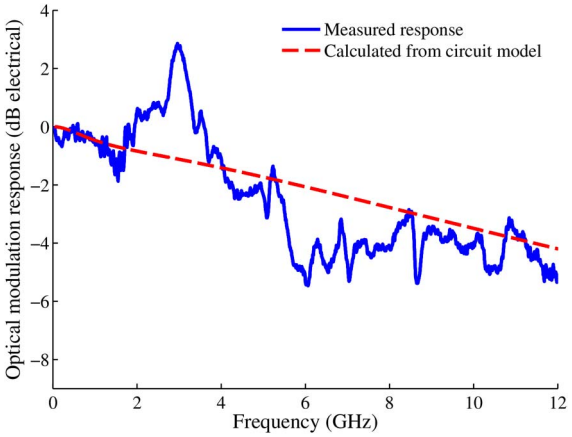

Fig. 6. Electrical-to-optical modulation response.

The small-signal electrical-to-optical modulation response is shown in Fig. 6. The modulated optical signal is detected with a photodetector with a 3 dB bandwidth of 12 GHz. Also shown in Fig. 6 is the frequency response of the voltage across C_J in the circuit model shown in Fig. 5(b) [8]. The measured 3 dB optical response bandwidth of the modulator is approximately 5 GHz. While the general trend of the optical responses matches the circuit model, the optical response contains additional dips and peaks across the entire frequency band.

The dips and peaks on the optical modulation response are a result of acousto-optic resonances [23–25]. The electric fields between the electrodes excite acoustic waves in the 1 μm thick $LiNbO_3$, producing resonances in the gigahertz frequency range. Multiple resonance peaks apparent in the S_{11} measurements at 1.7 GHz and corresponding harmonics indicate the conversion of the electrical energy to acoustic energy at the acoustic resonances. Consequently, refractive index changes occur in the $LiNbO_3$ through the elasto-optic effect. The acoustic resonances can be suppressed by roughening the surface of the piezoelectric material to increase the scattering loss of the acoustic wave [26,27]. The surface roughness can be produced by dry or wet etching [28]. Sufficiently thick $LiNbO_3$ avoids optical mode interaction with the rough surface.

B. High-Speed Digital Modulation

A schematic for the high-speed digital modulation characterization is shown in Fig. 7 [8]. A pulse pattern generator (PPG) outputs a $2^{31}-1$ pseudorandom-bit-stream data stream (PRBS31) with a voltage swing from −1 to 1 V. The peak-to-peak amplitude of the signal is amplified to 5 V (−2.5 to 2.5 V) with a modulator driver amplifier. Due to the microwave reflection from the capacitive device, the voltage swing across the modulator electrode is doubled to 10 V at DC [8]. The output light from the modulator is passed through a fiber amplifier and an optical passband filter with 0.5 nm bandwidth to amplify the signal and suppress the amplified spontaneous emission noise. The amplified optical signal is attenuated and connected to a 30 GHz optical module on

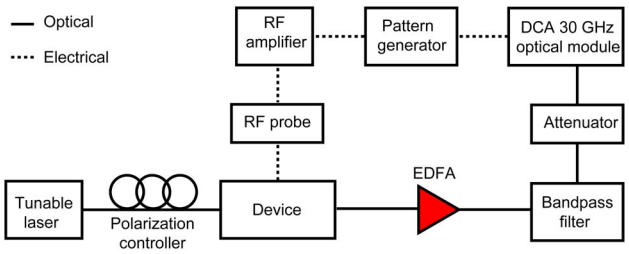

Fig. 7. Measurement setup for digital characterization. EDFA, erbium-doped fiber amplifier.

a digital communication analyzer (DCA) synchronized to the clock of the PPG for generating optical eye diagrams. The optical bias wavelength is tuned to maximize the ER.

The left column of Fig. 8 shows measured optical eye diagrams at 1, 4.5, 5, and 9 Gb/s, with ERs of 4.7, 4.5, 4, and 3 dB, respectively. The right column of Fig. 8 shows simulated eye diagrams at the corresponding bit rates with ideal PRBS driving signals. The modeling incorporates the measured frequency response in Fig. 6 and the optical resonance spectrum of the modulator in Fig. 4. The ER and shape of the simulated optical eyes agree well with the measurement results. In particular, the amplitude ringing for the 1 Gb/s eye and the partial eye closing on the left part of the 5 Gb/s eye closely match the simulation.

The total energy consumption of the modulator is estimated to be 4.4 pJ/bit at 9 Gb/s with a 10 V swing. The energy per bit encompasses 0.4 pJ/bit from C_J, 1.8 pJ/bit from C_P, and 2.2 pJ/bit from C_{OX}. The energy consumption on C_J is only 9% of the total energy consumption. The majority of the energy consumption is attributed to charging and discharging of the large area electrical pads for test and measurement. Energy consumption can be reduced by optimizing device capacitances. Operating in the optical TM mode also reduces the energy per bit due to the increase in tunability from a larger electro-optic coefficient ($r_{33} = 31$ pm V^{-1} [15]) and greater overlap between RF and optical fields.

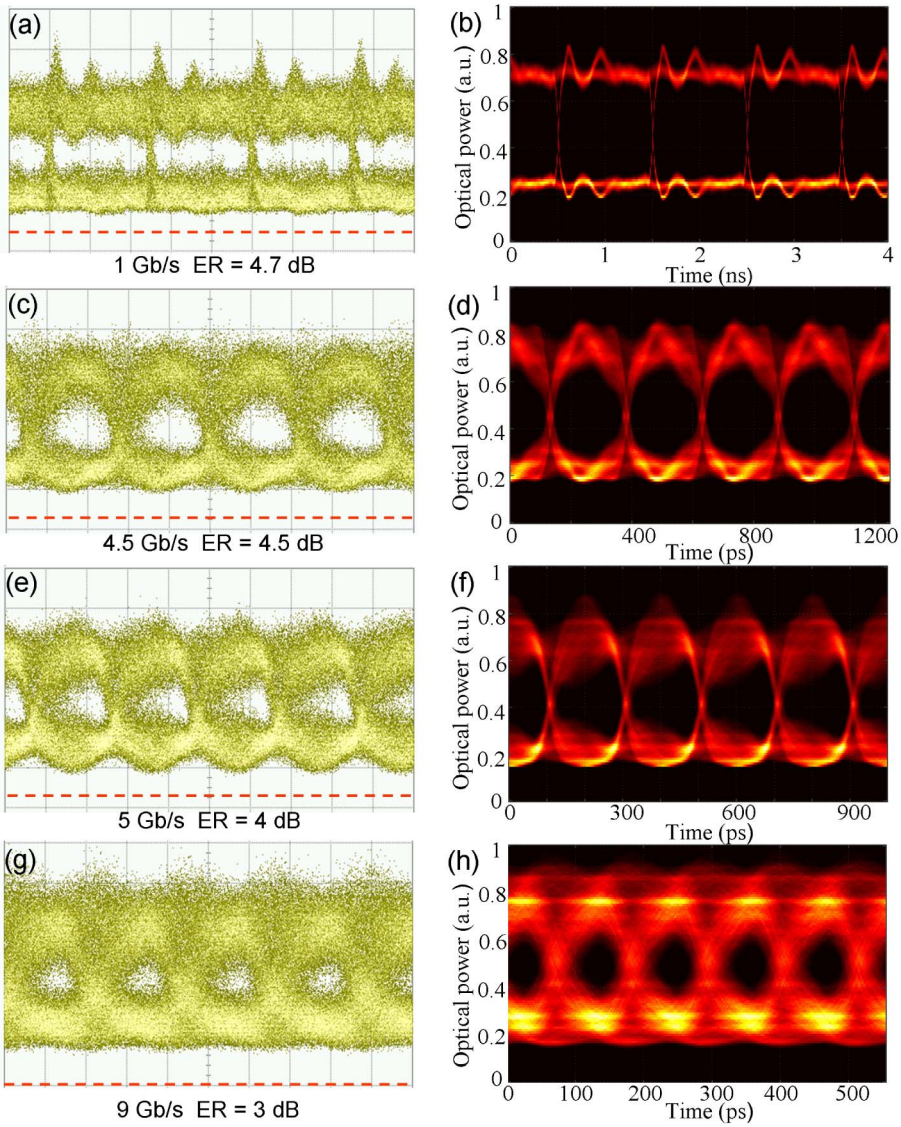

Fig. 8. Measured (left column) and simulated (right column) optical eye: (a), (b) 1 Gb/s; (c), (d) 4.5 Gb/s; (e), (f) 5 Gb/s; (g), (h) 9 Gb/s. The red dashed line in the measurement indicates the reference level for zero optical input. The vertical scale is 500 μW per division.

Steady-state DC power consumption for the tuning of optical resonance frequencies is ideally zero in the capacitive device.

4. CONCLUSION

A hybrid silicon and $LiNbO_3$ microring resonator modulator operating at gigahertz frequencies is designed, fabricated, and characterized. The hybrid modulator consists of an ion-sliced $LiNbO_3$ thin film bonded to a silicon waveguide ring resonator via BCB. Fabricated devices operating in the TE optical mode exhibit an optical loaded quality factor of 14,000 and a resonance tuning of 3.3 pm/V. High-frequency scattering parameters are used to extract an RC circuit model for the modulator. The small-signal electrical-to-optical 3 dB bandwidth is measured to be 5 GHz. Digital modulation with an ER greater than 3 dB is demonstrated up to 9 Gb/s. Future work involves optimizing the RC time constant, suppressing the acousto-optic resonances, and reducing the driving voltage in TE- and TM-mode designs to achieve higher data rates and lower energy consumption. High-speed and low-tuning-power chip-scale optical modulators that exploit the high-index contrast of silicon with the second-order susceptibility of $LiNbO_3$ are envisioned.

More broadly, new horizons become apparent when exploiting the capability of silicon to provide submicrometer spatial confinement of light and the ability of lithium niobate to mediate second-order nonlinear optical effects. Empowering silicon with second-order susceptibility opens a suite of nonlinear optics to the chip scale, including second-harmonic generation, difference frequency generation, optical rectification, and sum frequency generation for applications in classical and quantum information processing [29–31].

FUNDING INFORMATION

Army Research Office (ARO) (W911NF-12-1-0488).

REFERENCES

1. E. L. Wooten, K. M. Kissa, A. Yi-Yan, E. J. Murphy, D. A. Lafaw, P. F. Hallemeier, D. Maack, D. V. Attanasio, D. J. Fritz, G. J. McBrien, and D. E. Bossi, "A review of lithium niobate modulators for fiber-optic communications systems," IEEE J. Sel. Top. Quantum Electron. **6**, 69–82 (2000).
2. G. T. Reed, G. Mashanovich, F. Y. Gardes, and D. J. Thomson, "Silicon optical modulators," Nat. Photonics **4**, 518–526 (2010).
3. D. A. B. Miller, "Device requirements for optical interconnects to silicon chips," Proc. IEEE **97**, 1166–1185 (2009).
4. A. Biberman, S. Manipatruni, N. Ophir, L. Chen, M. Lipson, and K. Bergman, "First demonstration of long-haul transmission using silicon microring modulators," Opt. Express **18**, 15544–15552 (2010).
5. M. Streshinsky, A. Ayazi, Z. Xuan, A. E.-J. Lim, G.-Q. Lo, T. Baehr-Jones, and M. Hochberg, "Highly linear silicon traveling wave Mach-Zehnder carrier depletion modulator based on differential drive," Opt. Express **21**, 3818–3825 (2013).
6. S. S. Djordjevic, L. W. Luo, S. Ibrahim, N. K. Fontaine, C. B. Poitras, B. Guan, L. Zhou, K. Okamoto, Z. Ding, M. Lipson, and S. J. B. Yoo, "Fully reconfigurable silicon photonic lattice filters with four cascaded unit cells," IEEE Photon. Technol. Lett. **23**, 42–44 (2011).
7. Q. Xu, B. Schmidt, S. Pradhan, and M. Lipson, "Micrometre-scale silicon electro-optic modulator," Nature **435**, 325–327 (2005).
8. G. Li, X. Zheng, J. Yao, H. Thacker, I. Shubin, Y. Luo, K. Raj, J. E. Cunningham, and A. V. Krishnamoorthy, "25 Gb/s 1V-driving CMOS ring modulator with integrated thermal tuning," Opt. Express **19**, 20435–20443 (2011).
9. R. S. Jacobsen, K. N. Andersen, P. I. Borel, J. Fage-Pedersen, L. H. Frandsen, O. Hansen, M. Kristensen, A. V. Lavrinenko, G. Moulin, H. Ou, C. Peucheret, B. Zsigri, and A. Bjarklev, "Strained silicon as a new electro-optic material," Nature **441**, 199–202 (2006).
10. B. Chmielak, M. Waldow, C. Matheisen, C. Ripperda, J. Bolten, T. Wahlbrink, M. Nagel, F. Merget, and H. Kurz, "Pockels effect based fully integrated, strained silicon electro-optic modulator," Opt. Express **19**, 17212–17219 (2011).
11. B. Chmielak, C. Matheisen, C. Ripperda, J. Bolten, T. Wahlbrink, M. Waldow, and H. Kurz, "Investigation of local strain distribution and linear electro-optic effect in strained silicon waveguides," Opt. Express **21**, 25324–25332 (2013).
12. Y. S. Lee, G.-D. Kim, W.-J. Kim, S.-S. Lee, W.-G. Lee, and W. H. Steier, "Hybrid Si-$LiNbO_3$ microring electro-optically tunable resonators for active photonic devices," Opt. Lett. **36**, 1119–1121 (2011).
13. L. Chen and R. M. Reano, "Compact electric field sensors based on indirect bonding of lithium niobate to silicon microrings," Opt. Express **20**, 4032–4038 (2012).
14. L. Chen, M. G. Wood, and R. M. Reano, "12.5 pm/V hybrid silicon and lithium niobate optical microring resonator with integrated electrodes," Opt. Express **21**, 27003–27010 (2013).
15. K. K. Wong, *Properties of Lithium Niobate* (INSPEC, 2002).
16. M. E. Mills, P. Townsend, D. Castillo, S. Martin, and A. Achen, "Benzocyclobutene (DVS-BCB) polymer as an interlayer dielectric (ILD) material," Microelectron. Eng. **33**, 327–334 (1997).
17. S. M. Sze and K. K. Ng, *Physics of Semiconductor Devices* (Wiley, 1981).
18. M. G. Wood, L. Chen, J. R. Burr, and R. M. Reano, "Optimization of electron beam patterned hydrogen silsesquioxane mask edge roughness for low-loss silicon waveguides," J. Nanophoton. **8**, 083098 (2014).
19. A. Guarino, G. Poberaj, D. Rezzonico, R. Degl'Innocenti, and P. Günter, "Electro-optically tunable microring resonators in lithium niobate," Nat. Photonics **1**, 407–410 (2007).
20. M. Wood, P. Sun, and R. M. Reano, "Compact cantilever couplers for low-loss fiber coupling to silicon photonic integrated circuits," Opt. Express **20**, 164–172 (2012).
21. P. Sun and R. M. Reano, "Cantilever couplers for intra-chip coupling to silicon photonic integrated circuits," Opt. Express **17**, 4565–4574 (2009).
22. R. Ding, T. Baehr-Jones, Y. Liu, R. Bojko, J. Witzens, S. Huang, J. Luo, S. Benight, P. Sullivan, J.-M. Fedeli, M. Fournier, L. Dalton, A. Jen, and M. Hochberg, "Demonstration of a low $V_\pi L$ modulator with GHz bandwidth based on electro-optic polymer-clad silicon slot waveguides," Opt. Express **18**, 15618–15623 (2010).
23. J. L. Nightingale, R. A. Becker, R. C. Willis, and J. S. Vrhel, "Characterization of frequency dispersion in Ti-diffused lithium niobate optical devices," Appl. Phys. Lett. **51**, 716–718 (1987).
24. R. L. Jungerman and C. A. Flory, "Low-frequency acoustic anomalies in lithium niobate Mach-Zehnder interferometers," Appl. Phys. Lett. **53**, 1477–1479 (1988).
25. W. K. Burns, M. M. Howerton, R. P. Moeller, R. Krähenbühl, R. W. McElhanon, and A. S. Greenblatt, "Low drive voltage, broad-band $LiNbO_3$ modulators with and without etched ridges," J. Lightwave Technol. **17**, 2551–2555 (1999).
26. A. Vorobiev, J. Berge, S. Gevorgian, M. Löffler, and E. Olsson, "Effect of interface roughness on acoustic loss in tunable thin film bulk acoustic wave resonators," J. Appl. Phys. **110**, 024116 (2011).
27. M. Yoshida, S. Okamoto, T. Omiya, K. Kasai, and M. Nakazawa, "256 QAM digital coherent optical transmission using Raman amplifiers," IEICE Trans. Commun. E **94-B**, 417–424 (2011).

28. Z. Ren, P. J. Heard, J. M. Marshall, P. A. Thomas, and S. Yu, "Etching characteristics of $LiNbO_3$ in reactive ion etching and inductively coupled plasma," J. Appl. Phys. **103**, 034109 (2008).
29. M. Cazzanelli, F. Bianco, E. Borga, G. Pucker, M. Ghulinyan, E. Degoli, E. Luppi, V. Véniard, S. Ossicini, D. Modotto, S. Wabnitz, R. Pierobon, and L. Pavesi, "Second-harmonic generation in silicon waveguides strained by silicon nitride," Nat. Mater. **11**, 148–154 (2011).
30. M. Wächter, C. Matheisen, M. Waldow, T. Wahlbrink, J. Bolten, M. Nagel, and H. Kurz, "Optical generation of terahertz and second-harmonic light in plasma-activated silicon nanophotonic structures," Appl. Phys. Lett. **97**, 161107 (2010).
31. K. Banaszek, A. B. U'Ren, and I. A. Walmsley, "Generation of correlated photons in controlled spatial modes by down conversion in nonlinear waveguides," Opt. Lett. **26**, 1367–1369 (2001).

Research Article Vol. 1, No. 2 / August 2014 / Optica 119

Single-shot measurement of the complete temporal intensity and phase of supercontinuum

TSZ CHUN WONG, MICHELLE RHODES,* AND RICK TREBINO

School of Physics, Georgia Institute of Technology, 837 State Street, Atlanta, Georgia 30332, USA

**Corresponding author: mrhodes3@gatech.edu*

Received 25 April 2014; revised 26 June 2014; accepted 28 June 2014 (Doc. ID 210812); published 15 August 2014

When a narrowband laser pulse evolves into a broadband pulse, for example, via transmission through a photonic crystal fiber, the resulting continuum usually exhibits massive shot-to-shot pulse-shape fluctuations. The continuum's extreme complexity prevents its single-shot measurement, with the best estimates so far resulting from an average over many pulses. Here we solve this problem using cross-correlation frequency-resolved optical gating, achieving the necessary large spectral range using a polarization-gating geometry and the necessary large temporal range by significantly tilting the reference pulse. Furthermore, we have also discovered that we can simultaneously cancel the previously unavoidable longitudinal geometrical smearing by using a carefully chosen combination of pulse tilt and beam-crossing angle, thus simultaneously achieving the required temporal resolution. We hence make a complete measurement of an individual complex continuum pulse generated in photonic crystal fiber. By enabling measurement of single optical rogue waves, this technique could provide insight and perhaps even lead to the prediction of when mathematically similar, destructive oceanic rogue waves may occur.

OCIS codes: (320.0320) Ultrafast optics; (320.7100) Ultrafast measurements.

http://dx.doi.org/10.1364/OPTICA.1.000119

1. INTRODUCTION

Supercontinuum (SC) generation is the remarkable nonlinear-optical process by which a narrowband laser pulse efficiently evolves into an extremely broadband pulse [1]. Photonic crystal fiber (PCF) is an especially advantageous medium, conveniently yielding a spatially coherent SC beam [2] and allowing a wide range of applications, including stimulated emission depletion microscopy, optical coherence tomography, optical frequency metrology, and carrier-envelope phase stabilization [3–6].

Interestingly, SC pulses are extremely temporally complex, and trains of them are inherently highly unstable [7–14]. As a result, it has never been possible to measure the temporal intensity and phase of a single SC pulse. Such measurements have been possible if averaged over many pulses, but at best they yield only an estimate of a typical SC pulse [15–21]. At worst, multi-shot measurements of such unstable pulse trains are susceptible to "coherent artifacts" that can mislead the unwary into believing that their pulses are erroneously simple [22,23].

SC measurement recently acquired increased urgency when it was noted (and confirmed) that SC can give rise to optical rogue waves, mathematically equivalent to the oceanic rogue waves that sink dozens of ships every year [24]. Numerical simulations and experimental observations of collections of single-shot spectra have confirmed that SC generation in PCF follows the same L-shaped statistics as oceanic waves, where statistically rare rogue events occur much more often than would be implied by simple Gaussian statistics [25,26]. While the measurement of an oceanic rogue wave is straightforward (if one happens upon such a rare event), its intentional generation is difficult and perhaps also ill-advised (unless on a very small scale). On the other hand, while the generation of an optical rogue wave is simple, routine, and safe, its single-shot complete measurement has remained impossible. Complete

measurements of optical rogue waves could lead to insight into, and eventually to the prediction of, their destructive and difficult-to-simulate oceanic counterparts [26–28].

Unfortunately, the challenges facing single-shot measurement of SC are many. A typical SC generated from PCF is several picoseconds long and has well over 100 nm of spectral bandwidth, easily achieving a time–bandwidth product (TBP) of ~100 or more. Such SC pulses are extremely complex, with fine structure in both the temporal and spectral domains. To further complicate the task, due to the small cores of PCFs, a SC pulse is quite weak, having at most ~20 nJ of energy. Since this energy is spread over a few picoseconds, the intensity of these pulses is also quite low. While addressing one (or occasionally two) of these requirements at a time is now routine, achieving nanojoule sensitivity, large temporal and spectral ranges, and fine temporal and spectral resolution simultaneously on a single shot has not yet been accomplished, despite an ever-increasing need to do so.

Here, we report a general technique that solves this problem. In order to deal with the low energy of the SC pulse, we use a cross-correlation frequency-resolved optical gating (XFROG) setup with a high-energy (regeneratively amplified) reference pulse. This setup provides much more signal and hence sensitivity than a self-referenced nonlinear measurement. Even better, XFROG has been demonstrated to retrieve extremely complicated pulse shapes very reliably [29]. We also chose a polarization-gating (PG) geometry, which has essentially infinite bandwidth and so nicely solves the spectral-width problem immediately. Unfortunately, PG has a drawback: it is a third-order nonlinear process, and therefore, even with a high-intensity reference pulse, it still requires a relatively long (>1 mm) nonlinear medium for adequate signal strength, which will prove problematic for other reasons that we will discuss shortly.

Achieving sufficient temporal range to measure SC is also nontrivial. A typical FROG or XFROG device achieves single-shot measurement by crossing the reference and unknown pulses inside the nonlinear medium at an angle, θ, as depicted in Fig. 1(a). This maps the delay onto the transverse spatial position in the nonlinear medium and also at the camera onto which the nonlinear medium is imaged. The temporal range of the device scales with the crossing angle, and delay ranges up to a few picoseconds are possible with this approach. However, since a delay range of several times the pulse length is necessary, this is not sufficient to measure SC pulses, which are typically longer. An old and well-known innovation that increased the temporal range of autocorrelators to tens of picoseconds was the use of pulse-front tilt (PFT) in the two pulses in the device [30]. We adapt this approach here for XFROG and add PFT, but only to the reference pulse (to avoid potentially distorting the SC). The temporal ranges with and without PFT, ΔT_{PFT} and ΔT, are given by (see Fig. 1)

$$\Delta T = \frac{d}{c}\tan\,\theta, \tag{1}$$

$$\Delta T_{\mathrm{PFT}} = \frac{d}{c}\tan(\alpha - \theta), \tag{2}$$

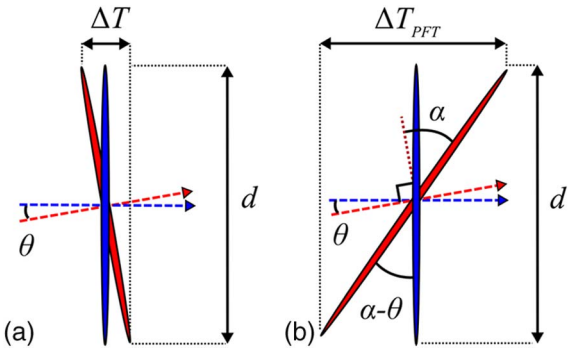

Fig. 1. Illustration of the temporal range calculation for single-shot XFROG [see Eqs. (1) and (2)]. (a) Typical device with an untilted reference pulse. The unknown and reference pulses are shown in blue and red, respectively, with arrows showing their propagation directions. The relative delay between the pulses varies transversely, and imaging the beam-crossing region onto a camera achieves single-shot operation. (b) Proposed approach using a reference pulse with pulse-front tilt to increase the temporal range. The tilt angle is α.

where d is the beam diameter, θ is the internal crossing angle, α is the PFT angle, and c is the speed of light. This can easily increase the temporal range by more than an order of magnitude, and hence solves the temporal range problem [31].

The last and most difficult requirement for measuring SC is achieving the required very fine temporal resolution. In a PG geometry (and most other beam geometries as well), this is severely limited by a fundamental effect called longitudinal geometrical smearing (LGS). As the pulses cross in the nonlinear medium, the line of constant delay drifts away from the direction of signal-beam propagation, causing a given camera pixel to see signal light generated from a range of delays, rather than just one delay [32]. The LGS increases with crossing angle at an even faster rate than the temporal range does, significantly limiting the temporal resolution in experiments requiring a large temporal range. In addition, LGS increases with the length of the nonlinear medium, limiting signal strength.

Interestingly, introducing PFT into the gate pulse has a significant impact on LGS, which has not yet been considered in the literature. As shown in the schematic of LGS in a PFT setup [Fig. 2(a)], the zero time delay between the reference and the unknown pulse is located at the centers of both beams at the entrance of the nonlinear medium. Because the signal in a PG geometry follows the same path as the unknown pulse, the spatial center of the signal beam corresponds to different time delays between the pulses as the two beams propagate in different directions. When the signal beam exits the nonlinear medium, the delay between the beams in the center is nonzero. The range of delays contained in the same transverse spatial location, δt_{PFT}, is the longitudinal smearing:

$$\delta t_{\mathrm{PFT}} = \frac{L}{c}\left(1 - \frac{\cos\,\alpha}{\cos(\alpha - \theta)}\right), \tag{3}$$

where L is the thickness of the nonlinear medium, α is the PFT angle, θ is the internal crossing angle, and c is the speed of light.

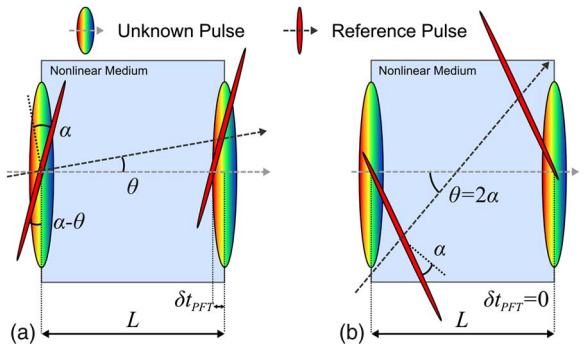

Fig. 2. Illustration of longitudinal geometrical smearing in single-shot XFROG. (a) General case with arbitrary internal crossing angle, θ, and PFT angle, α. The rectangle with thickness L represents the nonlinear medium. The reference and unknown pulses are shown in red and rainbow colors, respectively, with an arrow indicating their propagation direction. The signal pulse propagates along the same direction as the unknown pulse (the gray dashed line). In this direction, the reference pulse gates the green part (the center) of the unknown pulse at the front of the medium and the red part (the left) of the unknown pulse at the back of the medium. Thus, each transverse position contains signal light created by a range of delays, rather than a single delay. This range is the longitudinal smearing, δt_{PFT}. (b) The ideal choice of internal crossing angle, $\theta = 2\alpha$, removes the longitudinal smearing completely while maintaining a large delay range. The reference pulse overlaps with the same part of the unknown pulse at each transverse position throughout the medium. The PFT angle, α, here remains the same as in part (a).

Quite fortuitously, from Eq. (3), we find that for a given amount of PFT, a specific internal crossing angle can be chosen that actually perfectly eliminates the LGS. Indeed, Eq. (3) provides two such conditions: $\theta = 0$ and $\theta = 2\alpha$. The solution $\theta = 0$ is not practical in our setup, as it provides for copropagating reference and unknown pulses, which cannot be separated after their interaction inside the nonlinear medium. The second condition, $\theta = 2\alpha$, however, is ideal, and we implement it in our apparatus, thus solving the temporal resolution problem [see Fig. 2(b)]. This condition does not limit flexibility in the temporal range for the device, because the beam size is also a strong factor in determining the overall temporal range. In any case, removing LGS allows the use of a much thicker nonlinear medium (the next limitation on the medium thickness is group-velocity dispersion, which is significantly less restrictive, even for the SC's large spectral width, and can be included in the XFROG retrieval algorithm if desired). And as mentioned above, this also significantly increases the nonlinear interaction length and thus the sensitivity of the device, because the signal pulse energy scales as the square of the nonlinear medium thickness.

Finally, we use a regeneratively amplified reference pulse with 440 μJ of pulse energy, attenuated to just below the threshold for continuum generation in the nonlinear medium in order to maximize the nonlinear–optical interaction without distorting the reference pulse or SC pulse to be measured. This allows our device to measure even extremely weak SC on a single shot. An additional increase in device sensitivity could be achieved by time stretching (chirping) the reference pulse, whose phase is irrelevant in the measurement, so that it overlaps with a larger fraction of the unknown SC pulse. This proved unnecessary in our experiments, but we mention it here in case a weaker SC must be measured.

2. METHODS

To create the reference pulse, 80% of the energy from a regenerative amplifier was sent to a 45° polarizer and then to a 600 line/mm diffraction grating. To properly image the diffracted beam, we prefer that the first order diffracts along the normal of the grating surface, setting an incidence angle of 28.7° for 800 nm light. As is shown in Fig. 3, the diffracted beam has PFT because the right side of the pulse hits the grating before the left side of the pulse. This pulse was imaged with 1 : 1 imaging (using a 200 mm lens with 400 mm of propagation before and after) onto the nonlinear medium, 5 mm of BK7. Figure 3 also shows that the beam size is expanded by both the grating and the large incidence angle into the nonlinear medium. The beam expansion combined with the slower phase velocity in the glass causes the PFT angle in the nonlinear medium to be significantly less than the PFT angle in air just after the grating. The tilt angle α in the glass is given by (see Fig. 3)

$$\begin{aligned}\tan\alpha &= (b/n)/(dM(\cos\theta_2/\cos\theta_1))\\ &= \sin\gamma\cos\theta_1/nM\cos\theta_2,\end{aligned} \tag{4}$$

where b is the spatial delay caused by impinging on the grating at incidence angle γ, n of BK7 is ~1.5, d is the beam diameter at the grating, $M = 1$ is the magnification of the imaging lens, and θ_1 and θ_2 are the incidence and refracted angles, respectively, at the glass surface. We find that the reference pulse had a tilt of ~15° inside the nonlinear medium. It crossed with the SC pulse at an external angle of 43° to satisfy the condition to eliminate LGS. Fine adjustment of the crossing angle of the beams was accomplished by tweaking the angle of the BK7. The beam from the amplifier has a diameter d of about 1 cm. Using Eq. (2), we find that this yields a theoretical temporal range of about 14 ps. The effective temporal range is often less due to the drop-off in intensity in the wings of the beam, but this geometry is sufficient to measure SC pulses 2–3 ps long.

The other 20% of the amplifier pulse was made into a SC seed by spatially and spectrally filtering it (with a filter centered at 785 nm with FWHM 6.5 nm) and then stretching it with

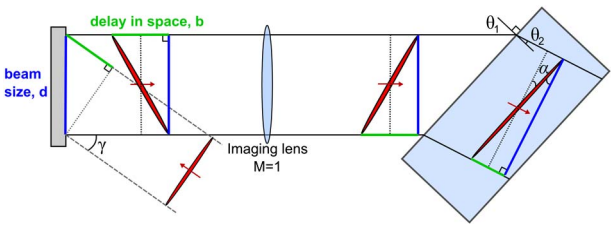

Fig. 3. Illustration of how to create PFT and calculate the resulting PFT angle in the nonlinear medium. The PFT angle in glass is smaller than the angle in air after the grating due to the larger size of the refracted beam and the slower phase velocity. The drawing is not to scale, and the angles are slightly exaggerated for clarity.

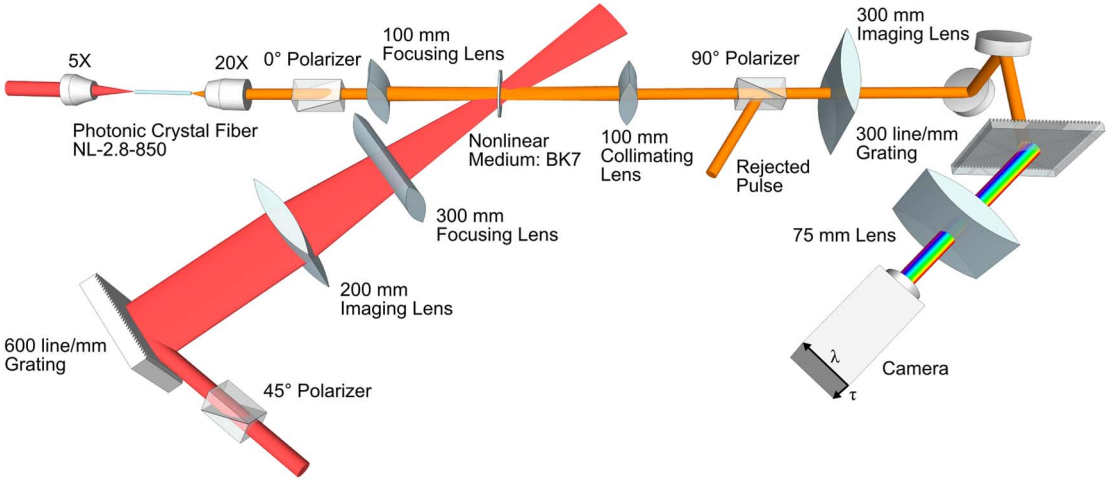

Fig. 4. 3D schematic of the experimental apparatus of PG XFROG with PFT in the reference pulse. The red and orange represent the reference pulse and the SC, respectively. The reference pulse gates the SC in the nonlinear medium, which is imaged onto the camera in the vertical direction, mapping time delay to spatial position. The spectrometer consists of a transmission grating and cylindrical lens that generate the spectrum of the gated SC pulse in the horizontal direction.

several centimeters of glass to reduce the peak intensity. It was focused into 23.1 mm of PCF fiber (NL-2.8-850-02, Thorlabs) with a microscope objective and collimated after the fiber with another microscope objective. The spatial profile of the SC was measured by a camera to confirm that it had a single spatial mode. A fiber-coupled spectrometer confirmed the absence of spatial chirp in the SC.

The remainder of our device was a standard single-shot PG XFROG. The experimental setup is shown in Fig. 4. The nonlinear medium was imaged into a simple homemade imaging spectrometer, and the SC pulse gated by the tilted reference pulse was spectrally resolved as a function of delay, yielding an XFROG trace (spectrogram) of the SC. The experimental apparatus had a temporal range (at the camera) of ~8 ps and a spectral range of ~360 nm. Fourier filtering and standard background subtraction were performed before retrieving the intensity and phase with the standard XFROG algorithm.

3. RESULTS

The generated SC had 15.5 nJ of energy, and 7.3 nJ was delivered to the nonlinear medium. The measured and retrieved XFROG traces (2048 × 2048 arrays), with a FROG error (rms difference between the measured and retrieved XFROG traces) of 0.85% (indicating good agreement), are shown in Figs. 5(a) and 5(b). The retrieved temporal and spectral intensity and phase are shown in Figs. 5(c) and 5(d). The majority of the measured features are reproduced in the retrieved trace, while the noisy background is appropriately ignored by the XFROG retrieval algorithm. The retrieved spectrum (green solid line) ranged from 715 to 850 nm, showing excellent agreement with an independently measured spectrum (black solid line) from the same SC as was measured by our apparatus. The retrieved spectral peak locations also match well with the measured ones. The duration of the pulse is ~2 ps, and the TBP is ~65. This is, to the best of our knowledge, the first single-shot intensity and phase measurement of SC generated from PCF.

It is important to confirm that our retrieved pulse is correct, but there is no alternative technique available to confirm it. The best that can be done is to compare the spectrum measured by our device with that measured using a standard spectrometer. However, SC generation is an inherently unstable process and suffers from severe shot-to-shot fluctuations, especially in its spectrum. As a result, the only spectrum that can be used to confirm the measurement has to come from the same SC pulse that was measured by the XFROG. Since the SC pulse is extremely weak, sending a sufficient amount of the SC pulse to a spectrometer before the nonlinear medium would greatly reduce the signal strength. Fortunately, in the PG geometry, the signal pulse is generated when the gate pulse

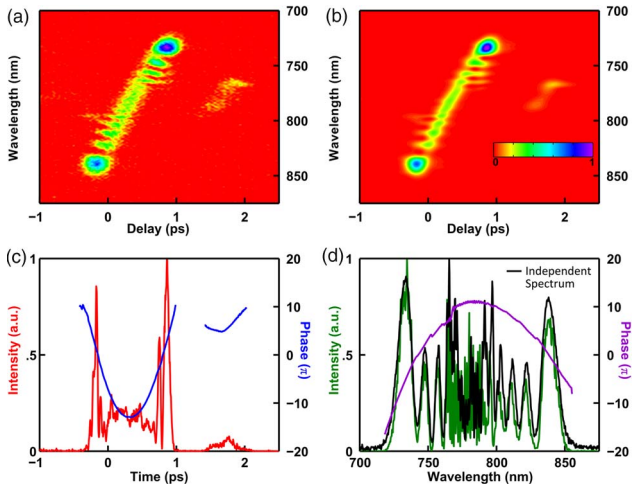

Fig. 5. Single-shot PG XFROG measurement of SC generated from a 23.1 mm long NL-2.8-850 photonic crystal fiber. (a) Measured XFROG trace (2048 × 2048 array) after background subtraction, (b) retrieved XFROG trace with rms error of 0.85%, (c) temporal intensity (red) and phase (blue) of the retrieved SC, and (d) spectral intensity (green) and phase (violet) of the retrieved SC with the same-shot spectrum (black).

slightly rotates the polarization of the SC pulse and a polarization analyzer rejects the original, unrotated polarization. Thus, the spectrum of the analyzer-rejected portion of the SC can be independently measured and hence used to confirm the XFROG-measured spectrum on the same shot. So we directed this rejected pulse to pass through the same grating-lens spectrometer as that used for the PG XFROG setup.

When comparing the retrieved spectrum with the same-shot spectrum measured in this manner, we see that the spectral peaks match well at the edges of the spectrum, but there are some small discrepancies in the central region. During the experiment, we found that a small prepulse was ejected from our regenerative amplifier tens of picoseconds before the main pulse. Due to its much lower energy, the prepulse experienced only slight spectral broadening in the PCF and contributed to the spectrum from 760 to 800 nm, with a FWHM of 15 nm. As FROG is a time-gating device, and the prepulse precedes the gating reference pulse by many picoseconds, the prepulse does not affect the recorded FROG trace. A spectrometer, however, integrates over all the energy that impinges onto the sensor during its exposure time. Thus, the same-shot spectrum is affected by a prepulse, while the FROG measurement is not. A correction to the spectrum was performed by first capturing a FROG trace of the prepulse at the correct delay, determining its spectrum, and then subtracting this spectrum from the same-shot spectrum. This assumes incoherent addition of the prepulse spectrum and the SC spectrum, which is not precisely the case, but it is not possible to do better. We believe that this accounts for the discrepancies in the central region of the spectrum.

With our device demonstrated to accurately measure pulses, we measured a very different SC pulse generated using a seed with less applied chirp and slightly larger energy, sent into a longer piece of fiber 32.2 mm long. The resulting SC had longer temporal duration, broader spectral bandwidth, and less pulse energy. The measured and retrieved XFROG traces (2048 × 2048 array), with a FROG error of 0.57%, are shown in Figs. 6(a) and 6(b). The retrieved temporal and spectral intensity and phase are shown in Figs. 6(c) and 6(d). The retrieved pulse has a TBP of ~96 with a duration of ~2.5 ps and spectrum ranging from 590 to 800 nm. The broader spectrum is not surprising, as the seed is less chirped and hence has a higher peak intensity, which usually generates a SC with a larger bandwidth. The temporal and spectral phases from Figs. 6(c) and 6(d) show more quadratic phase in the output, which is expected because the spectral bandwidth is larger and the fiber is longer. The same-shot spectrum was not measured, as the previous measurement demonstrated the validity of this measurement technique.

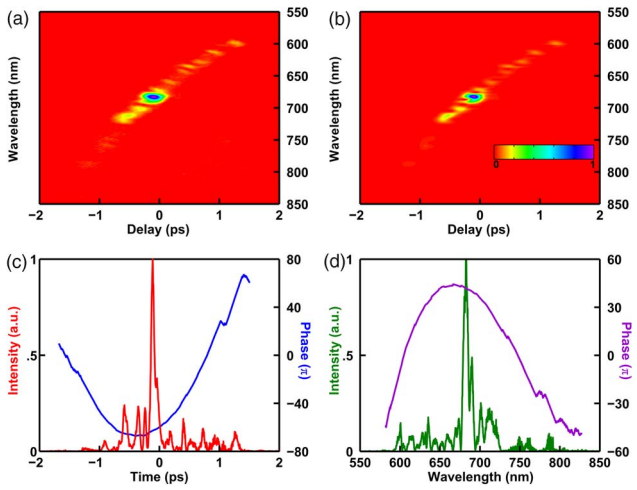

Fig. 6. Single-shot PG XFROG measurement of SC generated from a 32.2 mm long NL-2.8-850 photonic crystal fiber. (a) Measured XFROG trace (2048 × 2048 array) after background subtraction, (b) retrieved XFROG trace with a G-error of 0.57%, (c) temporal intensity (red) and phase (blue) of the retrieved SC, and (d) spectral intensity (green) and phase (violet) of the retrieved SC.

4. CONCLUSIONS

To summarize, we have proposed and demonstrated the use of PFT in the reference arm of PG XFROG to measure the intensity and phase of SC generated from PCF on a single shot. The unlimited phase-matching bandwidth of the PG geometry achieves the required large bandwidth. Further, introducing PFT into the reference pulse increases the temporal range of the single-shot device. More importantly, controlling the internal crossing angle between the tilted reference pulse and the SC inside the nonlinear medium eliminates the longitudinal geometrical smearing completely and allows the use of a thick nonlinear medium to achieve nanojoule sensitivity in our device. As regenerative amplifiers routinely achieve kilohertz repetition rates, and camera frame rates and data storage are more likely to limit the data collection rate, the apparatus described here is more than sufficient for studies of optical rogue waves involving many millions of pulses. Our method is easily able to adapt to different bandwidth and temporal range requirements imposed by optical rogue waves. For example, the optical rogue waves identified by Solli *et al.* require a temporal range of ~6 ps and a spectral bandwidth of ~300 nm centered at 1064 nm [25]. Our current apparatus is capable of such a measurement once the mirrors, lenses, and gratings are replaced with those appropriate for the shifted center wavelength.

FUNDING INFORMATION

National Science Foundation (NSF) (ECCS-1028825).

REFERENCES

1. R. R. Alfano and S. L. Shapiro, "Emission in the region 4000 to 7000 Å via four-photon coupling in glass," Phys. Rev. Lett. **24**, 584–587 (1970).
2. J. K. Ranka, R. S. Windeler, and A. J. Stentz, "Visible continuum generation in air-silica microstructure optical fibers with anomalous dispersion at 800 nm," Opt. Lett. **25**, 25–27 (2000).
3. D. Wildanger, E. Rittweger, L. Kastrup, and S. W. Hell, "STED microscopy with a supercontinuum laser source," Opt. Express **16**, 9614–9621 (2008).
4. G. Humbert, W. Wadsworth, S. Leon-Saval, J. Knight, T. Birks, P. St. J. Russell, M. Lederer, D. Kopf, K. Wiesauer, E. Breuer, and D. Stifter, "Supercontinuum generation system for optical coherence

tomography based on tapered photonic crystal fibre," Opt. Express **14**, 1596–1603 (2006).
5. T. Udem, R. Holzwarth, and T. W. Hansch, "Optical frequency metrology," Nature **416**, 233–237 (2002).
6. D. J. Jones, S. A. Diddams, J. K. Ranka, A. Stentz, R. S. Windeler, J. L. Hall, and S. T. Cundiff, "Carrier-envelope phase control of femtosecond mode-locked lasers and direct optical frequency synthesis," Science **288**, 635–639 (2000).
7. H. Kubota, K. R. Tamura, and M. Nakazawa, "Analyses of coherence-maintained ultrashort optical pulse trains and supercontinuum generation in the presence of soliton-amplified spontaneous-emission interaction," J. Opt. Soc. Am. B **16**, 2223–2232 (1999).
8. A. L. Gaeta, "Nonlinear propagation and continuum generation in microstructured optical fibers," Opt. Lett. **27**, 924–926 (2002).
9. J. M. Dudley, G. Genty, and S. Coen, "Supercontinuum generation in photonic crystal fiber," Rev. Mod. Phys. **78**, 1135–1184 (2006).
10. B. Wetzel, A. Stefani, L. Larger, P. A. Lacourt, J. M. Merolla, T. Sylvestre, A. Kudlinski, A. Mussot, G. Genty, F. Dias, and J. M. Dudley, "Real-time full bandwidth measurement of spectral noise in supercontinuum generation," Sci. Rep. **2**, 882 (2012).
11. U. Møller, S. T. Sørensen, C. Jakobsen, J. Johansen, P. M. Moselund, C. L. Thomsen, and O. Bang, "Power dependence of supercontinuum noise in uniform and tapered PCFs," Opt. Express **20**, 2851–2857 (2012).
12. S. T. Sørensen, C. Larsen, U. Møller, P. M. Moselund, C. L. Thomsen, and O. Bang, "Influence of pump power and modulation instability gain spectrum on seeded supercontinuum and rogue wave generation," J. Opt. Soc. Am. B **29**, 2875–2885 (2012).
13. S. T. Sørensen, C. Larsen, U. Møller, P. M. Moselund, C. L. Thomsen, and O. Bang, "The role of phase coherence in seeded supercontinuum generation," Opt. Express **20**, 22886–22894 (2012).
14. T. Godin, B. Wetzel, T. Sylvestre, L. Larger, A. Kudlinski, A. Mussot, A. Ben Salem, M. Zghal, G. Genty, F. Dias, and J. M. Dudley, "Real time noise and wavelength correlations in octave-spanning supercontinuum generation," Opt. Express **21**, 18452–18460 (2013).
15. Q. Cao, X. Gu, E. Zeek, M. Kimmel, R. Trebino, J. Dudley, and R. S. Windeler, "Measurement of the intensity and phase of supercontinuum from an 8-mm-long microstructure fiber," Appl. Phys. B **77**, 239–244 (2003).
16. J. Dudley, X. Gu, L. Xu, M. Kimmel, E. Zeek, P. O'Shea, R. Trebino, S. Coen, and R. Windeler, "Cross-correlation frequency resolved optical gating analysis of broadband continuum generation in photonic crystal fiber: simulations and experiments," Opt. Express **10**, 1215–1221 (2002).
17. X. Gu, M. Kimmel, A. Shreenath, R. Trebino, J. Dudley, S. Coen, and R. Windeler, "Experimental studies of the coherence of microstructure-fiber supercontinuum," Opt. Express **11**, 2697–2703 (2003).
18. X. Gu, L. Xu, M. Kimmel, E. Zeek, P. O'Shea, A. P. Shreenath, R. Trebino, and R. S. Windeler, "Frequency-resolved optical gating and single-shot spectral measurements reveal fine structure in microstructure-fiber continuum," Opt. Lett. **27**, 1174–1176 (2002).
19. D. Lee, P. Gabolde, and R. Trebino, "Toward single-shot measurement of a broadband ultrafast continuum," J. Opt. Soc. Am. B **25**, A34–A40 (2008).
20. J. Liu, Y. Feng, H. Li, P. Lu, H. Pan, J. Wu, and H. Zeng, "Supercontinuum pulse measurement by molecular alignment based cross-correlation frequency resolved optical gating," Opt. Express **19**, 40–46 (2011).
21. B. Tsermaa, B.-K. Yang, M.-W. Kim, and J.-S. Kim, "Characterization of supercontinuum and ultraviolet pulses by using XFROG," J. Opt. Soc. Korea **13**, 158–165 (2009).
22. M. Rhodes, G. Steinmeyer, J. Ratner, and R. Trebino, "Pulse-shape instabilities and their measurement," Laser Photon. Rev. **7**, 557–565 (2013).
23. J. Ratner, G. Steinmeyer, T. C. Wong, R. Bartels, and R. Trebino, "Coherent artifact in modern pulse measurements," Opt. Lett. **37**, 2874–2876 (2012).
24. M. Hopkin, "Sea snapshots will map frequency of freak waves," Nature **430**, 492 (2004).
25. D. R. Solli, C. Ropers, P. Koonath, and B. Jalali, "Optical rogue waves," Nature **450**, 1054–1057 (2007).
26. J. M. Dudley, G. Genty, and B. J. Eggleton, "Harnessing and control of optical rogue waves in supercontinuum generation," Opt. Express **16**, 3644–3651 (2008).
27. N. Akhmediev, A. Ankiewicz, J. M. Soto-Crespo, and J. M. Dudley, "Rogue wave early warning through spectral measurements?" Phys. Lett. A **375**, 541–544 (2011).
28. D. R. Solli, C. Ropers, and B. Jalali, "Active control of rogue waves for stimulated supercontinuum generation," Phys. Rev. Lett. **101**, 233902 (2008).
29. L. Xu, E. Zeek, and R. Trebino, "Simulations of frequency-resolved optical gating for measuring very complex pulses," J. Opt. Soc. Am. B **25**, A70–A80 (2008).
30. R. Wyatt and E. E. Marinero, "Versatile single-shot background-free pulse duration measurement technique, for pulses of subnanosecond to picosecond duration," Appl. Phys. **25**, 297–301 (1981).
31. T. C. Wong and R. Trebino, "Single-frame measurement of complex laser pulses tens of picoseconds long using pulse-front tilt in cross-correlation frequency-resolved optical gating," J. Opt. Soc. Am. B **30**, 2781–2786 (2013).
32. R. Trebino, *Frequency-Resolved Optical Gating: the Measurement of Ultrashort Laser Pulses* (Kluwer Academic, 2002).

optica

Channeling the electrical breakdown of air by optically heated plasma filaments

MAIK SCHELLER,[1] NORMAN BORN,[2] WEIBO CHENG,[1] AND PAVEL POLYNKIN[1,*]

[1]College of Optical Sciences, The University of Arizona, 1630 East University Blvd., Tucson, Arizona 85721, USA

[2]Faculty of Physics and Material Sciences, Phillipps-Universität Marburg, Renthof 5, Marburg 35032, Germany

*Corresponding author: ppolynkin@optics.arizona.edu

Received 14 April 2014; revised 6 June 2014; accepted 10 June 2014 (Doc. ID 210121); published 18 August 2014

Femtosecond laser pulses with sufficiently high peak power leave tracks of dilute plasma in their wakes. Potential use of this plasma for channeling electrical discharges in the atmosphere has been discussed and demonstrated in laboratory-scale experiments. However, the electron density in femtosecond laser-generated plasma decays rapidly on the nanosecond time scale, due to recombination and electron attachment to air molecules. The finite plasma lifetime limits the maximum extent of the guided electrical breakdown to a few meters. Here, we experimentally demonstrate that the limitation associated with the short plasma lifetime can be overcome though optical heating of the plasma filaments by an auxiliary energetic laser pulse with a duration in the nanosecond range. We show that the breakdown electric field can be reduced by up to a factor of 4 with a heater fluence of about 1 kJ/cm^2. This approach could have applications in channeling long-range electrical discharges in the atmosphere and, potentially, in channeling lightning strikes.

OCIS codes: (020.2649) Strong field laser physics; (140.3440) Laser-induced breakdown; (260.3230) Ionization.

http://dx.doi.org/10.1364/OPTICA.1.000125

Using powerful laser beams for the guidance of the electrical breakdown of air and for channeling natural lightning has been discussed for many years. During the 1970s, the use of energetic Q-switched lasers with a nanosecond pulse duration has been investigated in this context [1]. Those investigations continued into the 1990s [2,3] but have not resulted in the development of a viable guiding technology. Nanosecond lasers can easily produce free electrons in air through optically driven avalanche ionization, but only under the condition of relatively tight focusing of the laser beam. Plasma channels created in air that way are dense but not very long; a large fraction of the laser energy is lost to scattering on the plasma.

The development of femtosecond laser systems and the demonstration of self-channeling of intense femtosecond laser pulses in 1996 [4] gave new hope to the idea of guiding long-range electrical discharges in air by laser beams. In the case of an intense femtosecond laser pulse, the combined effect of self-focusing, diffraction, and photoionization of air results in the propagation regime termed "laser filamentation" [5,6]. Plasma channels produced in air that way are dilute, and thus no excessive loss of laser energy to scattering on the plasma takes place. The guidance of electrical discharges with a length of up to 3.8 m by femtosecond laser filaments has been experimentally demonstrated [7].

The above-mentioned length of the guided breakdown is, however, very close to the maximum that can be attained. The key limitation of the approach is associated with the very short lifetime of plasma in femtosecond laser filaments, which is in the nanosecond range or even shorter [8,9]. Free electrons that are produced through photoionization of air molecules by the intense laser field disappear very rapidly due to recombination and attachment to neutral oxygen molecules. The plasma channel appears to be long, but in fact its instantaneous extent is not more than few meters.

It has been established that dilute filament plasma is not sufficiently conductive to channel an electrical discharge directly. Instead, the guidance involves three essential steps [7,10]: first, a column of free electrons is generated through photoionization of air by the laser field. Second, this weakly conductive path is ohmically heated by the applied DC electric field, resulting in the temperature elevation of the gas on the beam axis by about 100 K above ambient temperature [10]. Third, the heated air column radially expands, creating a reduced-density cylindrical channel between the electrodes. Only then does electrical discharge develop. It goes through the laser-defined low-density path, since, according to the

Paschen's law [11], the strength of the threshold electric field for DC breakdown is approximately proportional to the gas density. This guidance mechanism relies on the existence of a continuous conductive path bridging the entire gap between the electrodes. If the conductive plasma channel is discontinuous or not long enough to connect the electrodes, no ohmic heating of the weakly ionized air takes place and thus no guidance of electrical discharge happens. Thus, a nanosecond-scale plasma lifetime in femtosecond laser filaments fundamentally limits the maximum length of guided electrical breakdown to a few meters.

In this Letter, we report an experimental demonstration of an approach to overcome the above range limitation. Instead of relying on ohmic heating of the conductive plasma channel by the applied DC electric field, we directly heat the plasma by an auxiliary laser pulse with multijoule pulse energy and with a duration in the nanosecond range [12–14]. Following the terminology used in the laser particle acceleration community, we refer to the approach based on the joint application of femtosecond and nanosecond laser pulses as the igniter–heater excitation scheme [15]. Free electrons in the femtosecond laser filament absorb energy from the nanosecond heater pulse through an inverse bremsstrahlung process. Then, just like in the scenario of guidance by the femtosecond filament alone, the heat is transferred from the electrons to the gas molecules, and the gas radially expands, creating a preferred low-density path for electrical discharge to go through. The existence of a continuous conductive path bridging the entire gap between the electrodes is no longer necessary. The lifetime of the low-density guide thus produced is determined by thermal diffusion and is in the millisecond range [16], which is much longer that the lifetime of plasma in the channel.

We point out that our approach does not rely on the maintenance of conductivity in the plasma channel through detachment of electrons from the negatively charged O_2^- complexes by the heater pulse, which is the basis of the approach suggested earlier [17]. In that case, the maximum extent of the guided electrical breakdown is limited by the duration of the heater pulse. The technique proposed here is free from such a limitation. In our case, the nanosecond laser pulse simply acts as a source of heat.

For experimental demonstration of our approach, on a laboratory scale, we make use of a setup schematically shown in Fig. 1. The demonstration utilizes all-solid-state, commercially

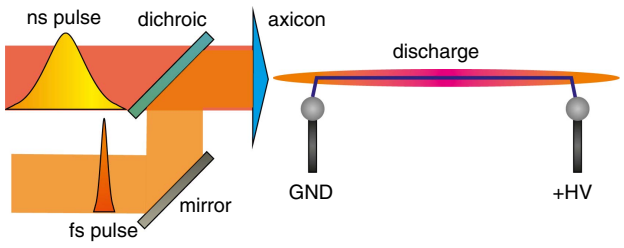

Fig. 1. Schematic of the experimental setup. Femtosecond and nanosecond laser beams are temporally and spatially overlapped and focused by a conical lens. Two ball electrodes are placed close to the beam axis. The electrical breakdown voltage is measured for different interelectrode separations and under various illumination conditions.

available laser sources. The DC voltage source available to us has a maximum output of 35 kV. This source is connected to two ball-shaped metal electrodes. A dilute femtosecond plasma filament is produced by a 100 fs long laser pulse at an 800 nm wavelength, with pulse energy of 15 mJ. The filament plasma is heated by a copropagating pulse from a different laser operating at a wavelength of 1.064 μm and generating pulses of 6 ns duration, with up to 3.3 J of energy per pulse. Both lasers produce 10 pulses/s, and the pulse trains from the two lasers are synchronized in time through a common electronic triggering. The delay between the femtosecond and nanosecond pulses is adjusted to maximize the effect of heating of the filament plasma. The heater pulse slightly lags behind the igniter in time. The time delay has to be shorter compared to the characteristic decay of plasma density in the igniter filament. The optimum igniter–heater delay is in the nanosecond range. The two laser beams have input diameters of about 2 cm. The beams are spatially overlapped using a dichroic mirror and focused by a common conical lens (axicon) with an apex angle of 175°. Thus the created linear focus zone for the beams has a length of about 30 cm. The linear focus is positioned about 5 mm above the ball electrodes, so that the electrodes are not directly exposed to the intense laser field. The estimated peak intensity of the igniter pulse in the interaction zone, assuming linear focusing by the axicon, is 75 TW/cm^2, which is close to the typical value of clamped intensity inside femtosecond laser filaments in air [18].

In Fig. 2, we show experimental results for the threshold breakdown voltage versus distance between the electrodes, for the case of unguided electrical breakdown. The slope of the data curve, at a particular interelectrode separation, approximately equals the threshold breakdown electric field for that separation. For millimeter-scale separations between the electrodes, the breakdown is dominated by the Townsend mechanism, in which no significant local charge separation occurs anywhere between the electrodes. Avalanche ionization is seeded by a secondary emission from the cathode and is driven by the externally applied electric field with a breakdown threshold strength of about 30 kV/cm. As the electrode separation is increased into the several-centimeter range, the

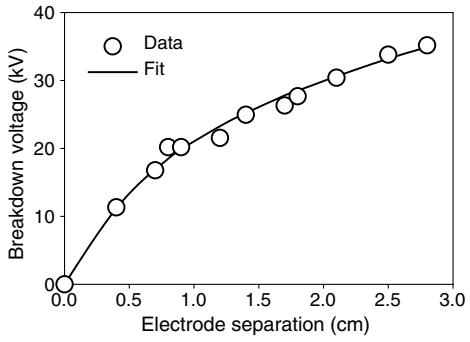

Fig. 2. Threshold breakdown voltage versus interelectrode separation for the case of unguided breakdown. The threshold breakdown field (which is the slope of this curve) decreases as the distance between the electrodes is increased, as a result of the transition from the Townsend to the streamer breakdown mechanism. Data points are shown with circles; the line is a polynomial fit.

streamer mechanism of breakdown starts to dominate, and the average breakdown field reduces to several kilovolts per centimeter. The formation of streamers relies on the local enhancement of the electric field due to charge separation in the streamer head [11]. For the case of very long breakdown sparks, including natural lightning, the average breakdown threshold field can be as low as several hundred volts per centimeter. In that case, the discharge is preceded by the formation of a breakdown leader that involves the development and merging of multiple streamers.

In Fig. 3, we show experimental data for the threshold breakdown voltage, as a function of interelectrode separation, for the cases of breakdown guided by the femtosecond laser filament alone and guidance by the filament heated by a nanosecond heater pulse, with two different heater-pulse energies. The apparent vertical offset of these curves by about 10 kV is because the 5 mm wide gaps between the electrodes and the plasma channel have to be jumped by unguided short streamers, without any help from channeling either by the laser plasma or by the reduced-density air channel. The intensity of the Bessel heater beam along its 30 cm long linear focus zone is higher in the center of the zone and declines toward its ends. Therefore, plasma heating is more intense in the middle of the channel. For the case of intermediate heater fluence of 1.0 kJ/cm^2, that results in the apparent increase of the slope of the breakdown voltage for interelectrode separations above 15 cm.

In the top part of Fig. 4, we show results for the breakdown threshold electric field versus peak fluence of the nanosecond heater pulse in the interaction zone. The energy of the femtosecond igniter pulse is fixed at 15 mJ. It is evident that the breakdown threshold field drops continuously as the fluence of the heater pulse is increased. In the bottom part of Fig. 4, we show the plasma density in the middle of the channel, on an arbitrary unit scale, versus fluence of the heater pulse. The plasma density is measured using a capacitive plasma probe described in detail elsewhere [19]. The curve shows the onset of an optically driven avalanche ionization of air at a heater fluence of about 1 kJ/cm^2. Below that level of fluence, only

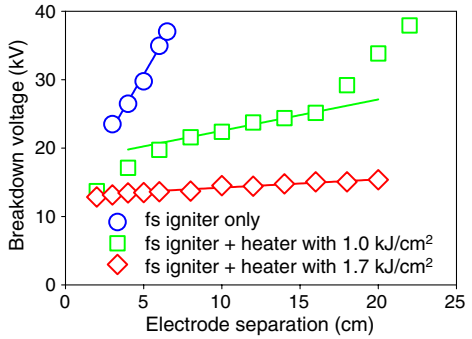

Fig. 3. Threshold breakdown voltage versus interelectrode separation, for the cases of electrical breakdown channeled by the femtosecond laser filament alone and by the filament heated by an auxiliary nanosecond laser pulse, with two different values of peak laser fluence. Optical heating of the filament plasma causes significant reduction of the breakdown threshold electric field.

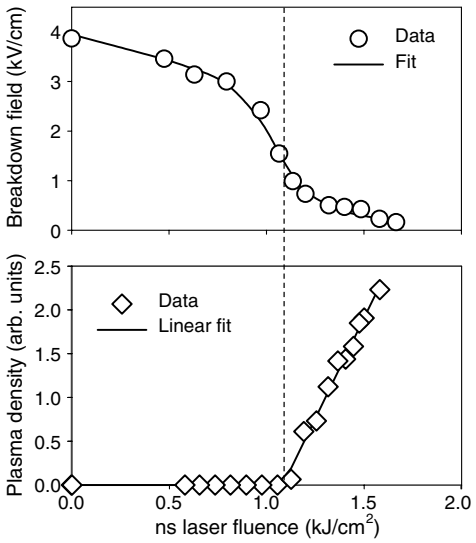

Fig. 4. Top: breakdown threshold electric field versus peak fluence of the nanosecond heater pulse in the interaction zone. The energy of the femtosecond igniter pulse is fixed at 15 mJ. The line is a polynomial fit to the data points. Bottom: corresponding plasma density in the channel on an arbitrary unit scale. The onset of optically driven avalanche ionization at the peak heater fluence of about 1 kJ/cm^2 is evident. Even below the threshold for an optical avalanche (the area to the left of the vertical dashed line), heating of the plasma channel by the nanosecond laser pulse results in significant reduction of the breakdown threshold electric field relative to the unguided case.

dilute plasma produced by the femtosecond igniter pulse is present. Its density is too low to show on the same scale with the density of dense plasma produced by an optically driven avalanche. Above the threshold for an optical avalanche, the heated channel continues to effectively channel electrical breakdown. However, the densified plasma in that case is fragmented into discrete bubbles [13,14]. Although channel fragmentation appears to be not much of a problem in our laboratory demonstration, in which both igniter and heater beams are focused by a common axicon lens, it may be undesirable in long-range applications of our approach. Producing an extended linear focus with a length above ~10 m is very difficult, as that imposes very stringent requirements on the phase flatness of the laser beam front. Thus, in long-range implementations, the use of collimated igniter and heater beams will be more appropriate. The fragmentation of the plasma channel into discrete bubbles will cause excessive scattering losses for the heater beam. Therefore, the practically useful range of heater fluence will be that below the threshold for an optically driven avalanche, which is the region to the left of the vertical dashed line in Fig. 4. Remarkably, even below the threshold for optical avalanche ionization, the breakdown electric field can be reduced by up to a factor of 4 relative to the case of guidance by the femtosecond filament alone, with no range limitation related to the short plasma lifetime.

In order to estimate how the proposed channeling approach scales to realistic long-range situations, consider the case with

an interelectrode separation of 20 m. Such a range could be practically relevant, e.g., for the remote detonation of land mines. In our laboratory-scale demonstration, a noticeable reduction of the breakdown threshold electric field relative to that for an unguided breakdown was achieved with a nanosecond pulse with a fluence in the range of 1 kJ/cm^2. A collimated Gaussian beam with a wavelength of 1 μm and Rayleigh length of 20 m will have a diameter of 5 mm. At the above-mentioned level of fluence, that beam size will correspond to a total heater pulse energy of about 200 J. Such laser energies are certainly achievable with modern solid-state laser technology.

We point out that if the 200 J heater pulse discussed above had a pulse duration of 6 ns, as in our laboratory-scale demonstration, the peak pulse power would be above the critical power for self-focusing in air, potentially causing problems associated with self-focusing of the heater beam. Thus a longer heater pulse with a duration in tens of nanoseconds would be preferred, as the optical heating effect scales not with the peak laser intensity but with the fluence [13]. For heater pulses that are longer than the lifetime of free electrons in the femtosecond igniter filament, a heater beam of sufficient intensity will cause detachment of electrons from O_2^- complexes and will continue to deposit heat into the gas [20]. Thus the maximum pulse duration of the heater pulse will not be limited by the lifetime of the igniter plasma. Alternative heater sources including powerful microwave beams may be also considered.

To summarize, we have demonstrated that the application of optical heating of dilute plasma in femtosecond laser filaments in air creates an extended low-density guide capable of channeling the electrical breakdown of air and thus leads to a significant reduction in the electrical breakdown threshold. This approach to laser guidance of electrical discharges in air alleviates the limitation on the maximum range of guidance associated with the nanosecond-scale lifetime of free electrons in femtosecond laser filaments.

FUNDING INFORMATION

Air Force Office of Scientific Research (AFOSR) (FA9550-10-1-0561, FA9550-12-1-0143, FA9550-12-1-0482); Defense Threat Reduction Agency (DTRA) (HDTRA 1-14-1-0009).

REFERENCES

1. D. W. Koopman and T. D. Wilkerson, J. Appl. Phys. **42**, 1883 (1971).
2. D. Wang, T. Ushio, Z.-I. Kawasaki, K. Matsuura, Y. Shimada, S. Uchida, C. Yamanaka, Y. Izawa, Y. Sonoi, and N. Simokura, J. Atmos. Terr. Phys. **57**, 459 (1995).
3. M. Miki, T. Shindo, and Y. Aihara, J. Phys. D **29**, 1984 (1996).
4. A. Braun, G. Korn, X. Liu, D. Du, J. Squier, and G. Mourou, Opt. Lett. **20**, 73 (1995).
5. A. Couairon and A. Mysyrowicz, Phys. Rep. **441**, 47 (2007).
6. L. Berge, S. Skupin, R. Nuter, J. Kasparian, and J.-P. Wolf, Rep. Prog. Phys. **70**, 1633 (2007).
7. M. Rodríguez, R. Sauerbrey, H. Wille, L. Woste, T. Fujii, Y.-B. Andre, A. Mysyrowicz, L. Klingbeil, K. Rethmeier, W. Kalkner, J. Kasparian, E. Salmon, J. Yu, and J.-P. Wolf, Opt. Lett. **27**, 772 (2002).
8. S. Tzortzakis, B. Prade, M. Franco, and A. Mysyrowicz, Opt. Commun. **181**, 123 (2000).
9. Z. Sun, J. Chen, and W. Rudolph, Phys. Rev. E **83**, 046408 (2011).
10. S. Tzortzakis, B. Prade, M. Franco, A. Mysyrowicz, S. Hüller, and P. Mora, Phys. Rev. E **64** 057401 (2001).
11. Y. P. Raizer, *Gas Discharge Physics* (Springer, 1997).
12. M. N. Schneider, A. N. Zheltikov, and R. B. Miles, Phys. Plasmas **18**, 063509 (2011).
13. P. Polynkin and J. V. Moloney, Appl. Phys. Lett. **99**, 151103 (2011).
14. P. Polynkin, B. Pasenhow, N. Driscoll, M. Scheller, E. M. Wright, and J. V. Moloney, Phys. Rev. A **86**, 043410 (2012).
15. P. Volfbeyn, E. Esarey, and W. P. Leemans, Phys. Plasmas **6**, 2269 (1999).
16. Y.-H. Cheng, J. K. Wahlstrand, N. Jhajj, and H. M. Milchberg, Opt. Express **21**, 4740 (2013).
17. P. Rambo, J. Biegert, V. Kubecek, J. Schwarz, A. Bernstein, J.-C. Diels, R. Bernstein, and K. Stahlkopf, J. Opt. Technol. **66**, 194 (1999).
18. S. Xu, J. Bernhardt, M. Sharifi, W. Liu, and S. L. Chin, Laser Phys. **22**, 195 (2012).
19. P. Polynkin, Appl. Phys. Lett. **101**, 164102 (2012).
20. B. Zhou, S. Akturk, B. Prade, Y.-B. Andre, A. Houard, Y. Liu, M. Franco, C. D'Amico, E. Salmon, Z.-Q. Hao, N. Lascoux, and A. Mysyrowicz, Opt. Express **17**, 11450 (2009).